FREDRIK DESSEN

DIRECT TRAINING OF ROBOTS USING A POSITIONAL DEVIATION SENSOR

NTH
UNIVERSITETET I TRONDHEIM
NORGES TEKNISKE HØGSKOLE

DOKTOR INGENIØRAVHANDLING 1988:33
INSTITUTT FOR TEKNISK KYBERNETIKK
TRONDHEIM 1988

88-37-W

DIRECT TRAINING OF ROBOTS USING A POSITIONAL DEVIATION SENSOR

by
Fredrik Dessen

Doktor ingeniør dissertation,
Norwegian Institute of Technology,
Division of Engineering Cybernetics,
September 1988

Abstract. A device and system for physically guiding a manipulator through its task is described. The device consists of inductive, contact-free positional deviation sensors, enabling the robot to track a motion marker. Factors limiting the tracking performance are the kinematics of the sensor device and the bandwidth of the servo system. Means for improving it includes the use of optimal motion coordination and force and velocity feedback. This enables real-time manual training of high-performance manipulators. Multi-dimensional, non-linear measurement equations for the sensor system are developed, and their inversion described.

PREFACE

This work presents a new device and method for direct teaching of robots such that the programmer is not hampered by the friction and the dynamics of the manipulator. The idea of using a short-range contact-free positional deviation sensor for this purpose was suggested by Prof. J.G. Balchen in 1984 (ref.). The same year, the author became engaged in outlining a system, and predicting its performance. Results from this work are mainly retained in Sections 4 and 5 below. Since then, a prototype deviation sensor has been designed and built, and the principle has been proven possible by several experiments. The compiling of this text has been going on since September 1987, starting with a brief presentation at the NATO Advanced Research Workshop "Sensor Devices and Systems for Robotics" in October the same year.

Objective. The main purpose of this dissertation is to outline a system for direct teaching, with special emphasis on the tracking controller. Thus, the complementary (learning and repeating) role of the robot is given less attention. The design of the positional deviation sensor is described in detail, however complying to the above objective, no formal discussion is made concerning the accuracy needed to obtain sufficiently exact motion recordings.

Arrangement. The present text falls into three parts which can be denoted

I. Extended introduction, Sections 1 through 5.
II. Advanced control, Sections 6 through 8.
III. Physics of the sensor, Sections 9 and 10.

In order to make the first part a self-contained system description, Sections 3 and 5 are included which, logically, as well belongs to Parts III and II respectively. The complete description of the control problem is thus found in Sections 5 through 8 whereas the positional deviation sensor is described in Sections 3, 9 and 10. These parts can be read separately if so desired.

Acknowledgements. I wish to thank Trallfa Robot A.S. for supporting this project, Dir. Dag Kjosavik and Jan Inge Tjølsen in special for their interest and assistance. I also appreciate the advice and support given to me by my supervisor Prof. J.G. Balchen and the technical assistance given by Stefano Bertelli and Arvid Lervold, as well as the careful typing of this manuscript by Mrs. Eva Amdahl.

Trondheim, july 1988

Fredrik Dessen

CONTENTS

1. ROBOT PROGRAMMING METHODS

In the years following the introduction of the industrial robot, nearly all programming was done by direct training. This is a process where the robot is physically led through its task, and a sequence of points is recorded for playback at a later time. An alternative to direct training is numerical motion specification, which may be quite cumbersome unless combined with some other method. In this section, refinements of these basic methods will be discussed. A new device, which is the topic of this dissertation, will also be introduced. At the end of the section, some notes are made on the programming of paint spraying robots, which will be of major interest throughout this work.

1.1. Motion specification

The methods of direct training are still popular. This is due to the natural feedback given to the programmer when watching the manipulator move through space. The robot manipulator may be led remotely, by means of a teach-pendant. This is often associated with point-to-point control systems (Engelberger, 1980), in which the task is described by indicating to the system a relatively short sequence of positions. This combination was introduced together with the first Unimate systems. The presence of feedback is most clear in the case of manual lead-through, where the operator not only receives close up visual feedback, but also wields direct control. Power to the motor system is usually shut off and the programmer moves the manipulator with his hands. The method may be used for the programming of point-to-point control systems, but is more frequently used in continuous path systems. Here, the motion of the manipulator during programming is recorded automatically at a fixed frequency in order to create an almost continuous reference trajectory. During playback the

manipulator echoes the motion of the programmer, who often is a skilled craftsman rather than a trained programmer. The success of this approach depends on careful design of the manipulator. The arm should be lightweight, preferably gravitational effects should be compensated, and joint friction during training must be low. These considerations need not be taken to implement remote control by teach-pendant. However, even when considering the advantage of visual feedback, this method may be quite cumbersome in practice. After the introduction of real-time coordinate conversion and multi-dimensional joy-stick controls, the process has become somewhat easier. It has also become possible to program forces. Nevertheless, the information lag due to the dynamics of the human system of vision and brain makes a teach pendant inconvenient for trajectory recording in real time (Hirzinger, 1982; 1983).

The alternative to direct training seems to be the use of computer language. This may include program flow control, manipulator move statements and a number of additional commands, such as gripper control. In the most extreme case, the motion coordinates are specified numerically by the programmer. This is an environment in which computer scientists and specialists in numerical control may feel comfortable. On the other hand; a craftsman, who may be an expert on the production process itself, may not be able to describe a task in this way. In addition, the natural feedback which led to the success of direct training disappears. Or at best is available in batches.

Recent robot programming languages are high-level and block-structured in the same way as general computer languages. Some also have real-time capabilities. Usually means for manipulating coordinate systems are provided. In some cases, even contact forces and compliance may be programmed (Blume, 1986; Hayward, 1986). It is said that languages develop from being arm oriented into being object oriented, which means that object motion rather than arm motion is specified in the program. Considering the complexity and the abstract structures of such a language, it should be thought of as a design tool rather than the means for

application oriented programming. In fact, once installed in an industrial robot system, this tool may be used to structure and simplify the development of highly specialized user interfaces. As an example, the development of a system for direct programming may thus be carried out in no time. A well designed language may also be the base for more advanced applications, such as task oriented systems with the capability of problem solving and interfaces to factory management systems and CAD databases (Fu, 1987; Blume, 1986; Alexander, 1986; Parent, 1984).

For an operator who is properly trained, the use of a fairly general programming language will increase the versatility of the industrial robot. However, it is often desirable to indicate positions by means of direct programming. These features are often combined. Then, the motion is usually specified on a point to point basis. In principle, once a set of positions is indicated, it is possible to simply edit motion using the stored positional data. This may be convenient, for instance when editing is done on a standard computer terminal, as in the Robtalk/TSM-system (Trallfa, 1986). In other systems, such as ASEA stage 2 IRb-system, point and flow programming is usually done concurrently. This is convenient because of the handy teach-unit, which includes a menu-based terminal as well as a joy-stick for remote control (ASEA, 1984).

Compared to the use of programming languages and remote control by joy-stick, the main advantage of manual lead-through programming is the close interaction between the robot and the operator. A disadvantage is that physical force must be applied, and that special care must be taken in the design of the manipulator. Several approaches have recently been made to include the possibility of manual control in arbitrary industrial robot systems. Usually, this has been done by mounting a force-sensing handle onto, or near, the manipulator end effector. The force applied is then used to indicate the desired motion of the manipulator. In principle, the method is easy to apply. Its main advantages over remote control by joy-stick are that the operator interacts directly with the manipulator, and that there is no

confusion as to how the manipulator reacts when the handle is operated. In addition to reducing the time needed for training, this may improve personnel safety. This statement may seem paradoxical, but is based on the fact that the operator frequently works within the range of the manipulator even when using a remote control device.

Unfortunately, the close interaction between the operator and the manipulator leads to a stability problem (Hirzinger, 1982) which is due to the stiffness of the force sensor. Because of this, the bandwidth of this assisted manual control system may be low, and it may still be necessary to apply considerable force in order to make the manipulator move. The ideal approach to manual lead-through programming seems to be a system where the operator can hold the tool freely in his own hands, and complete the task without being hampered by the manipulator. This is possible when the tool motion is recorded by means of a remote positional sensing device. One such device is a lightweight, low friction dummy arm equipped with joint displacement sensors. A second possibility is the use of sensors based on optical, magnetic, soundwave or electromagnetic wave measurements (Ishii, 1987; Foley, 1987; Parent, 1984). Using this method, there will be a good deal of freedom with respect to the manipulator design. Positional sensing devices may also be used for remote control. In this case the manipulator may be set up to echo the detected motion. Since visual feedback is available, the sensor does not need to be very accurate. If a force-servoed dummy arm is used, force feedback may be available as well (Vertut, 1985).

This dissertation presents a new system for contact-free positional sensing of a tool or teach-handle moved freely by the operator (Balchen, 1984). It consists of a small-range positional deviation sensor mounted at the tip of the manipulator. If used with a teach-handle, the device resembles the force-sensing handle mentioned earlier, except that there is no contact between the programmer and the manipulator. Because of this, the stability conditions are altered. A second interesting application is to configure the unit to sense the motion of a tool, and make the

manipulator track it. This allows the operator to hold the tool freely in his own hands, and carry out the task the way he is used to. The robot senses the tool motion in close proximity, and records it in order to create a robot program. Compared to the use of long-range positional sensors, tool motion is now restricted by the dynamic capabilities of the manipulator. On the other hand, close-range sensing may be more accurate than sensing at a distance. These issues will be covered in later sections.

1.2. Off-line programming

Today, much research effort seems to be concentrated on robot programming languages. The off-line nature of this approach enables robot reprogramming without interrupting the production process. It also opens the way towards full automation of robot program generation. Training by means of remote positional sensors may also be considered to be off-line, in the sense that the manipulator is not involved during the training session. However, to avoid interrupting production, a copy of the environment must be available for the purpose of programming. This may in turn occupy valuable space. Similar abstract computer models may be used to check the execution of any robot program. In some cases they may even provide on-line feedback to the programmer, who can then perform direct training in a simulated environment (Foley, 1987).

With off-line programming, no feedback from the real manipulator is available. Feedback may exist, but it is taken from a model of the real situation. Success consequently depends upon the exactness of the model, or the existance of means to correct modelling errors. Model correction may in turn require a sensory controlled robot. Future off-line programming systems seem promising, however their complexity and anticipated cost may discourage potential users.

1.3. Paint spraying robots

The task of paint spraying requires robots which are capable of following complex trajectories accurately at high speed. Hence, a robot program for paint spraying will consist of a detailed sequence of recorded positions. Because of this, real-time manual lead-through programming is very popular for this application. The simplicity of the method makes it possible for a skilled paint-sprayer to describe the task by doing it himself.

A well-known manufacturer of paint-spraying robots is the Norwegian company Trallfa Robot AS. It is believed that their success is the result of their main line of products being dedicated to this one application (Engelberger, 1980). Details of the manipulator designs, the programming systems and storage media reflect their dedication to paint-spraying applications. Their first commercial success, the TR-2000, consisted of a lightweight spring-balanced manipulator and a control system with a magnetic tape cartridge unit for program storage and playback. Program selection was done by inserting different cartridges. The sequential nature of the storage medium makes it difficult to include any kind of program flow control. However, this seems to be of little importance in paint spraying, as in many other applications. The sampling rate was fixed at 80 Hz both for program recording and playback, unless the system had to be synchronized to a conveyor or other. With such dedicated continuous path systems, the only means of programming was by manual lead through. This was still the case when point-to-point control was enabled by the introduction of a microprocessor based control unit.

The standard unit today is the TR-4000, which is fully computer controlled. More means for program editing and structuring are available, however the programming system still reflects the nature of industrial paint-spraying. For example, means for branching and looping are restricted, and only available at the program selection level (Trallfa, 1982a; 1982b). At this level, the system design is focused on common situations, such as

batch production, conveyor systems, and the repetition of single programs. The way of managing this structure is very simple. Like its predecessors, the manipulator is lightweight and spring balanced. Low friction during manual lead-through programming is secured by the introduction of a split-piston arrangement for removing oil from the hydraulic actuators.

From here, two trends seem to develop. One is to design cheaper robots which retain the basic concept of the Trallfa Robot systems. This is the case for the TR-400. The other approach is to design complete, Advanced Coating Systems, such as TRACS. In both cases it seems to be difficult to preserve the basic method of real-time manual lead-through programming. In the first case, because such considerations will increase the price of the manipulator. In the second case, complex manipulator designs make it more difficult to retain the prerequisites for this basic method. It is also evident that the demand for continuous path programming is decreasing among large-scale manufacturers, who usually prefer off-line or at least point-to-point programming systems. This turns paint spraying into a science rather than an art. The process becomes more predictable, and subsequent modification of points, speed and the flow of paint becomes simpler.

On the other hand, it seems that many small or medium-scale manufacturers still may benefit from the use of manual lead-through programming. In order to apply the method on arbitrary robot manipulators, assisted lead-through may be used. Such a system may be implemented using a positional deviation sensor. Problems will of course arise, due to the extreme performance requirements in paint spraying. However, when these are solved, a conceptually simple system will be provided for easy programming by means of manual lead-through.

2. OUTLINE OF THE SYSTEM

A motivation for employing the positional deviation sensor, which is the subject of this dissertation, will be given by considering the programming of a paint spraying robot. During the training session, the operator holds the spray-gun in his own hands, and carries out the task in his usual manner. At the same time, the robot manipulator follows the tool slavishly, without any contact. The situation is shown in Fig. 2.1. The manipulator is able to track the tool because of feedback from the positional deviation sensor. This consists of two complementary parts; one fixed to the tool, and the other to the wrist of the manipulator. The sensor measures the displacement between the two parts, Fig. 2.2.

2.1. Homogeneous transformations

The situation may be formalized in terms of homogeneous transformation matrices (Paul, 1981; Fu, 1987). A homogeneous transformation, H, as used to describe the position and orientation of some object, is a 4 by 4 matrix construction with the structure

$$H = \begin{bmatrix} & R & & \underline{p} \\ 0 & 0 & 0 & 1 \end{bmatrix} \qquad (2.1)$$

Here R denotes a 3 by 3 orthonormal directional cosine matrix for the description of orientation, and $\underline{p}$ a 3-dimensional translational displacement vector. The elements of row 4 are usually fixed, their main function being to simplify the writing of transformation equations. In this context, a point in space may be described by a 4-dimensional vector

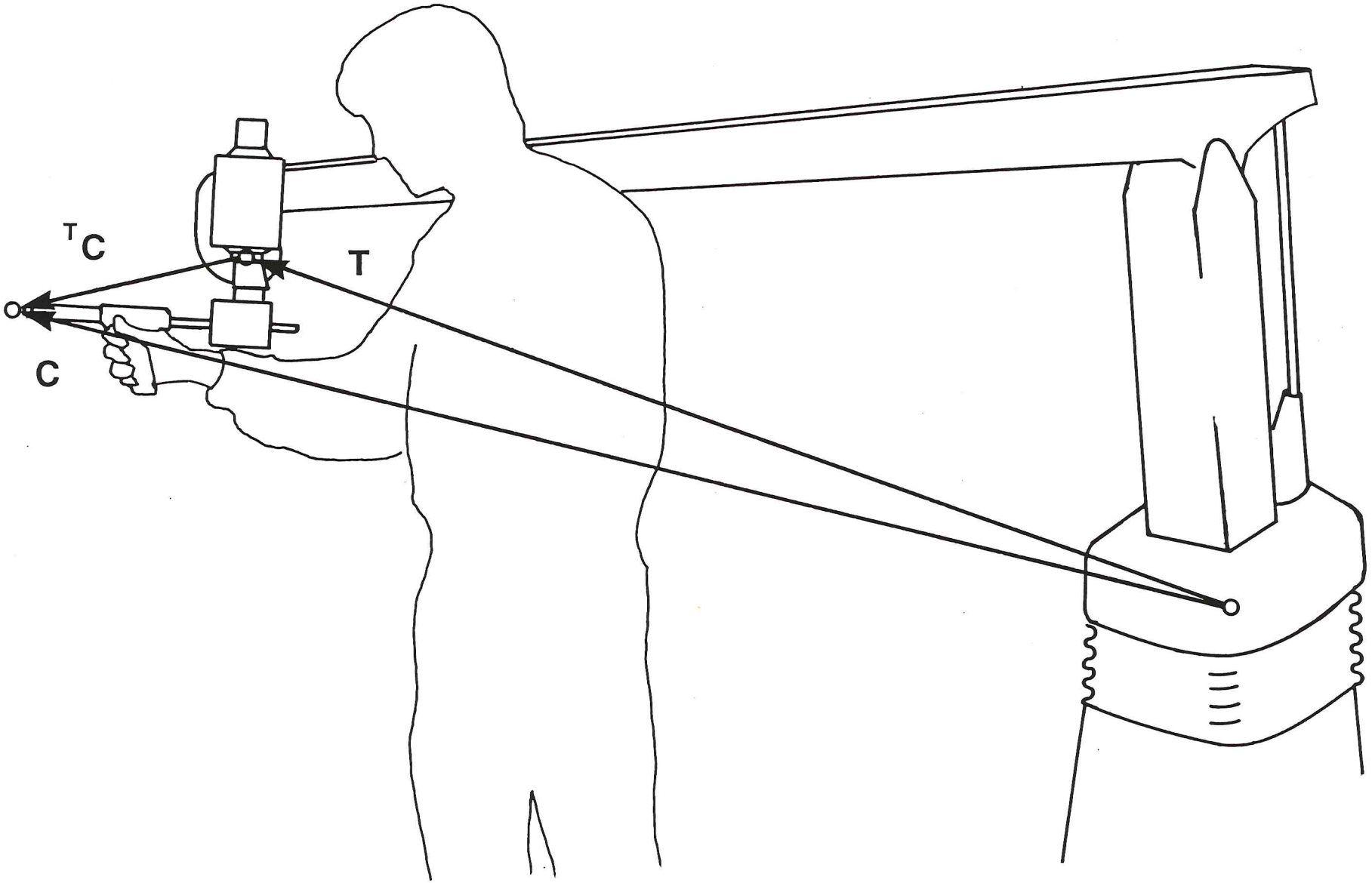

Figure 2.1. Manual lead-through programming.

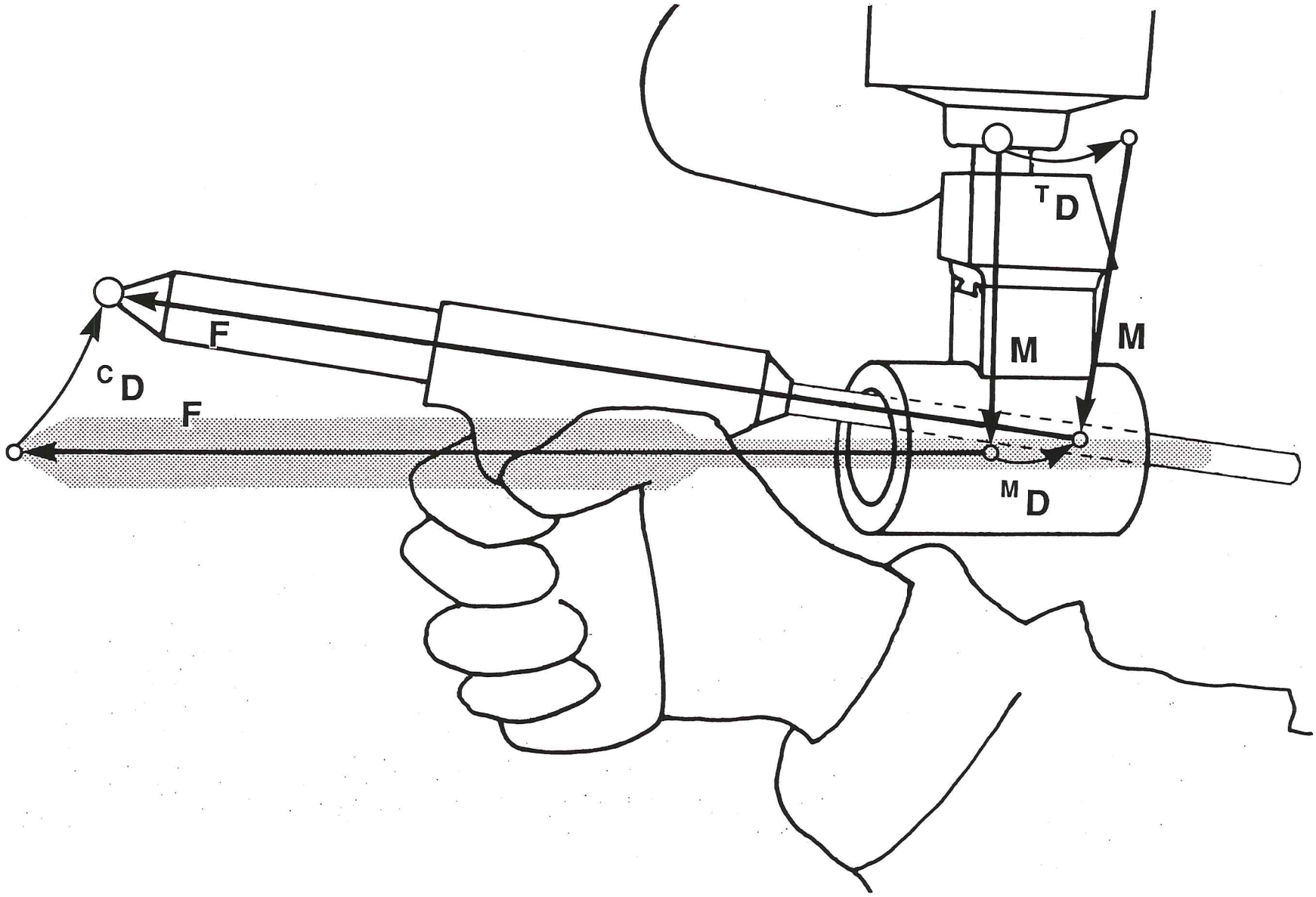

Figure 2.2. Position of the tool relative to the wrist, i.e. ${}^{T}C$ may be obtained by following either of the paths $MF{}^{C}D$, $M{}^{M}DF$ or ${}^{T}DMF$.

$$\underline{h} = [\ \underline{p}^T\ ,\ 1]^T \tag{2.2}$$

where $\underline{p}$ is 3-dimensional, and describes position in the usual sense.

If vector ${}^H\underline{v}$ describes a position in space relative to a coordinate frame described by H, the position may be described in base coordinates by

$$\underline{v} = H\ {}^H\underline{v} \tag{2.3}$$

In the same way, if ${}^H T$ describes a coordinate frame in terms of H-coordinates, it may be described in base coordinates by

$$T = H\ {}^H T \tag{2.4}$$

The inverse of a homogeneous transformation matrix is easily computed by

$$H^{-1} = \begin{bmatrix} & R^T & & -R^T\underline{p} \\ 0 & 0 & 0 & 1 \end{bmatrix} \tag{2.5}$$

where H^{-1} is the inverse of H in (2.1), and post superscript T denotes matrix transposition. This is due to the orthonormality of R.

If matrix D describes a small positional and rotational deviation between two objects, such as the two complementary parts of the positional deviation sensor, it will be close to unity. In this case it may be approximated by a first order expansion about the unity matrix I.

$$D = I + \Delta = \begin{bmatrix} 1 & -\delta_3 & \delta_2 & d_1 \\ \delta_3 & 1 & -\delta_1 & d_2 \\ -\delta_2 & \delta_1 & 1 & d_3 \\ 0 & 0 & 0 & 1 \end{bmatrix} \qquad (2.6)$$

Based on the elements of Δ, a 6-dimensional deviation vector may be constructed.

$$\underline{d} = [d_1 \ , \ d_2 \ , \ d_3 \ , \ \delta_1 \quad \delta_2 \ , \ \delta_3]^T \qquad (2.7)$$

Here the first three elements express the translational and the others the rotational deviation.

In Fig. 2.1 the position of the manipulator wrist relative to its base is described by the positional transformation matrix T. In the same way, the position of the tool is described by C. Using the notation of (2.4), T and C may be related by

$$C = T \ {}^{T}C \qquad (2.8)$$

Here ${}^{T}C$ expresses tool position relative to the wrist. In Fig. 2.2 matrix ${}^{T}C$ is split into two fixed transformations, M and F, and three alternative displacement matrices, ${}^{T}D$, ${}^{M}D$ or ${}^{C}D$. Here M defines the sensor frame, F is a tool description matrix and ${}^{M}D$ expresses the tool displacement as seen from the sensor frame. ${}^{T}D$ and ${}^{C}D$ are related to ${}^{M}D$ by

$${}^{T}D = M \ {}^{M}D \ M^{-1} \quad ; \ {}^{T}\Delta = M \ {}^{M}\Delta \ M^{-1} \qquad (2.9)$$

$${}^{C}D = F^{-1} \ {}^{M}D \ F \quad ; \ {}^{C}\Delta = F^{-1} \ {}^{M}\Delta \ F \qquad (2.10)$$

Here the relationship between Δ-matrices (2.6) is included as well.

Using the displacement matrix ${}^{M}D$, (2.8) may be expressed in more detail as

$$C = T\ M\ {}^{M}D\ F \tag{2.11}$$

Since T may be computed when knowing the position of the manipulator, and ${}^{H}D$ is given by the sensor output, tool position relative to the base may be found at any time using (2.11). The computed tool motion is recorded in order to create a robot program.

2.2. Tool tracking and motion recording

Because of the limited range of the deviation sensor, the manipulator must track the tool closely in order to keep ${}^{M}D$ as close to unity as possible. Hence, an approximate tracking error may be expressed by ${}^{M}\Delta$ (2.6) or ${}^{M}\underline{d}$ (2.7). Appropriate action to make the manipulator follow the tool is computed by a coordinating controller. The tracking control system is outlined in Fig. 2.3, together with the motion recording system. Here ${}^{M}\underline{d}$ is given as input to the controller, $\underline{u}$ is the control action, and $\underline{q}$ expresses the manipulator motion in terms of a set of generalized coordinates. For the purpose of motion recording, matrices ${}^{M}D$ and T are computed. From this, a sequence of tool positions C is obtained by (2.11) and stored in memory. The design of tracking controllers and expressions for computing ${}^{M}D$ and ${}^{M}\underline{d}$ are treated in later sections.

The two uses which are made of the deviation sensor output, have different requirements for accuracy and computational speed. For tool tracking, fresh control error values must be present at a sufficiently high rate. Due to the feedback, there is no need for precise values. This implies that approximations may be made in order to reduce the time needed for computations. In later sections, it appears that the computations of manipulator kinematics, sensor kinematics and the measurement functions may be simplified for this purpose. Motion recording however, requires that ${}^{M}D$ and T are computed as exactly as possible. On the other hand, since there are no inherent real-time requirements, the work may either be done on a separate computer, or later when the

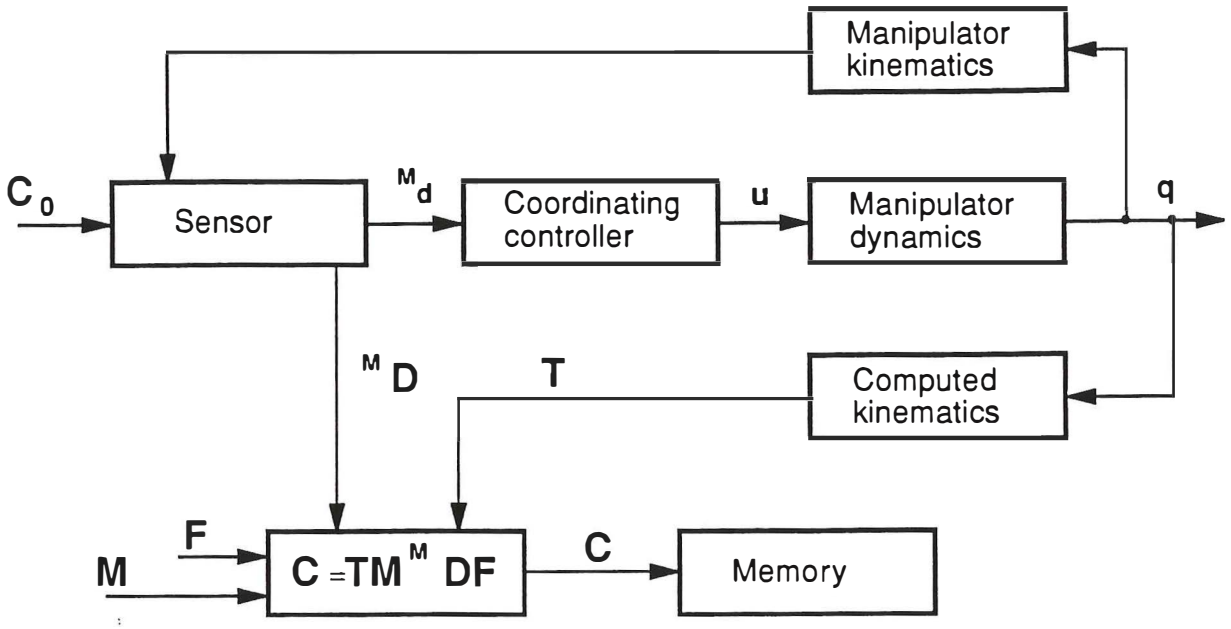

Figure 2.3. Tool tracking and motion recording. The tool motion C_0 is reproduced and stored in memory.

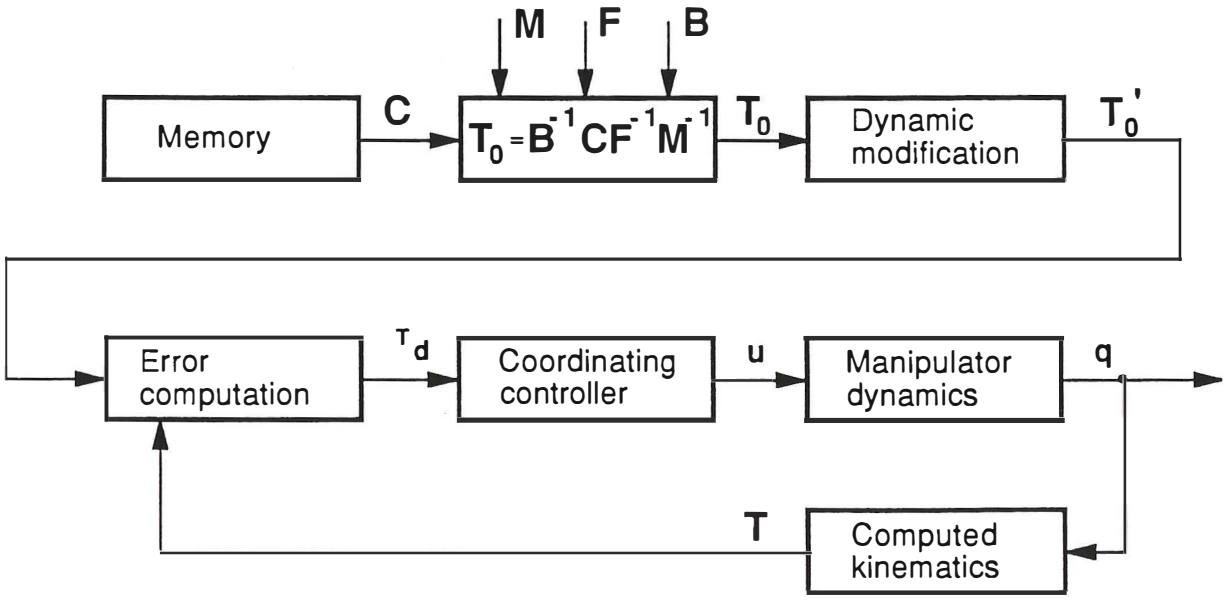

Figure 2.4. Motion playback.

training session is over. The last alternative is not recommended, since it makes the robot system inoperable for some time after training.

2.3. Motion playback

Figure 2.4 shows the structure of a motion playback system. In essence the task of the manipulator is to make a tool repeat the motion described by C, which is stored in memory. However, this motion sequence may be modified in several ways before it is used as a reference trajectory. In the simplest case, the same manipulator and tool are used for both the programming and playback. The deviation sensor may have been replaced by a dummy with the same kinematic description, M.

In general however, M and F may have been altered, and it may be desirable to refer the motion to a new coordinate system B. These modifications enter as shown in the figure. In addition, a dynamic modification block may be inserted in front of the positional controller. This may for instance be a filter which represents the inverse of the manipulator dynamics. As the present work is concerned with the design of the tool tracking system and the positional deviation sensor, the playback system is only considered in passing.

3. KINEMATIC DESCRIPTION OF THE SENSOR

So far, very little has been said about the displacement sensor itself. It has been pointed out that it consists of two parts, and it may have a limited range. In this section, the measurement principle and the design of the sensor are outlined. Based on this, the internal kinematics of the sensor is described.

3.1. Sensor design

The sensor consists of two cylindrical parts made of ferromagnetic material, Fig. 3.1. The two cylinders are magnetized in opposite axial directions by means of a solenoid mounted inside the larger, hollow part. This creates a radial magnetic field between them which varies according to their relative position. By measuring the magnetic field at selected points, relative motion is monitored.

A section of the sensor is shown in Fig. 3.2. Here, 4 pick-up solenoids (M2, M4, M6 and M8) are used to measure translation along the p_2 and p_4-axes (Fig. 3.3). From this, translation along the ^{M}y-axis and rotation about the ^{M}x-axis (Fig. 3.1) may be computed. Similarly, 4 solenoids are used to monitor the p_1 and p_3-motion. Axial translation, p_5, is measured by M9 and M10. It is seen that displacements p_1 through p_5 each are measured by two opposite solenoids. The relative difference may be computed for each pair. The results form a vector of measurements, y_1 through y_5, where y_i largely corresponds to p_i. A detailed mathematical description of these measurements is given in Section 9. Means for measuring p_6-motion are not shown in the figures. Depending on the application, this will either be omitted or consist of a

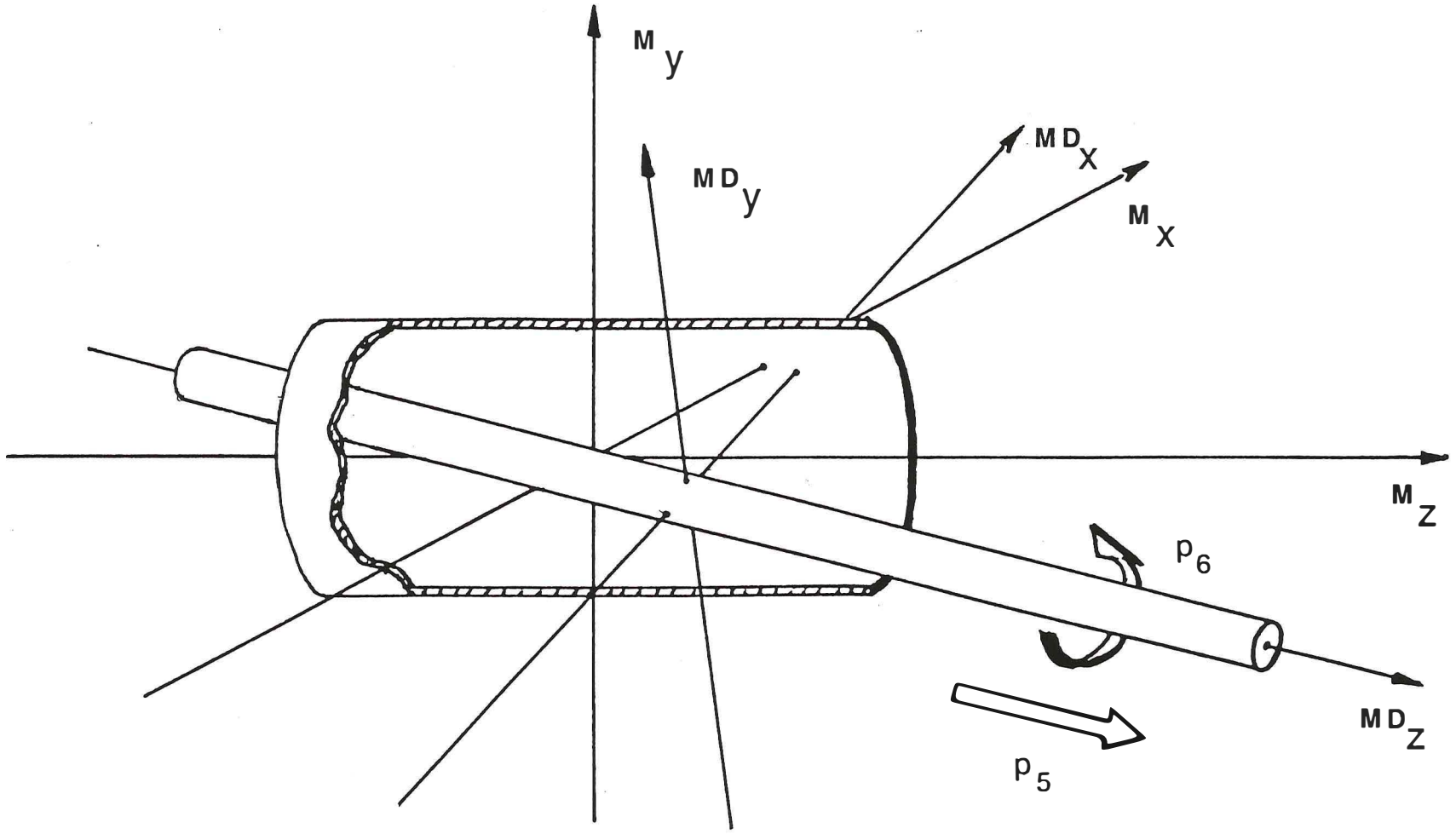

Figure 3.1. Coordinate systems of the two parts of the sensor.

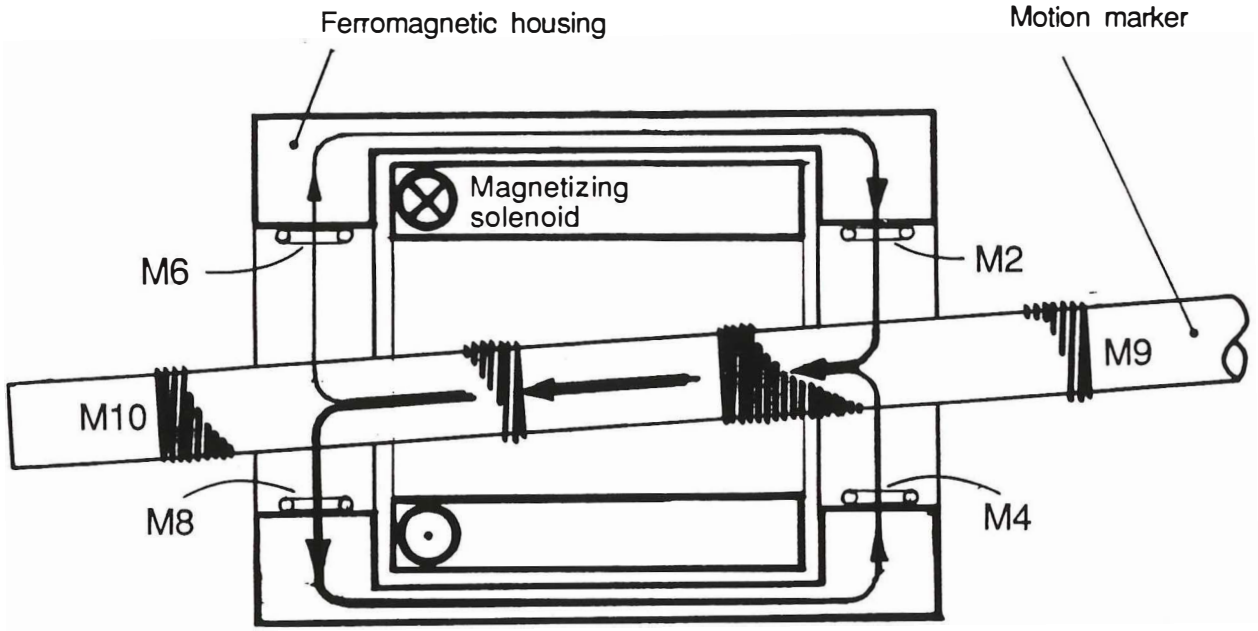

Figure 3.2. Measurements. Flux passing through each solenoid varies according to motion.

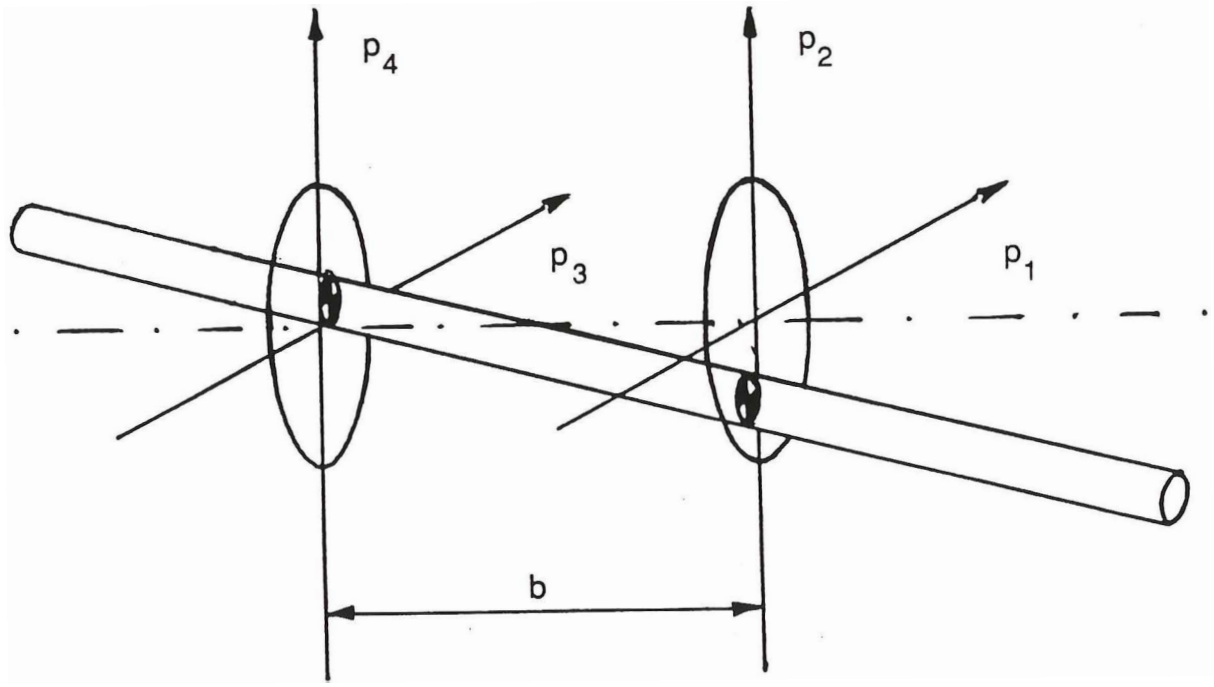

Figure 3.3. Internal radial deviation quantities.

4-solenoid, resolver-like configuration.

Given the 6-dimensional internal deviation vector

$$\underline{p} = [p_1, p_2, p_3, p_4, p_5, p_6]^T \tag{3.1}$$

the displacement transformation ${}^{M}D$, and the deviation vector ${}^{M}\underline{d}$ of Section 2 can be computed. This is the subject of the next section.

3.2. Internal kinematics

Vector ${}^{M}\underline{d}$ will be needed for tracking purposes. As seen from (2.6) and (2.7), this vector may be extracted from a first order expansion of ${}^{M}D$. However, ${}^{M}\underline{d}$ is more easily found directly. In this way, a further understanding of the internal kinematics of the sensor will be gained before starting the development of the of the exact transformation ${}^{M}D$.

First, imagine that the two parts of the sensor in Fig. 3.1 are centered, so that their coordinate frames coincide. Then ${}^{M}D = I$, ${}^{M}\underline{d} = \underline{0}$ and $\underline{p} = \underline{0}$, (3.1). From this position, the tool marker may be given a translational displacement along the ${}^{M}x$, ${}^{M}y$ or ${}^{M}z$-axis, or it may be rotated about one of the same axes. By observing the corresponding change in $\underline{p}$, the following relations appear

$$\begin{aligned} d_1 &= \tfrac{1}{2} p_1 + \tfrac{1}{2} p_3 \; ; \; d_2 = \tfrac{1}{2} p_2 + \tfrac{1}{2} p_4 \; ; \; d_3 = p_5 \\ \delta_1 &= \tfrac{1}{b} p_4 - \tfrac{1}{b} p_2 \; ; \; \delta_2 = \tfrac{1}{b} p_1 - \tfrac{1}{b} p_3 \; ; \; \delta_3 = p_6 \end{aligned} \tag{3.2}$$

If desired, this may be given in matrix notation.

$${}^{M}\underline{d} = J_{pM}\underline{p} \tag{3.3}$$

The development of ${}^{M}D$ as a function of $\underline{p}$ will be carried out in

steps. First, an intermediate homogeneous transformation B_1 will be found, which is a function of p_1 through p_4 only. This will be equal to ${}^{M}D$ as long as p_5 and p_6 are zero:

$$B_1 = {}^{M}D \qquad <=> \qquad p_5 = p_6 = 0$$

Then a second transformation, B_2, will be found such that

$$B_2 = {}^{M}D \qquad <=> \qquad p_1 = p_2 = p_3 = p_4 = 0$$

and

$${}^{M}D = B_1 B_2 \tag{3.4}$$

These two steps may be divided into substeps, so that ${}^{M}D$ eventually may be obtained by applying a sequence of rotations and translations in the form of homogeneous transformations.

First, radial displacement is expressed, i.e. translation along the ${}^{M}x$ and ${}^{M}y$-axes of Fig. 3.1. This motion is described by the transformation

$$S_1 = \begin{bmatrix} & & d_1 \\ & I & d_2 \\ & & 0 \\ & \underline{0}^T & 1 \end{bmatrix} \tag{3.5}$$

where d_1 and d_2 are defined by (3.2). The use of $\underline{d}$ rather than $\underline{p}$ simplifies the writing.

Next, the rotation about the ${}^{M}x$ and ${}^{M}y$-axes is described. This will be done by means of a single rotation about an imaginary vector $\underline{k}$, which may be obtained from the rotational quantities δ_1 and δ_2 of $\underline{d}$ (3.2).

$$\underline{k} = (\delta_1^2 + \delta_2^2)^{-\frac{1}{2}} [\delta_1 , \delta_2 , 0]^T \tag{3.6}$$

This vector is normalized, and it is seen that the vector is not defined if δ_1 and δ_2 are both zero. In this case, there is no radial rotation, and the complete step may be omitted.

If $\underline{k}$ is defined, a transformation matrix describing a rotation about this vector may be found (Paul, 1981).

$$S_2 = \begin{bmatrix} k_1^2\text{verse}\theta+\cos\theta & k_1k_2\text{verse}\theta & k_2\sin\theta & \\ k_1k_2\text{verse}\theta & k_2^2\text{verse}\theta+\cos\theta & -k_1\sin\theta & \underline{0} \\ -k_2\sin\theta & k_1\sin\theta & \cos\theta & \\ & \underline{0}^T & & 1 \end{bmatrix} \qquad (3.7)$$

where θ is the angle of rotation, and $\text{verse}\,\theta = 1-\cos\theta$. As well as vector $\underline{k}$, trigonometric functions of θ may be expressed in terms of δ_1 and δ_2:

$$\sin\theta = (\delta_1^2+\delta_2^2)^{\frac{1}{2}}(1+\delta_1^2+\delta_2^2)^{-\frac{1}{2}} \qquad (3.8)$$

$$\cos\theta = (1+\delta_1^2+\delta_2^2)^{-\frac{1}{2}} \qquad (3.9)$$

$$\text{vers}\,\theta = [(1+\delta_1^2+\delta_2^2)^{\frac{1}{2}} -1](1+\delta_1^2+\delta_2^2)^{-\frac{1}{2}} \qquad (3.10)$$

S_2 is obtained by inserting this, and (3.6), into (3.7). This completes the development of B_1 (3.4), which may be computed by

$$B_1 = S_1S_2 \qquad (3.11)$$

The two last transformations express the translation along and the rotation about the z-axis of the intermediate coordinate system MB_1. The translational transformation matrix is given by

$$S_3 = \begin{bmatrix} & & 0 \\ & I & 0 \\ & & d_3 \\ & \underline{0}^T & 1 \end{bmatrix} \tag{3.12}$$

and the rotational matrix by

$$S_4 = \begin{bmatrix} \cos\delta_3 & -\sin\delta_3 & 0 & \\ \sin\delta_3 & \cos\delta_3 & 0 & \underline{0} \\ 0 & 0 & 1 & \\ & \underline{0}^T & & 1 \end{bmatrix} \tag{3.13}$$

Now, the second intermediate transformation may be obtained by

$$B_2 = S_3 S_4 \tag{3.14}$$

and the complete positional deviation transformation by

$$^{M}D = B_1 B_2 = S_1 S_2 S_3 S_4 \tag{3.15}$$

Obviously, the exact computation of ^{M}D is complicated. However, as pointed out in Section 2.2, it need not be done in real time as long as $^{M}\underline{d}$ is sufficiently accurate for tool tracking.

4. TRAINING CONFIGURATIONS

An example of the use of the positional deviation sensor was given in Section 2. As mentioned, the operator holds the tool and the robot follows in order to learn the task. However, a second configuration is possible, where the tool is fixed to the manipulator in its normal manner. In this case, the operator leads the manipulator by means of a handle, as outlined in Fig. 4.1. This approach closely resembles the use of a force sensing handle, as described in Section 1, except that in the present case there is no mechanical contact between the handle and the manipulator. Characteristics of the two approaches will be discussed in Section 4.1. The other item to be discussed, concerns the kinematic structure of the sensor. This may be compared to the structure of the robot task, the tool or the manipulator at hand. A general discussion of this is presented in Section 4.2. Some special remarks on the training of paint spraying robots are given in Section 4.3.

4.1. Discussion of two configurations

The first approach, where the tool is held by the operator, can be considered as a special case of programming by means of remote positional sensing. By mounting the sensor to the manipulator, its short range is increased to include the manipulator´s workspace. Since a short-range remote positional sensor clearly picks up less disturbance than a full-range device, its use may lead to a more accurate recording of the tool motion. However, by (2.11) this also depends on the accuracy of the manipulator at hand. In any case, the presence of the manipulator gives the operator more feedback. It guarantees that the tool stays within the feasible workspace, and that obstacles are avoided. The similarities between this approach and the use of remote sensing are

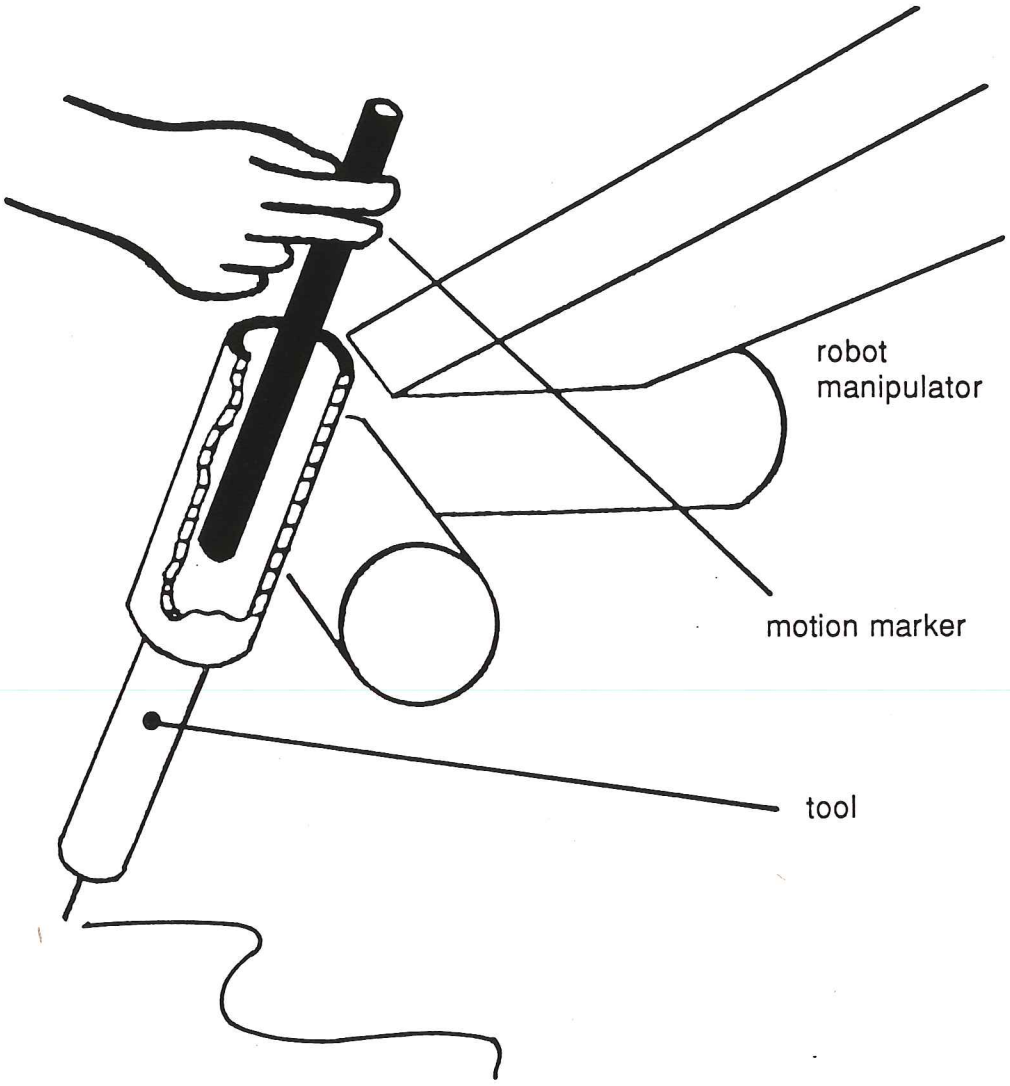

Figure 4.1. Assisted tool operation.

illustrated in Fig. 4.2. The second approach, where the tool is fixed to the manipulator, clearly resembles the use of a force sensing handle. It is more correct, however, to consider it as a "close up" case of remote control lead-through programming. This may be realized by comparing Fig. 4.3 to Fig. 4.1. The close distance to the manipulator enables the operator to do more precise programming.

The differences between programming by hand-operated tool and assisted tool operation are mainly due to the different types of interaction present. Using the first approach, the operator wields direct control of the tool. This enables the programming of swift, complex motion. Furthermore, if physical contact is made between the tool and the environment, this is felt by the operator, and appropriate action may be taken. By assisted tool operation, where the tool is fixed to the manipulator, any desired compliant action must be programmed in advance and carried out by the manipulator. However, the missing contact between the tool and the operator is an advantage whenever contact forces or gravitational forces will wear out the operator. During the programming of point-to-point motion, it may also be convenient to be able to lock the tool in a certain position. This may only be done when the tool is fixed to the manipulator. In this case, even a mode for fine motion may be included. This may enhance a point-to-point programming system considerably, but does not rule out the use of a hand-operated tool for this application. The swift and precise motion which becomes available in this case may speed up the programming of complex motion, which usually is described by a large sequence of closely spaced positions.

The tracking and recording system for the case of a hand-operated tool is outlined in Section 2.2, Fig. 2.3, where the need for sensor accuracy is discussed as well. Assisted tool operation requires a somewhat different recording system, since the true tool motion in this case is given by the homogeneous transformation equation

$$C = TE \tag{4.1}$$

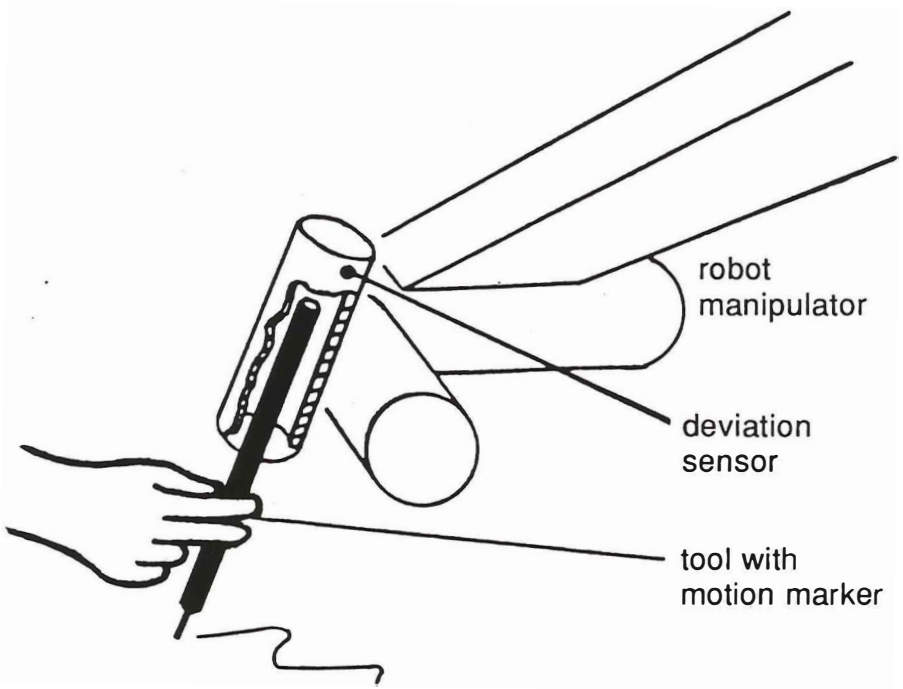

A: Deviation sensing

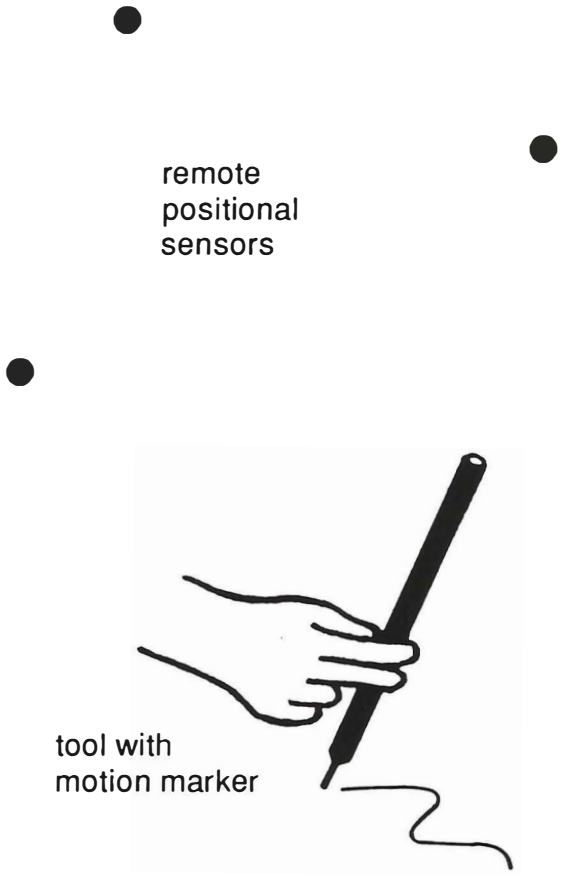

B: Remote sensing

Figure 4.2. Hand operated tool.

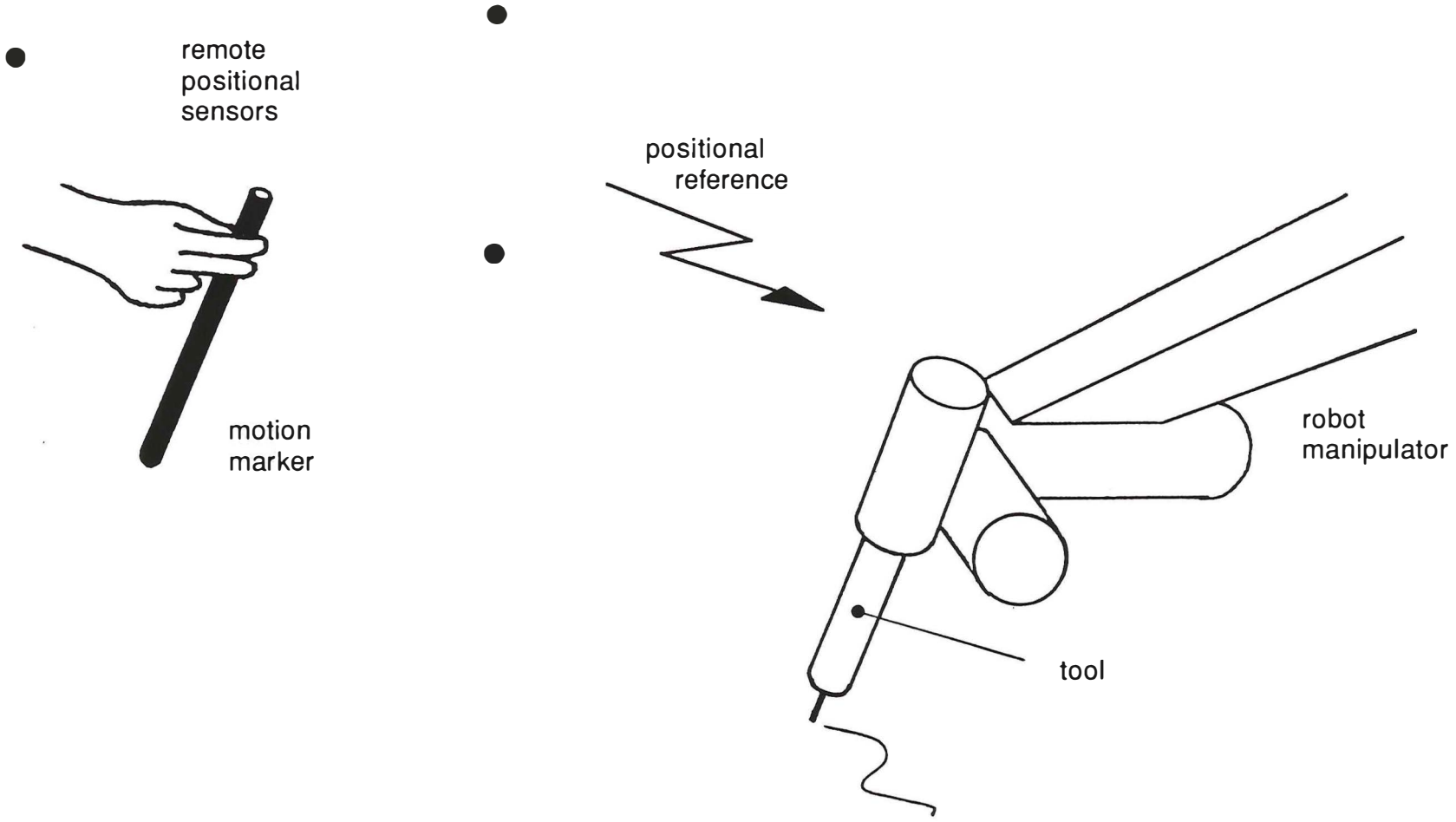

Figure 4.3. Remote control lead-through. Compare with Fig. 4.1.

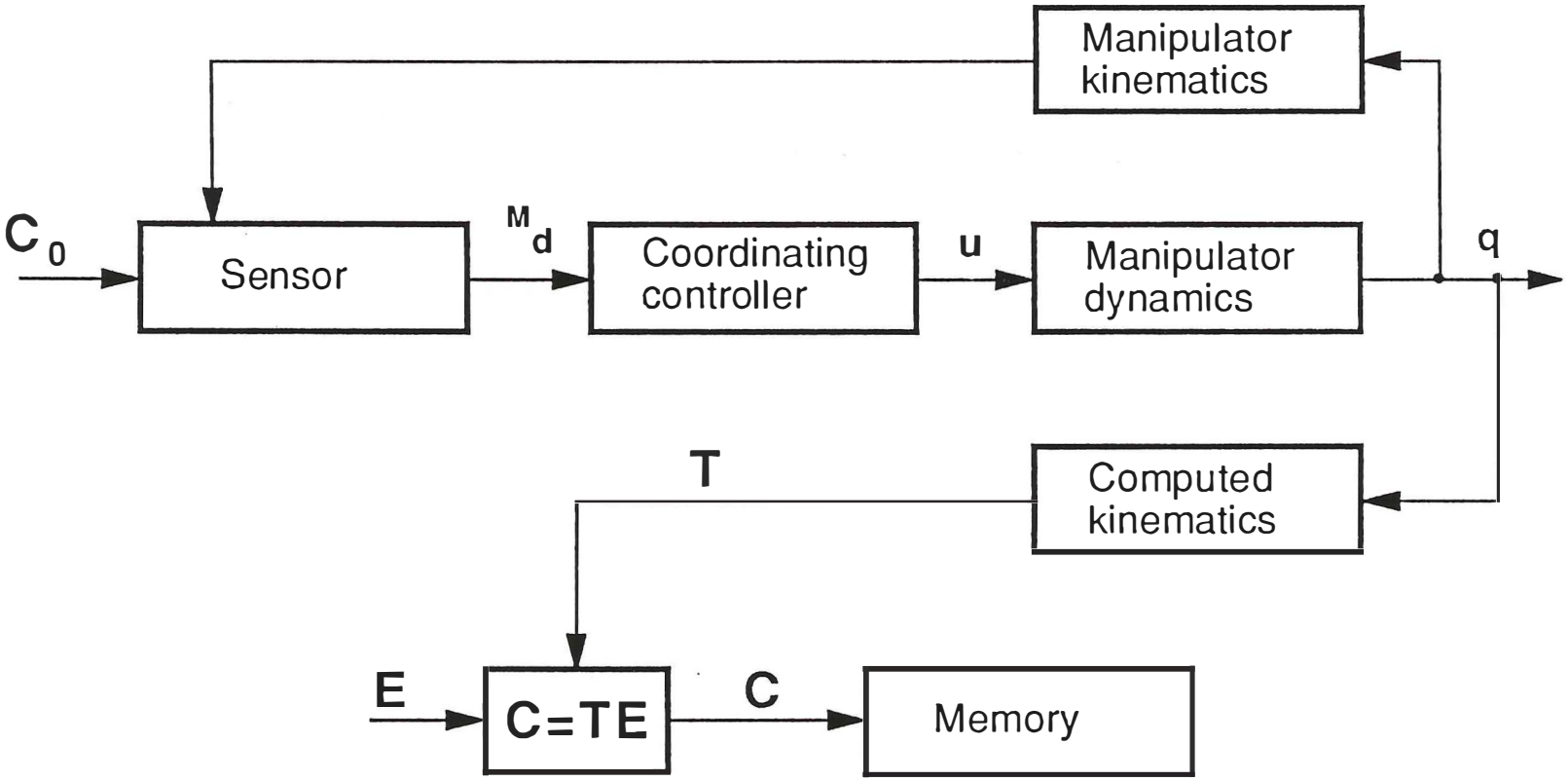

Figure 4.4. Tracking and recording system for assisted tool operation.

where transformation E carries the tool description. Obviously, when comparing (4.1) to (2.8),

$$E = {}^{T}C$$

except that in the present case, E (and ${}^{T}C$) is fixed. Because of this, the recorded program does not depend on the positional deviation sensor at all. The modified recording system is shown in Fig. 4.4. Since in this case the only purpose of the sensor is to guide the manipulator, it does not need to be as accurate as when using a hand-operated tool. Hence, less computational effort will be necessary.

4.2. Kinematic structures

Some of the kinematic properties of the sensor are summed up by describing the device as cylindrical. Referring to Figs. 3.1 and 3.3, a more rigid formulation of properties may be given. The radial deviation, represented by the intermediate deviation quantities p_1 through p_4, is firmly restricted such that

$$p_i^2 + p_{i+1}^2 < (a_1 - a_2)^2 \qquad i=1 \text{ or } 3 \qquad (4.3)$$

where a_1 denotes the inner radius of the outer cylinder and a_2 the radius of the marker. In theory, axial translation and rotation, p_5 and p_6, are not restricted. These properties define "cylindrical" in the present context. In practice, axial motion may also be restricted, however not as firmly as is the case for radial motion. Restrictions may be due to the finite length of the marker, or the layout of electrical cables. Even if free motion is allowed, the quality of the measurements must be taken into account. The measurement quantity y_5, corresponding to p_5, gradually saturates as $|p_5|$ increases. However, the quality is acceptable as long as

$$-b/2 \lesssim p_5 \lesssim b/2 \tag{4.4}$$

where b is defined in Fig. 3.3. When it comes to the sixth measurement, three possibilities exist. Since there is no inherent restriction on p_6, no corrective action by the manipulator needs to be taken in this direction. Then, y_6 must be distinct for all possible values of p_6. At least for

$$-\pi/2 \leq p_6 < \pi \tag{4.5}$$

In some cases y_6 is of sufficient quality only for small values of p_6, such as

$$-\pi/8 \lesssim p_6 \lesssim \pi/8 \tag{4.5b}$$

In this case, corrective action must be taken in order to keep p_6 within these limits. The cylindrical shape makes the sensor suitable for some common 5 d.o.f. applications, such as arc welding, deburring and paint spraying. In such cases, the tool may have the same cylindrical nature as the deviation sensor (Figs. 2.1, 2.2, 4.1, 4.2 and 4.3). The sixth measurement will be unnecessary if the 5 d.o.f. manipulator is incapable of tracking the corresponding motion. A prerequisite for this simplified configuration is that the symmetry axes of the tool and the sensor coincide when using a hand-operated tool. Assisted tool operation requires that the axes are at least parallel.

A fully equipped sensor may be used for 6 d.o.f. applications, either using the hand-operated tool approach or assisted tool motion. In addition, a few hybrid approaches may occasionally be useful. These take advantage of the cylindrical shape of the sensor. In Fig. 4.5, the sensor replaces the sixth servo of the manipulator. Here, the first 5 servos are programmed by a positional deviation sensor in the usual sense, whereas the 6th servo is in principle programmed by a remote positional sensor. The configuration in Fig. 4.6 is a special case of programming by remote control. The sensor is still fixed to link no. 5 of the

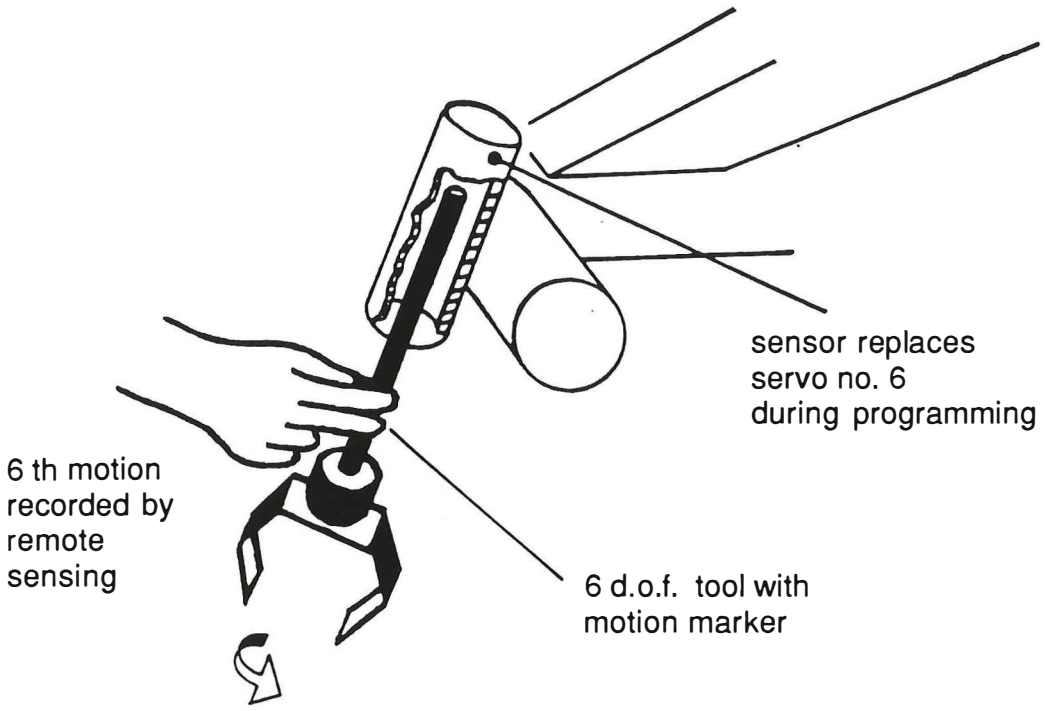

Figure 4.5. Hand operated tool. Hybrid.

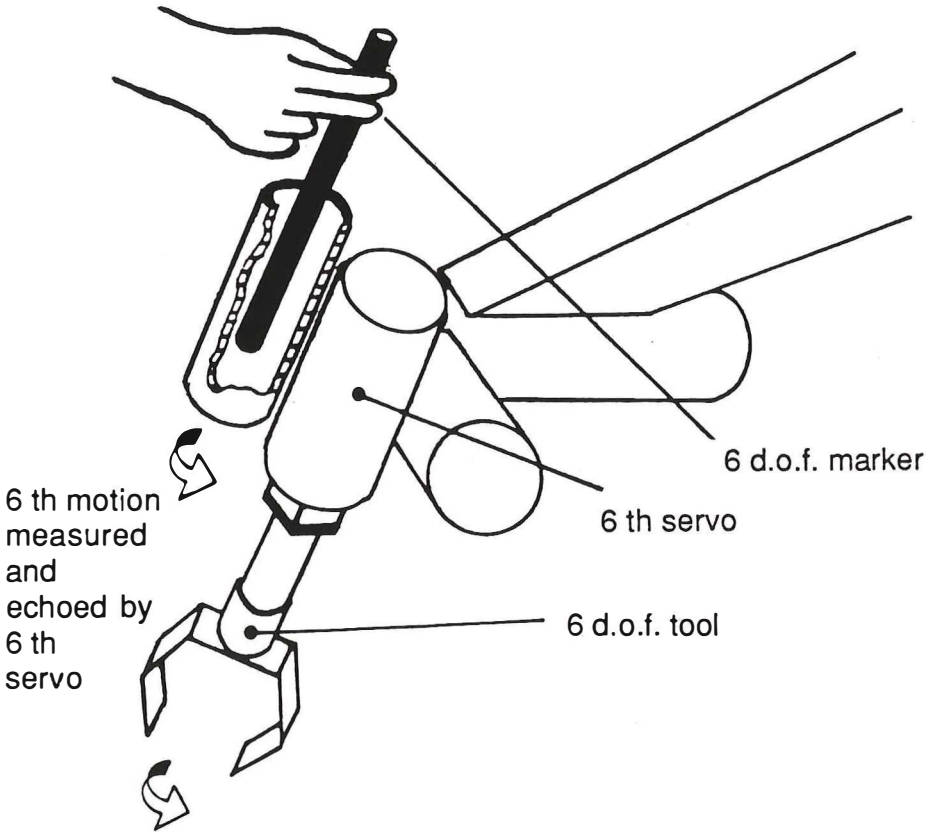

Figure 4.6. Assisted tool operation. Hybrid.

manipulator, and the first 5 servos track the teach-handle marker. The 6th servo reflects p_6- motion, usually 1 to 1.

Special problems arise during the teaching of manipulators with redundant degrees of freedom. This may in some cases be solved by adding some automatic accomodation scheme using a manipulability index (Yoshikawa, 1985), perhaps combined with an obstacle avoidance scheme (Khatib, 1985). In any case, some means for manual accomodation, such as an additional teach pendant, should be provided. A simple case of redundancy is presented below.

4.3. Paint spraying

For many paint spraying applications, a 5 d.o.f. manipulator will be sufficiently general. This is due to the usual rotational symmetry of the spray gun and the fan of paint, which gives it a 5 d.o.f. nature. Since the y_6-measurement may be omitted in this case, p_6-motion has no direct influence on the recorded program. The motion may thus simply be used to increase the comfort of the programmer.

Even if paint spraying often is a 5 d.o.f. application, one may use manipulators with more degrees of freedom in order to access otherwise unreachable areas of the object to be painted. It is quite common to use standard 6 d.o.f. manipulators with the spray gun mounted so that the extra orientational servo simply extends the range of the other wrist servos, Fig. 4.7. The same configuration also gives the system some capability for obstacle avoidance. Such systems may be trained either by using a fully equipped sensor, or by a 5-measurements sensor with an additional 1 d.o.f. teach pendant.

Paint spraying is not always a 5 d.o.f. task. In some cases the fan is given a noncircular shape, and an extra orientational servo is needed to rotate its impact image, Fig. 4.8. Including this, three possible uses of additional d.o.f. have been mentioned:

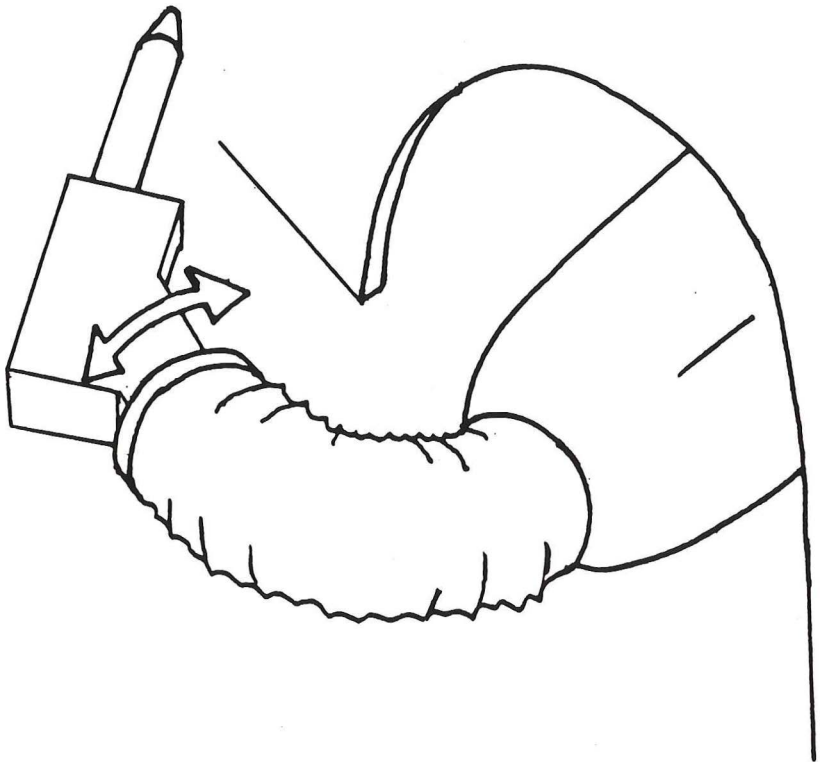

Figure 4.7. Extended wrist motion. 6th servo used to bend the tool backwards.

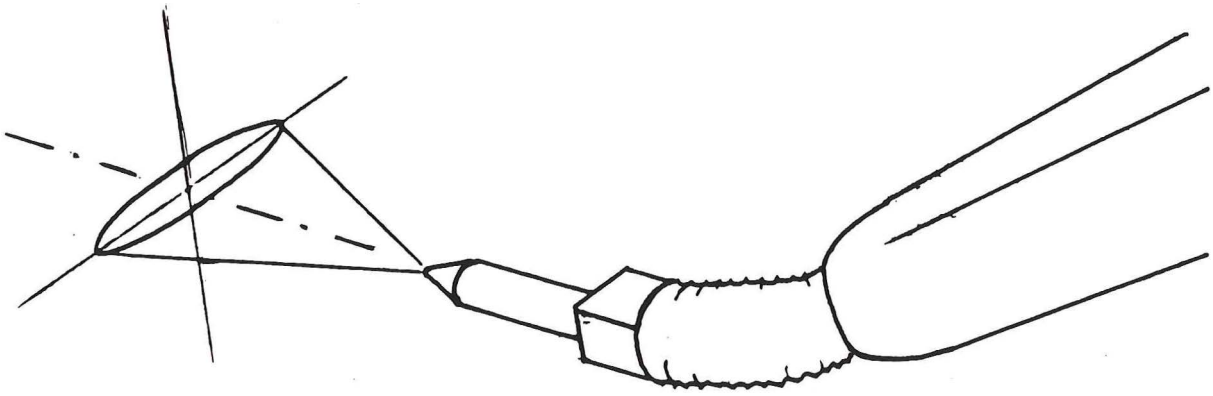

Figure 4.8. Noncircular fan.

- programmer´s accomodation
- extended wrist motion
- fan orientation

If all uses are desired, an 8 d.o.f. system will result which cannot be controlled only by the motion of the marker. Fig. 4.9 indicates a solution to the problem which requires the support of the operator´s second hand. This is by no means the only solution, considering the number of communication channels wielded by a human being. Research on interfacing these to computers seems to be growing (Foley, 1987; Bolt, 1984), and some of the results may be applicable in the present case.

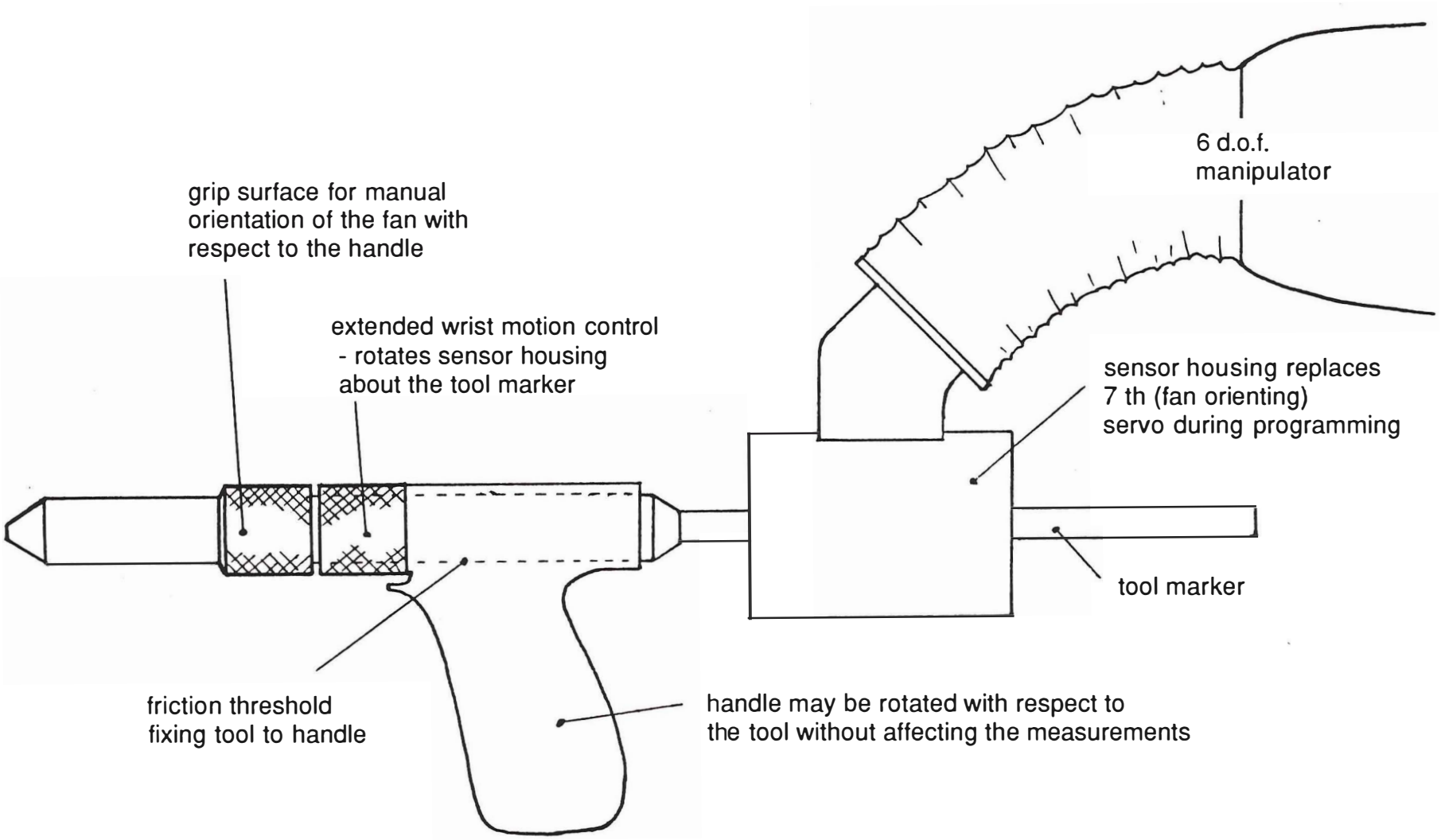

Figure 4.9. 8 d.o.f. system for paint spraying.

5. TRACKING SYSTEM

The success of the complete training system relies on the presence of a control system which makes the manipulator follow the tool closely at all times. Especially, real-time training of paint-spraying robots requires outstanding velocity and accelerational capabilities. The purpose of this section is to outline a coordinating control structure and to point out factors that may limit its performance.

5.1. Servo coordination

Very often, playback control systems work in servo coordinates. This means that any motion reference is converted into a vector of servo references. A corresponding vector of control errors is used to compute the required action. With the previously described positional deviation sensor, no servo reference is available. The reference may of course be computed by first finding the corresponding homogeneous transformation matrix for the manipulator,

$$T_0 = T^T_D \tag{5.1}$$

where ^T_D is given by (2.9). The required servo motion may be obtained from T_0. However, a computationally more efficient approach is to produce the control error in servo coordinates directly from the positional deviation sensor data. The relationship may be represented by the first order approximation

$$^M\underline{d} = J_{eM}\underline{e} \tag{5.2}$$

where J_{eM} is the Jacobian matrix $\partial\,^M\underline{d}/\partial\underline{e}$. If it is nonsingular,

the control error may be computed by

$$e = J_{Me}\,{}^{M}d \quad \text{where} \quad J_{Me} = J_{eM}^{-1} \tag{5.3}$$

The existence of an inverse Jacobian depends on the manipulator configuration. Usually, J_{Me} will not be computed explicitely. Instead ${}^{M}\underline{d}$ will go through a sequence of intermediate differential tranformations until finally $\underline{e}$ is obtained. The coordination algorithm which has been implemented on the TR 400 S manipulator is based on wrist partitioned kinematics (Hollerbach, 1983; Dessen, 1985). The scheme, which is described in Appendix A1, first transforms the error into wrist coordinates

$${}^{M}\underline{d} \longrightarrow {}^{T}\underline{d} \quad , \quad \text{cf.(A1.22)}$$

Then, errors in the first three joints are found by considering the translational elements of ${}^{T}\underline{d}$. Taking into account the change in orientation which is due to the computed change in the first three servos, errors in the wrist servos are found from the orientational elements of ${}^{T}\underline{d}$. Further notes on partitioning are found in Section 10.2.

Once $\underline{e}$ is given, controllers working in joint coordinates may be applied. The usual approach at this level is to employ separate controllers for each servo, neglecting possible coupling between the actuators. In many cases, this assumption is reasonable though not completely true. In the present case, coupling will be neglected by assuming it to be taken care of by internal control. More precisely, internal speed control of N servos is assumed with a resulting transfer matrix

$$G(s) = \mathrm{diag}[g_1(s),\ g_2(s),\ \ldots,\ g_N(s)] \tag{5.4}$$

which relates actual speed and speed reference by

$$v_i(s) = g_i(s)v_{i0}(s)$$

Seen from an added positional controller, the process transfer matrix is

$$H(s) = \frac{1}{s} G(s) = \text{diag}[\frac{1}{s} g_1(s), \ldots, \frac{1}{s} g_N(s)] \qquad (5.5)$$

The process is illustrated in Fig. 5.1. In practice H(s) will include several off-diagonal coupling terms. However, these are assumed to be small as coupling is taken care of by the speed controller.

The outlined structure may be considered as a hierarchical control system (Mesarovic, 1970; Findeisen, 1980) where the supremal (higher) level is a coordinating positional controller whereas the infimal (lower) level performs decoupling speed control. This partitioning will be retained throughout since it is believed to give a better understanding of the control problem at hand.

5.2. Performance

It is of interest to have a rough idea of the expected tracking performance. For this purpose, a simple 1 d.o.f. positional control system will be considered. Conforming to (5.5), the process transfer function is written

$$h(s) = \frac{1}{s} g(s) \qquad (5.6)$$

The control system is shown in Fig. 5.2, and will be analyzed in terms of its open-loop transfer function, which is assumed to be stable. At first, a proportional controller with gain k_p will be applied. The closed-loop system will be stable whenever

$$k_p < \alpha\omega_\varphi = \omega_x \qquad (5.7)$$

where ω_φ is the -180^o phase shift frequency for $h(j\omega)$, and

$$\alpha = |g(j\omega_\varphi)|^{-1} \qquad (5.8)$$

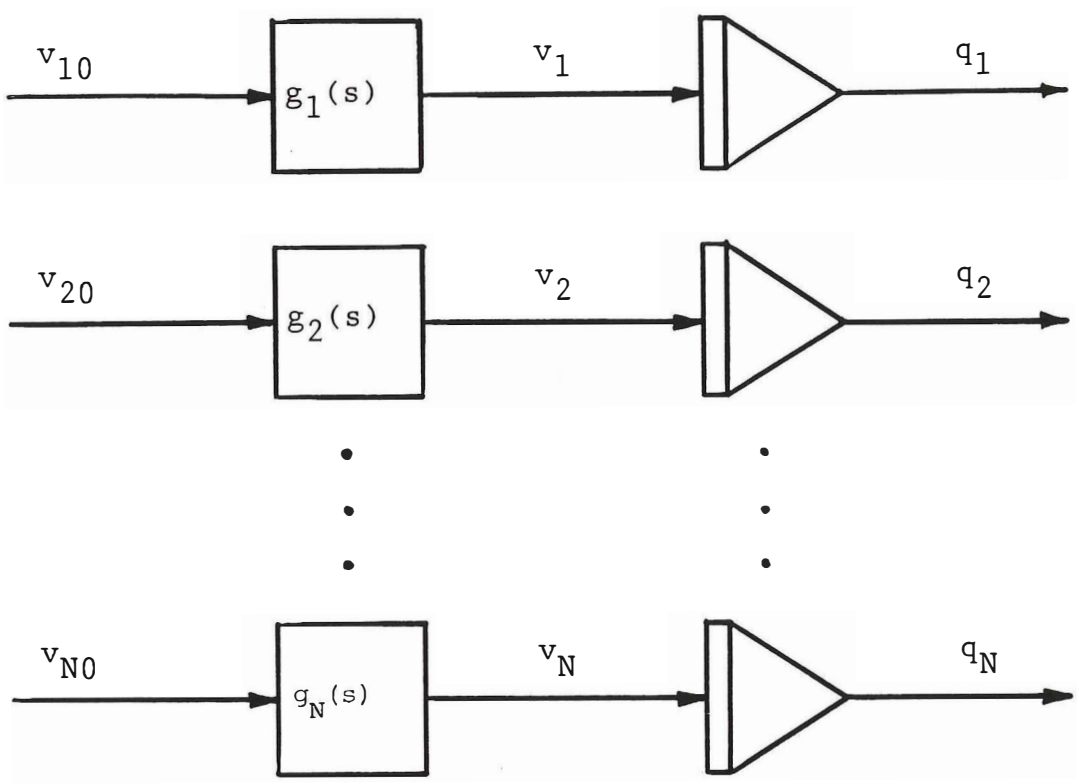

Figure 5.1. Process as seen from the coordinating controller.

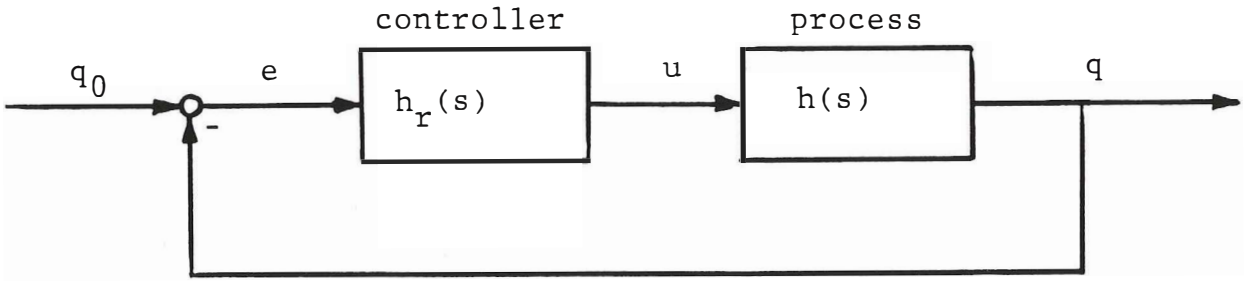

Figure 5.2. Simple positional servo.

Bode plots of the open-loop system are given in Fig. 5.3, and (5.7) follows from the Bode-Nyquist stability criterion.

In order to obtain a few simple expressions describing performance, controllers are assumed to be designed using the Ziegler-Nichols method where control parameters are based on the values of ω_x and φ_φ. For a proportional (P) controller, the method yields

$$h_r(s) = k_p = 0.5\ \omega_x \tag{5.9}$$

The resulting open-loop transfer function becomes

$$h_o(s) = h_r(s)h(s) \tag{5.10}$$

Tracking performance will be studied in terms of the closed-loop error transfer function

$$N(s) = e(s)/q_o(s) \tag{5.11}$$

From Fig. 5.2, the relationship between reference and control error is obtained as

$$e(s) = q_o(s) - q(s) = q_o(s) - h_o(s)e(s) \tag{5.12}$$

so that

$$N(s) = \frac{e(s)}{q_o(s)} = \frac{1}{1 + h_o(s)} \tag{5.13}$$

This transfer function is of major interest since it in the context of Section 2 relates the important quantities D (positional deviation) and C (tool motion). Assuming that the control error amplitude is restricted by

$$|e(j\omega)| < E \tag{5.14}$$

for all real ω, the reference is restricted by

$$|q_o(j\omega)| < E|N(j\omega)|^{-1} \tag{5.15}$$

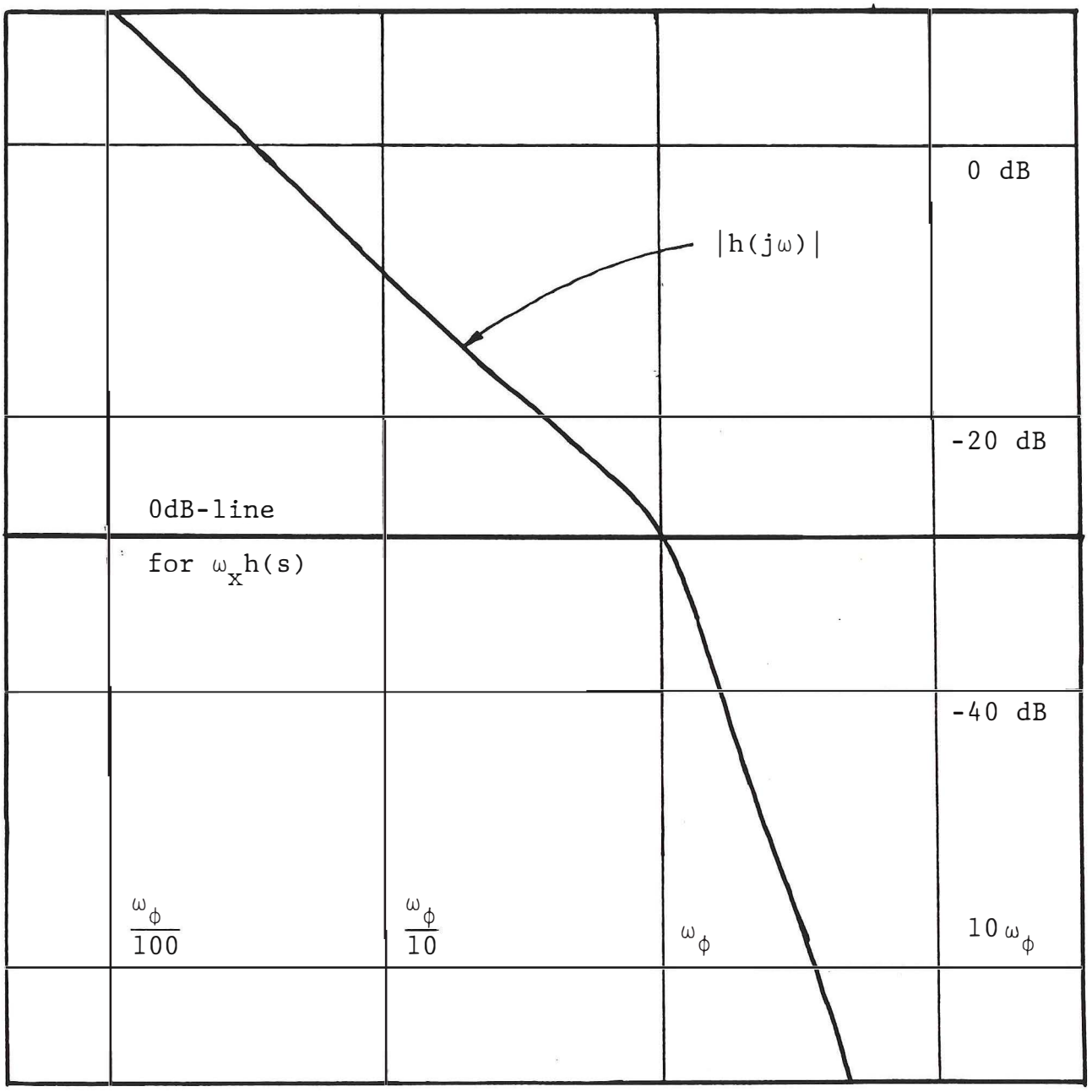

Figure 5.3. Amplitude of transfer function $h(j\omega)$. Application of controller $h_r(j\omega) = \omega_x$ shifts the 0dB-line as indicated. The crossing of this line at $\omega = \omega_\varphi$ shows that the stability limit has been reached.

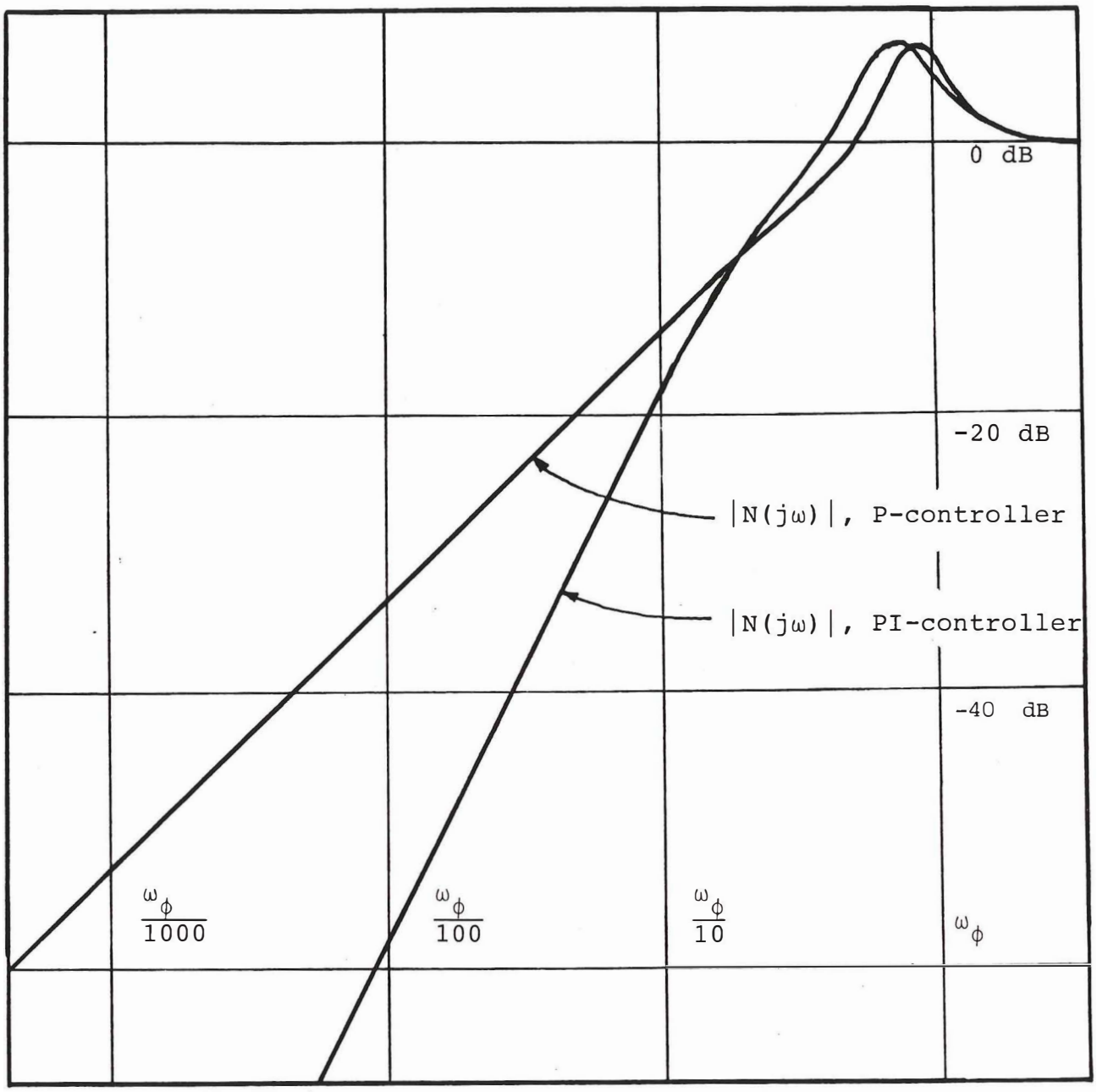

Figure 5.4. Amplitudes of typical closed-loop error transfer functions for P and PI type servos. The lower amplitude, the better performance.

Hence, the allowed tool motion amplitude at any fixed, single frequency ω may be read almost directly from Fig. 5.4.

By studying the asymptotical behaviour of N(s) as s approaches zero, it is seen that

$$\lim_{s\to 0} \frac{sE}{N(s)} = E\, k_p = 0.5\, E\, \omega_x \tag{5.16}$$

This implies a maximum steady state velocity

$$v_p = 0.5\, E\, \omega_x = 0.5\, E\, \alpha\, \omega_\varphi \tag{5.17}$$

Applying the numerical values E = 1 cm and ω_x = 20 rad/s, which are typical, v_p = 10 cm/s is obtained. Thus it is seen that the mere use of proportional control may yield low performance.

A proportional + integral (PI) controller, where

$$h_r(s) = k_p \frac{1 + T_i s}{T_i s} \tag{5.18}$$

will by the Ziegler-Nichols method be assigned

$$k_p = 0.45\, \omega_x \quad ; \quad T_i = 5/\omega_\varphi = 5\alpha/\omega_x \tag{5.19}$$

This time, the asymptotical behaviour of N(s) gives

$$\lim_{s\to 0} \frac{s^2 E}{N(s)} = E\, \frac{k_p}{T_i} = \frac{0.45}{5\alpha}\, E\, \omega_x^2 \tag{5.20}$$

which implies a maximum steady state acceleration

$$a_{PI} = \frac{0.45}{5\alpha}\, E\omega_x^2 = 0.09\, E\, \alpha\, \omega_\varphi^2 \tag{5.21}$$

Letting α = 1, a_{PI} = 36 cm/s^2 is obtained. Compared to the use of a proportional controller, this is an improvement. However, the results are still not satisfactory. Performance measures v_p and

a_{PI} are used several places in this text in place of function N(s) since they give an immediate understanding of important properties of the system in question. Whenever v_P is used, it is understood that the underlying closed-loop error transfer function has the slope +20 dB/decade at low frequencies. Whenever a_{PI} is used, this slope is understood to be +40 dB/decade.

For both P and PI control, Bode plots of the resulting error transfer functions are shown in Fig. 5.4. As seen from (5.17) and (5.21), the performance depends on the deviation sensor by E and on g(s) by α and ω_φ. Because of this, attempts will be made to increase these factors. Trivially, E may be increased by enlarging the positional deviation sensor. A second, related approach is to coordinate the servos so that maximum use is made of the sensor workspace. This is considered in Section 6. Due to the second order dependence on ω_φ in (5.20), means for improving the infimal control system are of special interest. Such means are discussed in Sections 7 and 8.

5.3. First experiments

The control structure outlined in Section 5.1 has been implemented on the 5 d.o.f. TR 400 paint spraying manipulator. Experiments were carried out at Trallfa Robot AS, Bryne, Norway and were part of the initial feasibility study. The manipulator is described in Appendix A1, and the 5-measurement positional deviation sensor in Appendix A5. The control system hardware, Fig. 5.5, consisted of two almost separate units, one of which contained the original playback, control and administration system.

The second unit, a Trallfa TSM (Trallfa, 1986) contained the experimental control system. The TSM-unit consists of a TMS 99105 microprocessor board and an adjoint input-output board with a fixed cycle time of 10 ms. The hardware allows skewed sampling of the 10 measurement solenoids, output of 5 servo control values and reception of the joint displacement values needed to compute the manipulator Jacobian. Conversion from solenoid measurement values

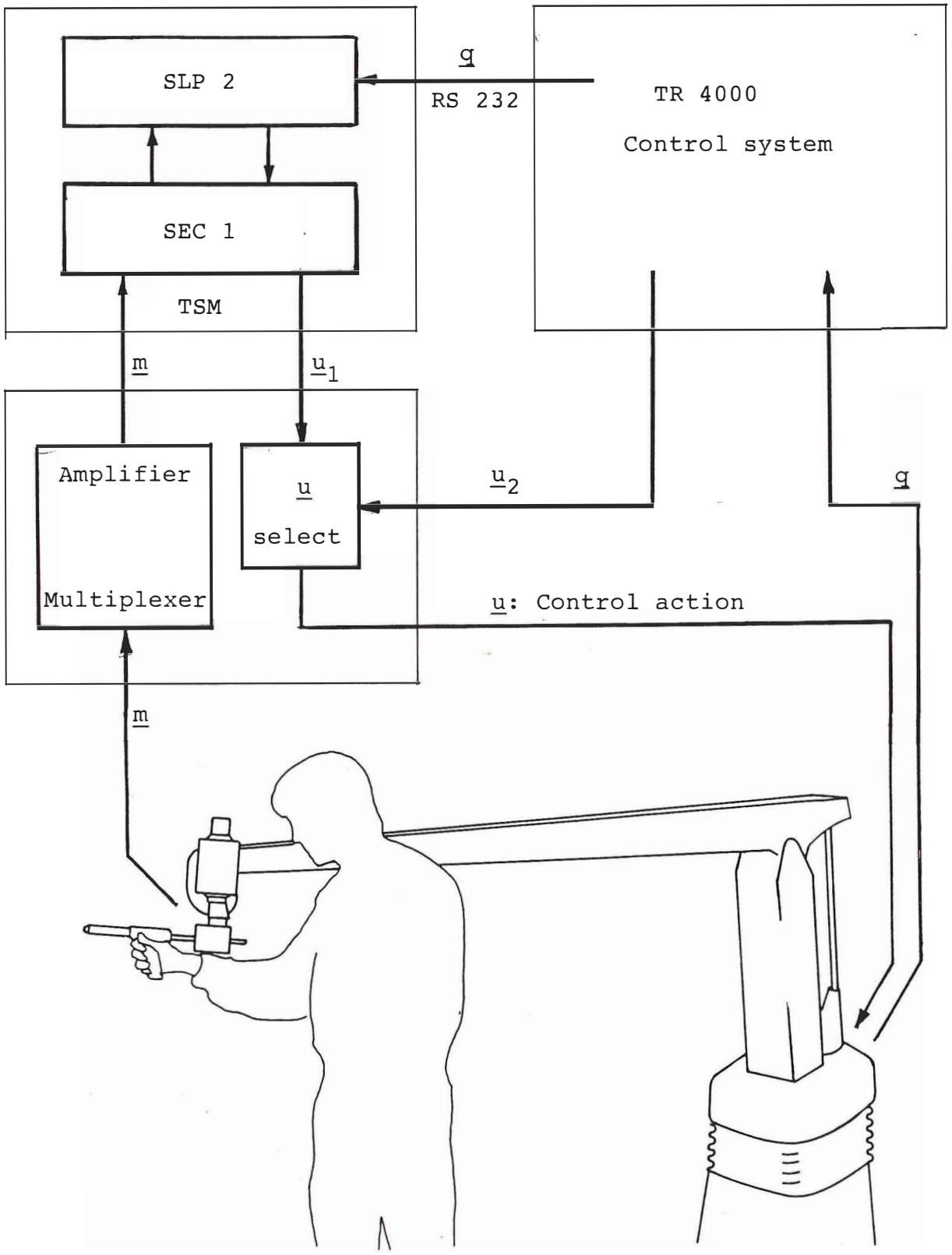

Figure 5.5. First experimental system. The experimental controller is run on the TSM-unit.

into an equivalent vector of servo control errors was done by the sequential scheme

$\underline{m} \longrightarrow \underline{y}$ Appendix A3

$\underline{y} \longrightarrow \underline{p}$

$\underline{p} \longrightarrow {}^{M}\underline{d}$ (3.2) and (3.3)

${}^{M}\underline{d} \longrightarrow \underline{e}$ Appendix A1

The subsequent controllers were of the proportional (P) or proportional + integral (PI) type. The complete scheme, which is written in integer assembly code, finishes in less than 1 ms. This is well within the limit given by the 10 ms I/O cyclus. Simplifications were made in all parts of the error conversion scheme. However, the accuracy was still reasonably good. This was verified by fixing the tool marker in an arbitrary position, and perturbing the manipulator manually around it. Actual and computed perturbations in servo coordinates were then compared. It is believed that most of the detected error was due to simplifications in the computation of the intermediate deviation vector $\underline{p}$. This will be discussed in Sections 9 and 10.

The first tests showed a tracking performance corresponding to the simple theoretical results of Section 5.2. This indicates that tool tracking is possible, at least at low speeds. Attempts to increase the performance by increasing the controller gain resulted in instable or oscillating behaviour. This was expected, however the nature of the oscillations suggested that the structural elasticities of the manipulator are of importance and should be investigated. In addition, the interaction between servos 2 and 3 seemed significant. These effects are considered theoretically in Section 7.

5.4. Force sensing handles

During the experiments described in the previous section, it was of interest to compare the described positional deviation sensor with a force sensing device. For a moment, the space between the two parts of the sensor was packed with rubber foam in order to obtain mechanical contact with a reasonable stiffness. The result was a more stable system, however the sensor workspace was reduced because of the foam, and now considerable force had to be applied in order to make the manipulator move.

Consider now the possibility of making use of the improved stability to increase the controller gains. This again will increase the performance of the system. A quick stability analysis can be made by assuming a certain stiffness k_s between the two parts of the sensor, and that the human operator represents a certain stiffness k_h. Defining the position of the operator and the manipulator as q_0 and q respectively, the position of the tool marker will be found as

$$q_m = \frac{k_s q + k_h q_0}{k_s + k_h} \tag{5.22}$$

The control error is defined as

$$e = q_0 - q$$

whereas the measured control error is

$$e_m = q_m - q = \frac{k_h}{k_s + k_h} e \tag{5.23}$$

This effect results in a corresponding damping of the original feedback gain, which may now be increased to

$$k_p = 0.5\ \omega_x \frac{k_s + k_h}{k_h} \tag{5.24}$$

according to (5.9) or a similar value corresponding to (5.19).

The problem is that the stiffness of the human muscular system varies according to the type of motion required, and will often increase during swift and precise motion. In that case the damping given by (5.23) will decrease, and if k_p is designed for a a lower k_h than the actual value, the system may become instable. Safe design requires a large k_h to be inserted into (5.24), and as k_h increases, k_p approaches the value given by (5.9), which is the only one that is perfectly safe.

A more detailed analysis of the situation is presented in (Hirzinger, 1982). However, the above considerations provide a simple link between the stability problems encountered with a positional deviation sensor and with a force sensing handle. Moreover, simple stability criterions have been obtained for both cases.

6. OPTIMAL COORDINATION

In the 1 d.o.f. system treated in Section 5.2, the control error magnitude was restricted by a positive constant E. When several degrees of freedom are to be coordinated, the situation becomes more complicated. Maximum control error may then be restricted by expressions such as (4.3), (4.4) and (4.5). In order to make full use of the resulting 6-dimensional volume, a taylored coordinating controller may be required.

6.1. Linear quadratic optimization

To simplify the design of the supremal control system, a quadratic performance index will be used to reflect the limitations given by the sensor. In terms of the intermediate deviation vector $\underline{p}$, this index may for instance be

$$L_1 = \frac{p_1^2 + p_2^2 + p_3^2 + p_4^2}{(a_1 - a_2)^2} + \frac{p_5^2}{(b/2)^2} + \frac{p_6^2}{\pi^2} \qquad (6.1)$$

which may be compared to (4.3), (4.4) and (4.5). This may be given in general matrix notation by

$$L_1 = \underline{p}^T Q'' \underline{p} \qquad (6.2)$$

or, using (3.3), in terms of vector ${}^M\underline{d}$ by

$$L_1 = {}^M\underline{d}^T J_{Mp}^T Q'' J_{Mp} {}^M\underline{d} = {}^M\underline{d}^T Q' {}^M\underline{d} \qquad (6.3)$$

However, since the controllers in Section 5.1 work in servo coordinates, it is convenient to express L_1 in terms of $\underline{e}$ using (5.3).

$$L_1 = \underline{e}^T J_{Me}^T Q' J_{Me} \underline{e} = \underline{e}^T Q \underline{e} \tag{6.4}$$

A similar performance index may be used to express the effort made by the servos. This will be in terms of the control vector, $\underline{u}$.

$$L_2 = \underline{u}^T P \underline{u} \tag{6.5}$$

A controller is now sought for the multivariable process

$$\underline{q}(s) = H(s) \underline{u}(s) \tag{6.6}$$

which minimizes the performance index

$$L = E(\int_{t_1}^{t_2} (\underline{e}^T Q \underline{e} + \underline{u}^T P \underline{u}) dt) \tag{6.7}$$

Here $\underline{e} = \underline{q}_0 - \underline{q}$ and E( ) denotes stochastic expectation. H(s) is given by (5.5). The solution to this problem is readily obtained obtained from the theory of linear-quadratic optimal control which requires feedback from the complete underlying state vector of (6.6). However, it is desirable at present to retain the assumption of hierarchical control made in Section 5, and thus only take feedback from the output vector $\underline{q}$.

A first approach to the solution of this problem is to assume perfect internal velocity control and take $\underline{q}$ as the state vector. The process is then simplified to

$$\underline{q}(s) = \frac{1}{s} \underline{u}(s) \tag{6.8}$$

for which the state-space model is

$$\dot{\underline{x}}_1 = \underline{u} \quad ; \quad \underline{q} = \underline{x}_1 \tag{6.9}$$

It is further assumed that the reference vector $\underline{q}_0$ is generated by the Wiener process

$$\dot{\underline{x}}_2 = \underline{v} \quad ; \quad \underline{q}_0 = \underline{x}_2 \tag{6.10}$$

where $\underline{v}$ is white noise with $E(\underline{v}) = \underline{0}$. By subtracting (6.9) from (6.10), the system

$$\dot{\underline{x}} = \underline{v} - \underline{u} \quad ; \quad \underline{e} = \underline{x} \tag{6.11}$$

appears. The optimal controller is then

$$\underline{u} = P^{-1}R\,\underline{e} \tag{6.12}$$

$$\dot{R} = RP^{-1}R - Q \quad ; \quad R\big|_{t=t_2} = 0$$

or if the substitution $P^{-1}R = S$ is made,

$$\underline{u} = S\,\underline{e}$$

$$\dot{S} = SS - P^{-1}Q \quad ; \quad S\big|_{t=t_2} = 0 \tag{6.13}$$

Assuming $t_2 - t >> \text{norm}(S^{-1})$ the stationary equation is valid:

$$SS = P^{-1}Q \tag{6.14}$$

Subject to standard conditions, this may be solved for S by diagonalization since then,

$$S = M\Lambda M^{-1} \quad <=> \quad SS = M\Lambda\Lambda M^{-1} \tag{6.15}$$

where Λ is diagonal. An alternative approach is to apply an iterational scheme based on (6.12) or (6.13). In this case, variations in S due to the always changing manipulator Jacobian are easily updated. Applying (5.3) and (6.4), (6.13) turns into

$$\underline{u} = S\,J_{Me}^{-1}\,\underline{M_d} \tag{6.16}$$

$$\dot{S} = SS - P\,J_{Me}^{T}\,Q'\,J_{Me}$$

Controller (6.12) is optimal and guarantees stability when applied to process (6.8). Applied on (6.6) however, stability is not guaranteed and must be checked. This problem is discussed in Section 6.2. If instability results, this may sometimes be mended by slight adjustments of P in (6.5). From the discussion in Section 5.2 it follows that the tracking performance is limited by the process bandwidth rather than restrictions on the control effort. This implies that controller (6.12) may not turn out to be satisfactory at all.

Still assuming the structure of the supremal controller to be

$$\underline{u} = S\underline{e} \tag{6.17}$$

optimal values for the elements of S when applied to (6.8) can be found by parametric optimization. Several methods exist for the solution of this problem, some of which are outlined below. For convenience, the performance index will be modified slightly compared to (6.7).

$$L = E(\underline{e}^T Q\underline{e} + \underline{u}^T P\underline{u}) \tag{6.18}$$

The value of L can be found by first inserting (6.17), resulting in

$$L = E(\underline{e}^T [Q+S^T PS]\underline{e}) \tag{6.19}$$

Laplace transformation, and the insertion of $e(s) = N(s)q_0(s)$ results in

$$L \sim \int_{-j\infty}^{j\infty} (\underline{q}_0^*(s)N^*(s)[Q+S^T PS]N(s)\underline{q}_0(s))ds \tag{6.20}$$

where * denotes the conjugate transpose. Once a scheme is avialable for the computation of L, iteration may be applied to obtain the optimal S. It is characteristic that the solution not

only depends on the performance index and the process itself, but also on the motion reference $\underline{q}_0$ applied.

Instead of applying (6.20) to obtain L, an estimate may be found from measurements of the true $\underline{e}(t)$ and $\underline{u}(t)$. This results in an experimenting, adaptive controller where the same iterational scheme as above can be used for real-time adjustments of S.

6.2. Stability

If the state-space representation of (5.5) is known, closed-loop stability may be checked by eigenvalue computation. For instance, if

$$g_i(s) = \frac{1}{1 + 2\zeta_i \frac{s}{\omega_i} + (\frac{s}{\omega_i})^2} \quad \text{for each i} \tag{6.21}$$

the state-space representation of H(s) may be

$$\dot{\underline{x}} = A\underline{x} + B\underline{u} \quad ; \quad \underline{q} = D\underline{x} \tag{6.22}$$

where

$$A = \begin{bmatrix} 0 & 0 & 0 \\ \Omega^2 & -2Z\Omega & -\Omega^2 \\ 0 & I & 0 \end{bmatrix} \quad ; \quad B = \begin{bmatrix} I \\ 0 \\ 0 \end{bmatrix}$$

$$D = [0 \quad 0 \quad I]$$

$$\Omega = \text{diag}\{\omega_i\} \quad ; \quad Z = \text{diag}\{\zeta_i\}$$

The controller corresponding to (6.17) is

$$G = [0 \quad 0 \quad -S]$$

The resulting closed-loop system matrix will be

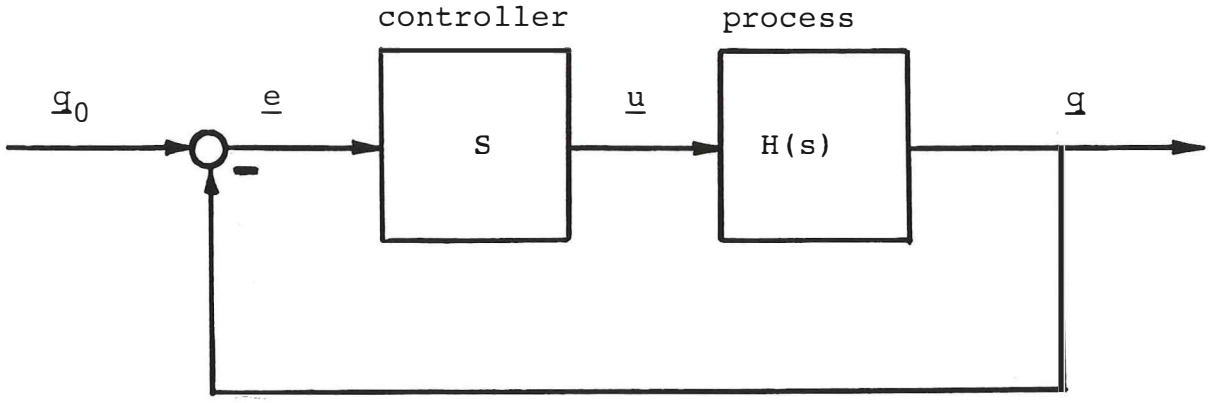

Figure 6.1. Coordinated positional servos. Non-diagonal S provides a better performance distribution.

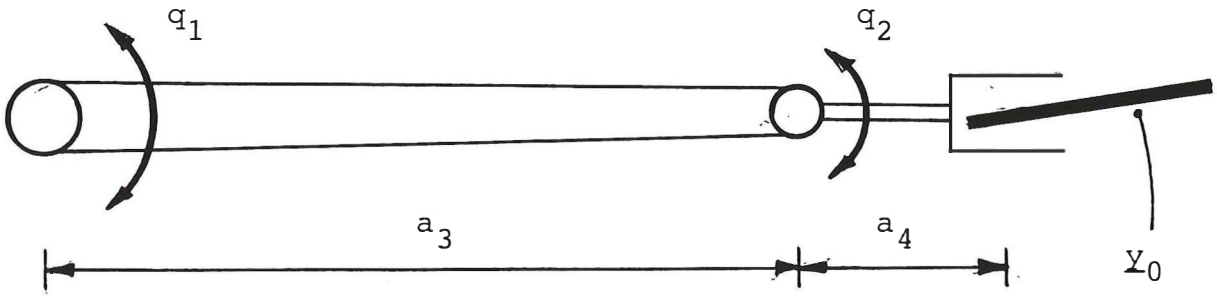

Figure 6.2. Simple optimization problem. A good controller will make servo 2 assist servo 1 in the compensation of translational errors.

$$A + BG = \begin{bmatrix} 0 & 0 & -S \\ \Omega^2 & -2Z\Omega & -\Omega^2 \\ 0 & I & 0 \end{bmatrix} \qquad (6.23)$$

and the system is stable if all its 3N eigenvalues are located in the left half of the complex plane.

Often, H(s) is more complicated than (6.21) suggests. For this reason, it may be convenient to be able to check stability by other means. This may be done by applying the generalized Nyquist stability criterion (MacFarlane, 1977). As with the standard Nyquist criterion, this is based on studying open-loop system transfer functions as complex frequency s traverses the standard Nyquist D-contour (clockwise encirclement of the right half of the complex plane).

The system shown in Fig. 6.1 has the open-loop transfer matrix

$$H_0(s) = H(s)S \qquad (6.21)$$

It is assumed to be open-loop stable. Letting s traverse the Nyquist contour D, the system is closed-loop stable if and only if the net sum of encirclements of the critical point (-1+j0) by the loci of the N eigenvalues $\{\lambda_i(s)\}$ of $H_0(s)$ is zero.

The problem of solving for the eigenvalues of H_0 is simpler than for the complete state-space system matrix A + BG. On the other hand, the eigenvalues of H_0 (s) must in principle be found for every $s \in D$. At least, their magnitudes at each crossing of the real axis must be known. In any case, due to the complexity of the eigenvalue problem, it is difficult to sort out the set of coordinating matrices S which result in a stable system.

Such results may however be found for the special case where

$$H(s) = I\, h(s) \qquad (6.25)$$

which presently means that all $g_i(s)$ in (5.5) are indentical. Then the open-loop transfer matrix is

$$H_0(s) = S\ h(s) \tag{6.26}$$

so that, if $\{\sigma_i\}$ are the eigenvalues of S,

$$\{\lambda_i(s)\} = \{\sigma_i h(s)\} \tag{6.27}$$

are the eigenvalues of $H_0(s)$. Since the stability criterion is in terms of encirclements of the critical point (-1+j0) by each $\sigma_i h(s)$, it may alternatively be stated in terms of the critical points $\{-\varrho_i\}$ and h(s), where ϱ_i is the reciprocal of σ_i. The following corollary is thus obtained:

Coordination of identical servos: If H(s) = I h(s), the system in Fig. 6.1 is stable if and only if the net sum of encirclements of the critical points $\{-\varrho_i\}$ by h(s) as s traverses D is zero.

An example is given in Fig. 6.3. Here h(s) is taken from Fig. 5.3. As can be seen, stability requires that all $-\varrho_i$ are placed left of the curve traced out by the transfer function. In the reciprocal plane, Fig. 6.4, corresponding restrictions on the eigenvalues of -S are obtained. Note that these results are due to the simplicity of (6.27), and may not be extended to the general case. The above results may however be used to give some idea of what can be gained by optimal motion coordination.

6.3. Example

As an illustration, a 2 d.o.f. system corresponding to servos 3 and 4 of the TR 400 manipulator will be made to track translational and rotational motion as shown in Fig. 6.2. Following Section 6.1, the corresponding simplified performance index L_1 can be written

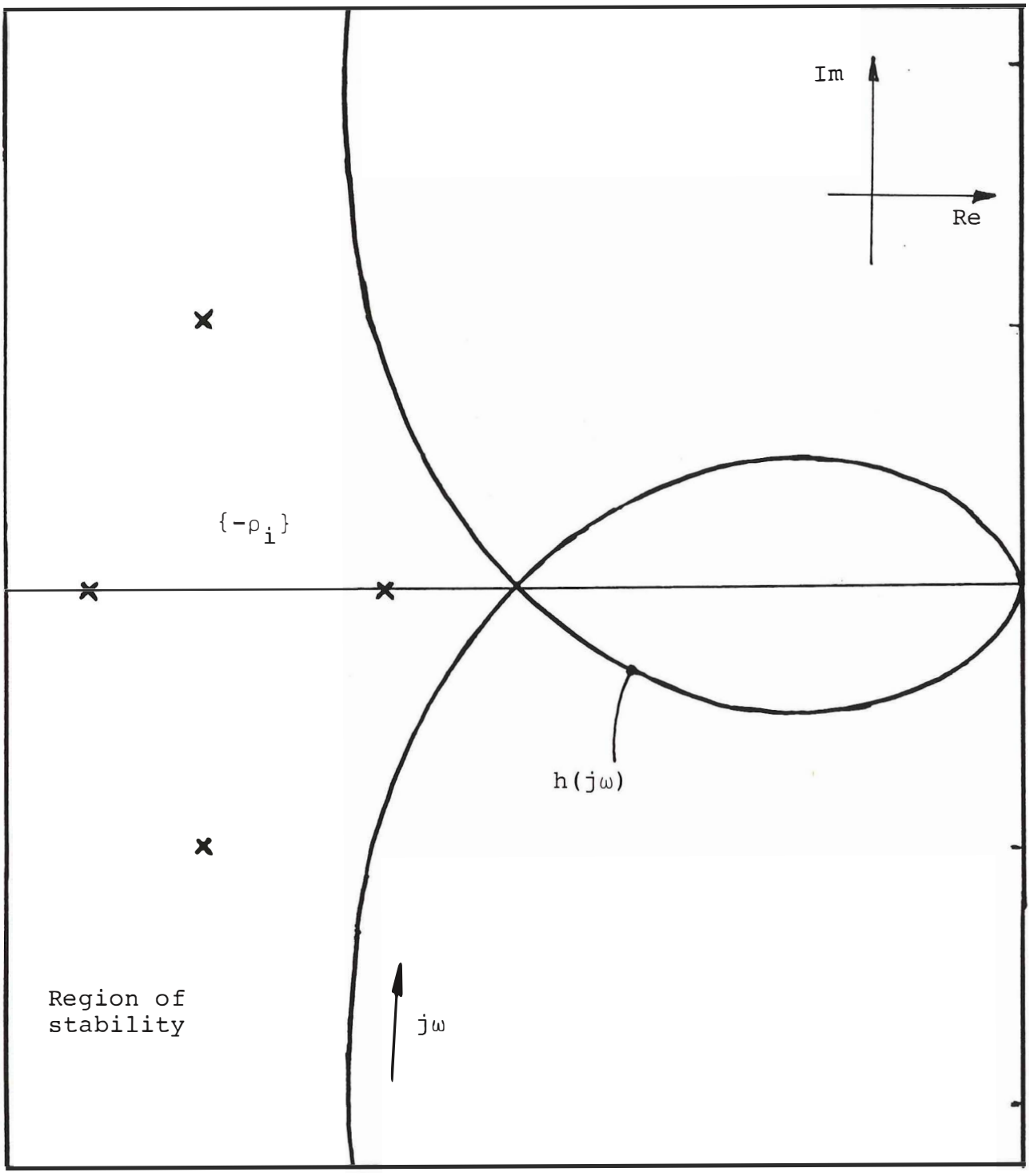

Figure 6.3. Graphical interpretation of the corollary in Section 6.2. The figure shows plots of $h(j\omega)$ and all $-\varrho_i$ in the left half of the complex plane. In the present case, stability is ensured since all $-\varrho_i$ are left of the curve traced out by $h(j\omega)$.

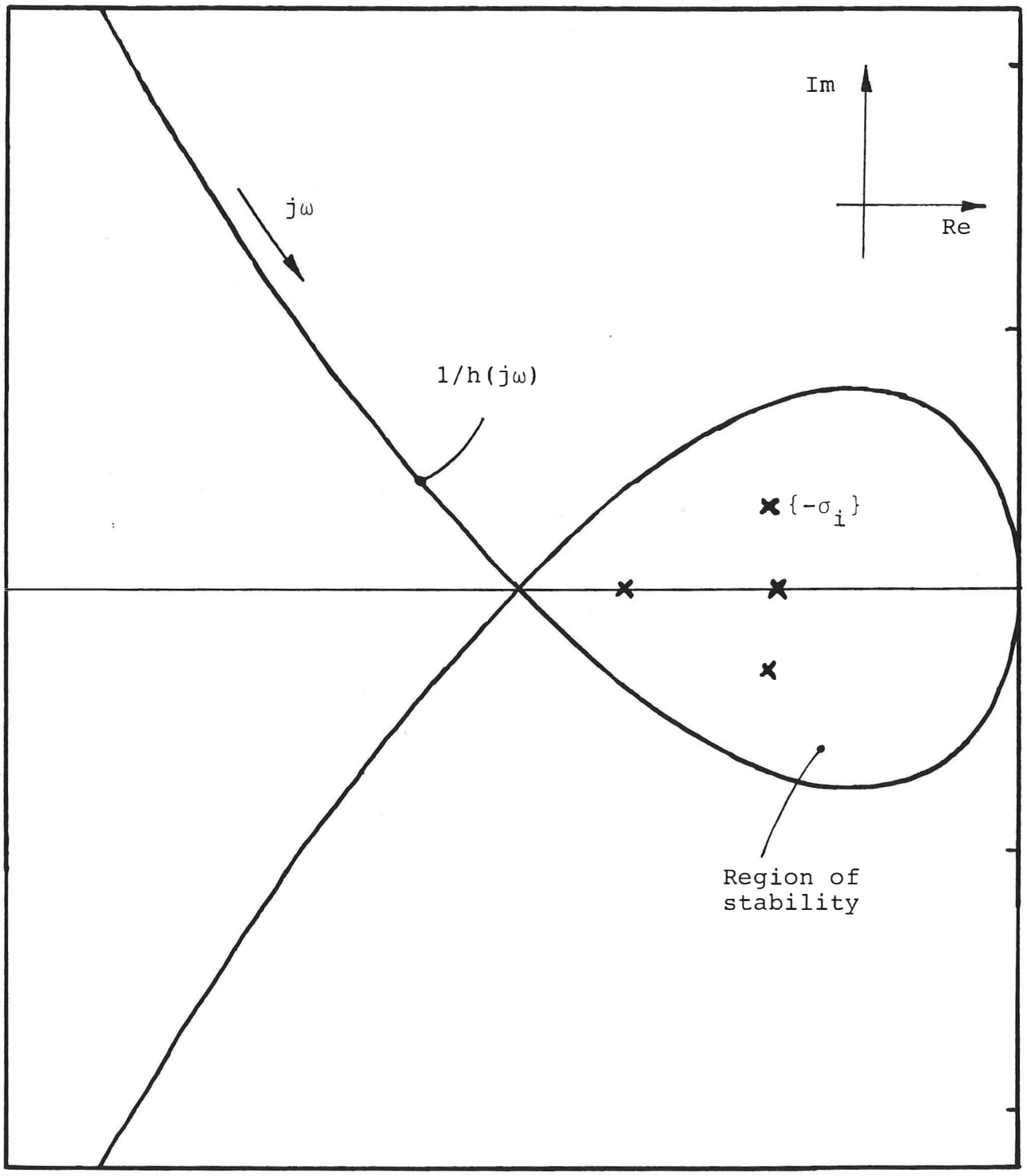

Figure 6.4. The reciprocal of the plot in Fig. 6.3. The system is stable since all eigenvalues of -S are within the indicated region of stability. The region can be considered as a narrowing of the left half plane, which would have been the region of stability if h(s) = 1/s.

$$L_1 = \frac{p_2^2 + p_4^2}{(a_1-a_2)^2} = [p_2,\ p_4](kI)\begin{bmatrix} p_2 \\ p_4 \end{bmatrix} \tag{6.28}$$

Transformed into servo coordinates, the index is written

$$L_1 = \underline{e}^T Q \underline{e} = \underline{e}^T J_{eM}^T J_{Mp}^T (kI) J_{Mp} J_{eM} \underline{e} \tag{6.29}$$

where by (3.2) and Fig. 6.2

$$J_{Mp} = \begin{bmatrix} 1 & b/2 \\ 1 & -b/2 \end{bmatrix} \quad ; \quad J_{eM} = \begin{bmatrix} a_3 + a_4 & a_4 \\ 1 & 1 \end{bmatrix} \tag{6.30}$$

For the computations, parameter values

$$k = 10 \cdot 10^3 \ m^{-2} \quad ; \quad b = 66 \cdot 10^{-3} \ m$$

$$a_3 = 1.6 \ m \quad ; \quad a_4 = 0.25 \ m$$

are taken, and it is assumed that the dynamics of the two servos may be represented by matrix A in (6.22), with parameters

$$2Z = I$$

$$\Omega = \omega_0 I \quad , \quad \omega_0 = 30 \ rad/s$$

This results in the process transfer matrix

$$H(s) = I\ h(s) \quad , \quad h(s) = \frac{1}{s[1 + \frac{s}{\omega_0} + (\frac{s}{\omega_0})^2]} \tag{6.31}$$

The system is to be controlled through the coordinating feedback matrix S, working in joint coordinates.

The scope is now to investigate how matrix S, as compared to the diagonal feedback described in Section 5.1, may alter the tracking performance. This will be visualized in terms of the two-by-two error transfer matrix

$$N(s) = \{\frac{e_i}{y_{j0}}\} \tag{6.32}$$

where e_1, e_2, y_{10} and y_{20} respectively denotes translational and orientational deviation and tool-marker motion. In matrix state-space notation, the controlled system becomes

$$\begin{aligned} \dot{\underline{x}} &= A\underline{x} + B\underline{y}_0 \\ \underline{e} &= D\underline{x} + E\underline{y}_0 \end{aligned} \tag{6.30}$$

where

$$A = \begin{bmatrix} 0 & 0 & -S \\ \Omega^2 & -\Omega & -\Omega^2 \\ 0 & 0 & 0 \end{bmatrix} ; \quad B = \begin{bmatrix} SJ_{eM}^{-1} \\ 0 \\ 0 \end{bmatrix}$$

$$D = [0 \quad 0 \quad -J_{eM}] ; \quad E = [\ I\ ]$$

and N(s) may be obtained by

$$N(s) = D(sI-A)^{-1}B + E \tag{6.34}$$

Rather than computing matrix S as described in Section 6.1, the feedback is established by heuristic minimization, c.f. (6.28), of the magnitude of the elements of

$$J_{Mp}N(s) = \{\frac{p_i}{y_{j0}}\} \tag{6.35}$$

subject to parameters c_0 and c_1 of

$$S = c_0\omega_0 \begin{bmatrix} 1 & 0 \\ \frac{c_1 a_4}{b} & 1 \end{bmatrix} \tag{6.36}$$

The reason for prescribing this specific feedback structure is, apart from the fact that it will give good results, that the

necessary and sufficient conditions for stability simply are

$$0 < c_0 < 1$$

This follows from the corollary obtained in Section 6.2 by noting that both critical points corresponding to matrix S are

$$-\sigma_i = -\frac{1}{c_0\omega_0}$$

and that no encirclements of these are made by h(s) as long as

$$-\infty < -\sigma_i < -\frac{1}{\omega_0}$$

The result of the heuristic minimization of (6.35) is

$$S_1 = \begin{bmatrix} 10 & 0 \\ 60 & 10 \end{bmatrix} \sec^{-1}; \quad c_0 = \frac{1}{3} \quad ; \quad c_1 = 1.6 \qquad (6.37)$$

To compare, application of the Ziegler-Nichols method as in Section 5.2 results in

$$S_0 = \begin{bmatrix} 15 & 0 \\ 0 & 15 \end{bmatrix} \sec^{-1}; \quad c_0 = \frac{1}{2} \quad ; \; c_1 = 0 \qquad (6.38)$$

Amplitude-frequency plots of (6.34) with S given by (6.37) and (6.38) are shown in Fig. 6.5. It is seen that the use of (6.37) rather than (6.38) can be considered to result in a trade-off between translational and rotational tracking performance. Considering the asymptotical behaviour of the plots at low frequencies, it is seen that for

$$S = S_0 : \quad \frac{e_1}{y_{10}}(s) = \frac{e_2}{y_{20}}(s) = s/15 \text{ sec}^{-1}$$

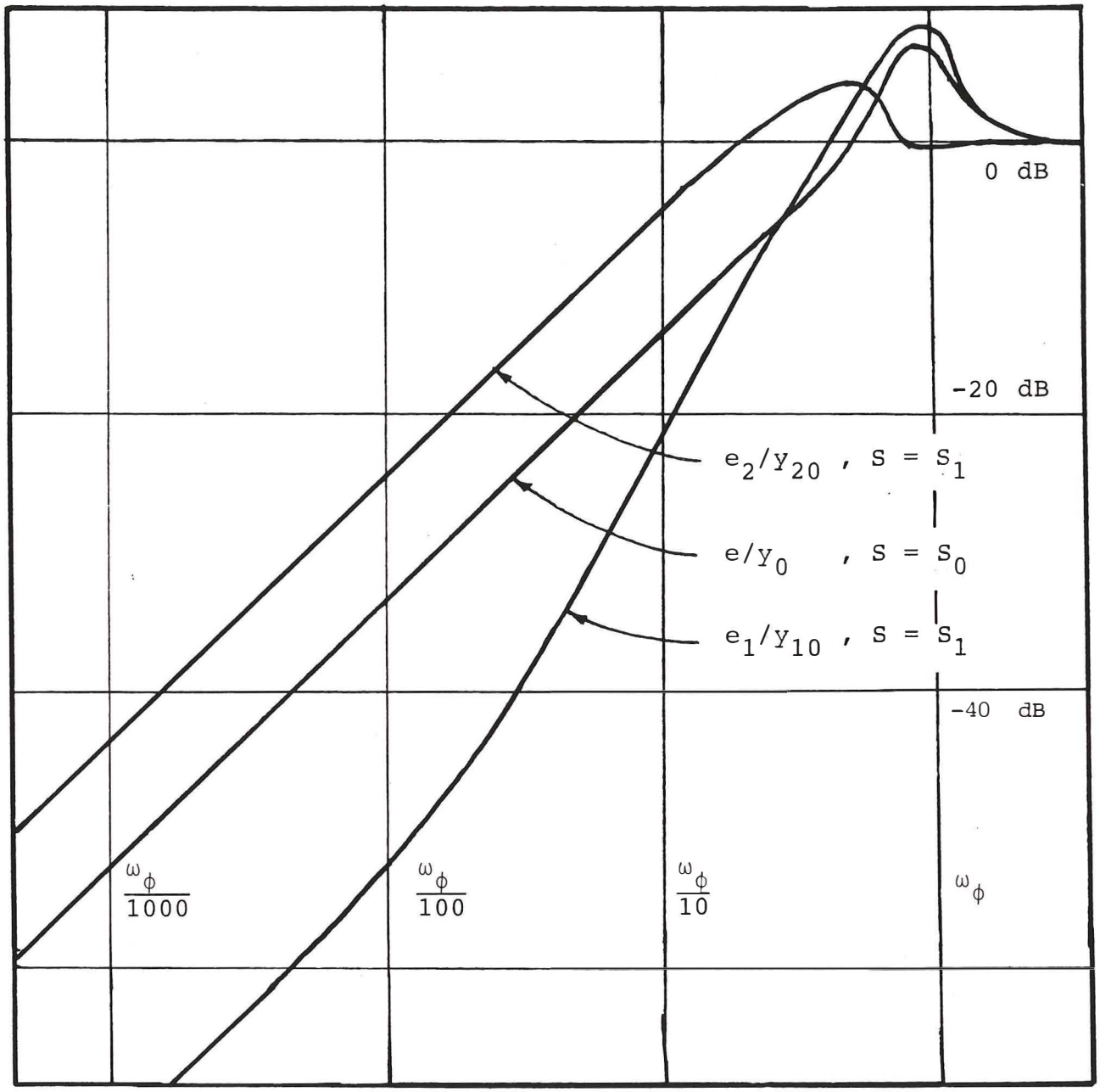

Figure 6.5. Amplitudes of the closed-loop transfer functions given by (6.37) and (6.38). It is seen that the use of S_1 implies better compensation of translational errors. The price to pay is a not-so-good compensation of rotational errors.

$$S = S_1 : \frac{e_1}{y_{10}}(s) = s/160\ \text{sec}^{-1};\ \frac{e_2}{y_{20}}(s) = s/5\ \text{sec}^{-1}$$

The design of the positional deviation sensor restricts the maximum translational and rotational deviation to

$$E_1 \approx 1\ \text{cm} \quad ; \quad E_2 \approx 0.3\ \text{rad}$$

which results in the maximum allowed steady-state velocities

$$S = S_0 : \ v_0 = 15\ \text{cm/s} \ ; \ w_0 = 4.5\ \text{rad/s}$$

$$S = S_1 : \ v_1 = 160\ \text{cm/s} \ ; \ w_1 = 1.5\ \text{rad/s}$$

Thus, feedback matrix S_1 results in a better performance distribution than is the case when applying matrix S_0.

In the given example, a non-zero displacement a_4 between the sensor and the manipulator wrist was assumed, which enables the wrist servo to assist in the compensation of translational deviation. The experimental systems described in Sections 5.3 and A4.1 do not however provide this displacement, so no attempt has been made to obtain practical results. Nevertheless, the principle of optimal coordination seems promising, and is believed to be of interest in connection with many applications in addition to direct teaching.

7. DYNAMIC MODEL OF THE MANIPULATOR

As Section 5.2 concluded, it is of major importance to increase the bandwidth of the servo controllers. The design of these will be based on the dynamic model developed in this section. Since the complete model of a hydraulically driven manipulator is extremely complicated, simplifications will be necessary. Based on the qualitative results from the preliminary experiments, each hydraulic actuator is treated separately, except for actuators 2 and 3 for which coupling will be considered. The structural elasticity of manipulator link 3 is believed to be significant and is included in the model. For simplicity, only the subsystem consisting of servos 2 and 3 will be considered. The resulting model may easily be modified to fit the other subsystems.

7.1. Equations of motion

The structure to be considered is shown in Fig. 7.1. This is a two-link system where the outer link is nonrigid. Considering only one elastic mode, a 3 d.o.f. structure results. The generalized coordinates to be used are:

q_1: joint 2 displacement

q_2: angular displacement of a neutral axis which will be defined in (7.6).

q_3: joint 3 displacement relative to q_2

This means that joint 3 displacement is found by adding q_2 and q_3. The deflection of link 3 is defined by function $u(r,q_3)$ such that

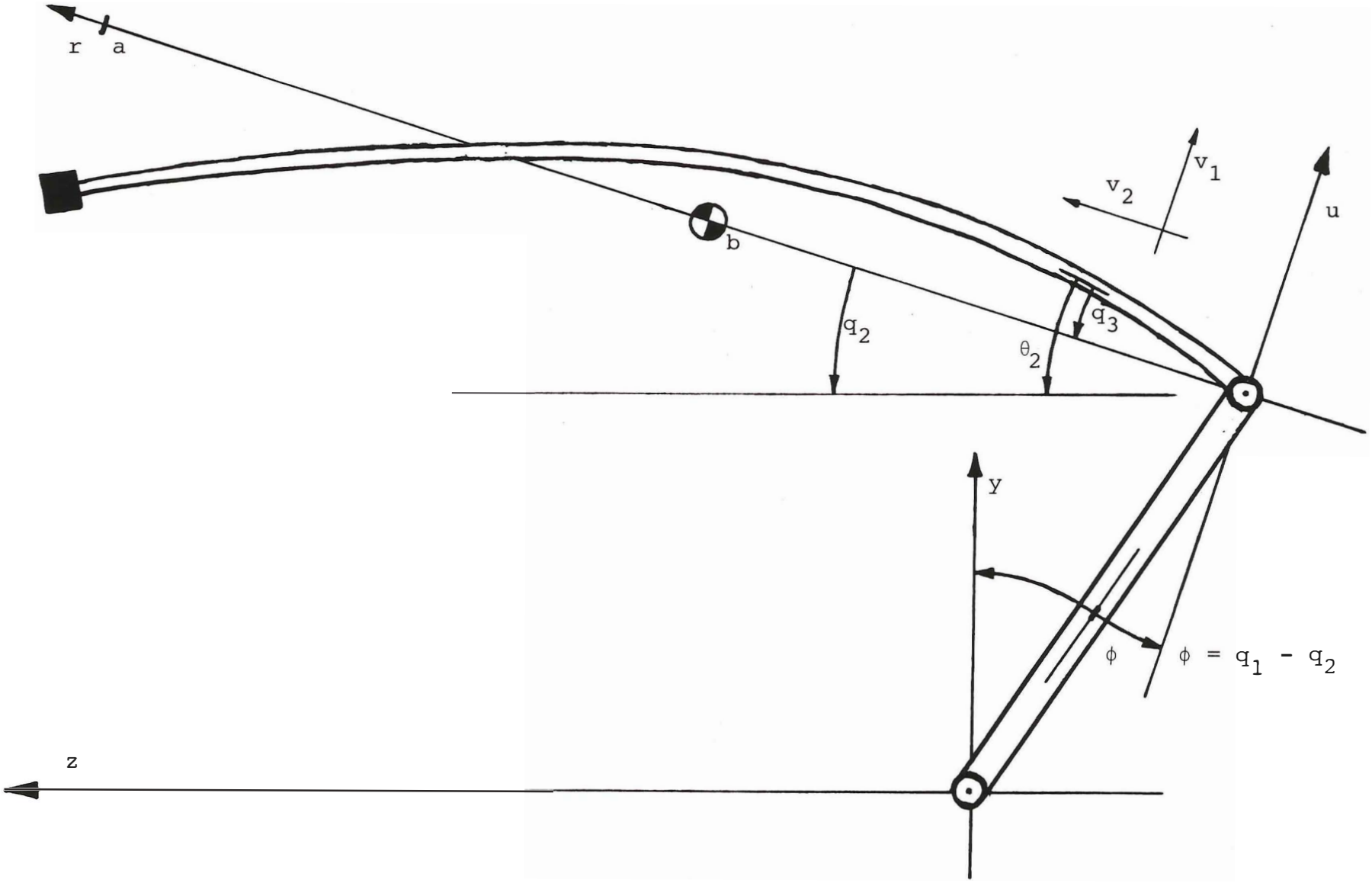

Figure 7.1. Structure and notation for two-link two-joint elastic manipulator.

$$u(r,q_3) = -q_3\beta(r) \tag{7.1}$$

The Lagrange equations (Meriam, 1975) for this system will now be developed.

The velocity at every point on link 3 is given by

$$v_1(r) = -\dot{q}_1\, a_2\sin\varphi - \dot{q}_2 r - \dot{q}_3\beta(r)$$

$$v_2(r) = \dot{q}_1\, a_2\cos\varphi$$

where v_1 and v_2 respectively denote velocity perpendicular to and along the r-axis defined in Fig. 7.1. From this, speed magnitude squared becomes

$$\begin{aligned} |\underline{v}(r)|^2 = v_1^{\,2} + v_2^{\,2} &= a_2^2\,\dot{q}_1^2 + 2a_2 r\sin\varphi\ \dot{q}_1\dot{q}_2 \\ &+ 2a_2\beta(r)\sin\varphi\ \dot{q}_1\dot{q}_3 \\ &+ r^2\dot{q}_2^2 + 2r\,\beta(r)\dot{q}_2\dot{q}_3 + \beta^2(r)\dot{q}_3^2 \end{aligned} \tag{7.3}$$

Assuming link 3 mass m_3, with distribution

$$\mu(r) = m_3 i(r) \quad ; \quad \int_0^{a_3} i(r)dr = 1 \tag{7.4}$$

the kinetic energy of the link is

$$T_3 = \frac{1}{2}\, m_3 \int_0^{a_3} i(r)|\underline{v}(r)|^2 dr \tag{7.5}$$

By defining coordinate q_2 such that

$$\int_0^{a_3} i(r)r\,\beta(r)dr = 0 \tag{7.6}$$

this may be written

$$T_3 = \frac{1}{2} m_3(a_2^2\dot{q}_1^2 + 2a_2 b \sin\varphi\ \dot{q}_1\dot{q}_2$$

$$+ 2a_2 D \sin\varphi\ \dot{q}_1\dot{q}_3 + R^2\dot{q}_2^2 + B^2\dot{q}_3^2) \qquad (7.7)$$

where

$$b = \int_0^{a_3} i(r)r\,dr \quad ; \quad D = \int_0^{a_3} i(r)\beta(r)dr$$

$$R^2 = \int_0^{a_3} i(r)r^2dr \quad ; \quad B^2 = \int_0^{a_3} i(r)\beta^2(r)dr$$

The kinetic energy of link 2 is simply

$$T_2 = \frac{1}{2} J_1' \dot{q}_1^2 \qquad (7.8)$$

where J_1' is its moment of inertia about the axis of joint 2. The total kinetic energy is $T = T_2 + T_3$.

Neglecting gravitational effects, the potential energy of the system is given by link 3 deflection only. Considering the link as a slender beam, it may be written

$$V = \frac{1}{2} \int_0^{a_3} \varkappa(r)\left(\frac{\partial^2 u}{\partial r^2}\right)^2 dr = \frac{1}{2} k_s q_3^2 \qquad (7.9)$$

where $\varkappa(r)$ and k_s denote distributed and total bending stiffness. By (7.1) and (7.9),

$$k_s = \int_0^{a_3} \varkappa(r)\left(\frac{\partial^2 \beta}{\partial r^2}\right)^2 dr$$

For each generalized coordinate in the system, the Lagrange equation has the form

$$\tau_i' = \frac{\partial}{\partial t}\left(\frac{\partial T}{\partial \dot{q}_i}\right) + \frac{\partial V}{\partial q_i} \tag{7.10}$$

where τ_i' is the generalized force corresponding to q_i. By Fig. 7.1, both τ_2' and τ_3' denote the torque in joint 3, so a new vector $\underset{\sim}{\tau} = [\tau_1, \tau_2, \tau_3]^T$ is introduced where

$$\tau_i = \tau_i' - \partial V/\partial q_i \tag{7.11}$$

which by (7.9) gives

$$\tau_1 = \tau_1' \quad ; \quad \tau_2 = \tau_2' = \tau_3'$$

$$\tau_3 = \tau_2 - k_s q_3 \tag{7.12}$$

Applying this, (7.7), (7.8) and (7.10),

$$\begin{aligned}
\tau_1 &= (m_3 a_2^2 + J_2')\ddot{q}_1 + m_3 a_2 b\sin\varphi\ \ddot{q}_2 + m_3 a_2 D\sin\varphi\ \ddot{q}_3 \\
\tau_2 &= m_3 a_2 b\sin\varphi\ \ddot{q}_1 + m_3 R^2 \ddot{q}_2 \\
\tau_3 &= m_3 a_2 D\sin\varphi\ \ddot{q}_1 + m_3 B^2 \ddot{q}_3
\end{aligned} \tag{7.13}$$

which together with (7.12) constitute the equations of motion. Note that Coriolis and sentrifugal terms are omitted by assuming $\dot{\varphi} \approx 0$. Matrix notation for (7.13) is

$$\underset{\sim}{\tau} = M(\varphi)\ddot{\underline{q}} \tag{7.14}$$

where, by defining

$$\begin{aligned}
&J_1 = (m_3 a_2^2 + J_1') \quad ; \quad J_2 = m_3 R^2 \quad ; \quad J_3 = m_2 B^2 \\
&J_{12} = m_2 a_1 b \quad ; \quad J_{13} = m_2 a_1 D
\end{aligned} \tag{7.15}$$

the inertia matrix may be written

$$M(\varphi) = \begin{bmatrix} J_1 & J_{12}\sin\varphi & J_{13}\sin\varphi \\ J_{12}\sin\varphi & J_2 & 0 \\ J_{13}\sin\varphi & 0 & J_3 \end{bmatrix} \tag{7.16}$$

In general, the corresponding inverse equation will be

$$\ddot{\underline{q}} = N(\varphi)\,\underline{\tilde{\tau}} \tag{7.17}$$

where

$$N(\varphi) = \begin{bmatrix} n_1 & n_{12} & n_{13} \\ n_{12} & n_2 & n_{23} \\ n_{13} & n_{23} & n_3 \end{bmatrix} = M^{-1}(\varphi) \tag{7.18}$$

Considering (7.12), a fourth order state space model

$$\dot{\underline{x}} = A(\varphi)\underline{x} + B(\varphi)\underline{\tau} \tag{7.19}$$

is obtained, where

$$\underline{x} = [\dot{q}_1 \quad \dot{q}_2 \quad \dot{q}_3 \quad q_3]^T \;\; ; \;\; \underline{\tau} = [\tau_1 \quad \tau_2]^T$$

$$A = \begin{bmatrix} 0 & 0 & 0 & -n_{13}k_s \\ 0 & 0 & 0 & -n_{23}k_s \\ 0 & 0 & 0 & -n_3k_s \\ 0 & 0 & 1 & 0 \end{bmatrix}; \; B = \begin{bmatrix} n_1 & n_{12} + n_{13} \\ n_{12} & n_2 + n_{23} \\ n_{13} & n_{23} + n_3 \\ 0 & 0 \end{bmatrix} \tag{7.20}$$

When $\varphi = 0$, the coupling terms n_{12}, n_{13} and n_{23} vanish since $M(0)$ is diagonal. In this case the control of link 3 may be considered separately. From the calculations of stiffness and inertia terms made in Appendix A2, it is found that the pinned-free frequency of link 3,

$$\omega_{pf}(0) = (n_3(0)k_s)^{1/2} = \left(\frac{k_s}{J_3}\right)^{1/2} \tag{7.21}$$

exceeds the clamped-free frequency

$$\omega_{cf} = \left(\frac{k_s}{J_2}\right)^{1/2} \tag{7.22}$$

by a factor of 10 approx. Inspired by this, an attempt will be made to simplify (7.19) and (7.20) by reducing the order of the system. This may be done by a singular perturbation method (Kokotovic, 1976). In the present case, this is simple since only the dynamic equation for $\dot{q}_3$ needs to be considered. By (7.19) and (7.20) with (7.21) inserted,

$$\dot{q}_3 = -\omega_{pf}^2 q_3 + n_{13}\tau_1 + (n_{23} + n_3)\tau_2 \tag{7.23}$$

From the corresponding static equation ($q_3 = 0$), a static expression for q_3 is found.

$$q_3 = \frac{n_{13}}{\omega_{pf}^2}\tau_1 + \frac{n_{23} + n_3}{\omega_{pf}^2}\tau_2 \tag{7.24}$$

This may be inserted into the dynamic equations for $\dot{q}_1$ and $\dot{q}_2$, leaving

$$\begin{bmatrix} \dot{q}_1 \\ \dot{q}_2 \end{bmatrix} = \begin{bmatrix} \left(n_1 - \frac{n_{13}^2}{n_3}\right) & \left(n_{12} + n_{13} - \frac{n_{13}(n_{23} + n_3)}{n_3}\right) \\ \left(n_{12} - \frac{n_{13}n_{23}}{n_3}\right) & \left(n_2 + n_{23} - \frac{n_{23}(n_{23} + n_3)}{n_3}\right) \end{bmatrix} \underline{\tau} \tag{7.25}$$

and the static equation

$$q_3 = \frac{1}{k_s}\left[\frac{n_{13}}{n_3} \quad \frac{n_{23} + n_3}{n_3}\right] \underline{\tau} \tag{7.26}$$

These may be simplified further by noting the order of magnitude of each element in $N(\varphi)$. By assuming

$$n_3 >> n_{23} \quad \text{and} \quad n_3 >> n_{13} \tag{7.27}$$

which follows from the discussion in Appendix A2, (7.25) and (7.26) may be approximated by

$$\begin{bmatrix} \ddot{q}_1 \\ \ddot{q}_2 \end{bmatrix} = \begin{bmatrix} n_1 & n_{12} \\ n_{12} & n_2 \end{bmatrix} \underline{\tau} \tag{7.28}$$

$$q_3 = [0 \quad \frac{1}{k_s}] \underline{\tau} \tag{7.29}$$

By the same results, this 2x2 N-matrix may be approximated by inverting the upper left 2x2 block of $M(\varphi)$ in (7.16).

This simple model closely resembles what would have been obtained if link 3 in Fig. 7.1 had been considered rigid. The main difference lies in the presence of (7.29), which will influence both the dynamics of the corresponding hydraulic servo and the measurements. Hence its influence on the dynamics of the control system is significant.

7.2. Actuators

The arrangement for driving either joint 2 or 3 of the TR 400 is outlined in Fig. 7.2. It consists of a linear hydraulic cylinder controlled by a 4-way spool valve. Motion is transfered to the corresponding joint through a simple lever and, for joint 3, a parallelogram structure. The joint displacement sensor measures the lever angle θ.

In Appendix A3 a first order linear dynamic model is developed. This takes into account leakage, and deflection of the hydraulic fluid. The dynamics and the nonlinear load dependence of the servo valve is not included however. Summing up, the actuator model may be linearized about a workpoint θ_0 and written

$$\dot{\tau} = -k_t(\theta_0)\tau - k_h(\theta_0)\theta + k_u(\theta_0)u \tag{7.30}$$

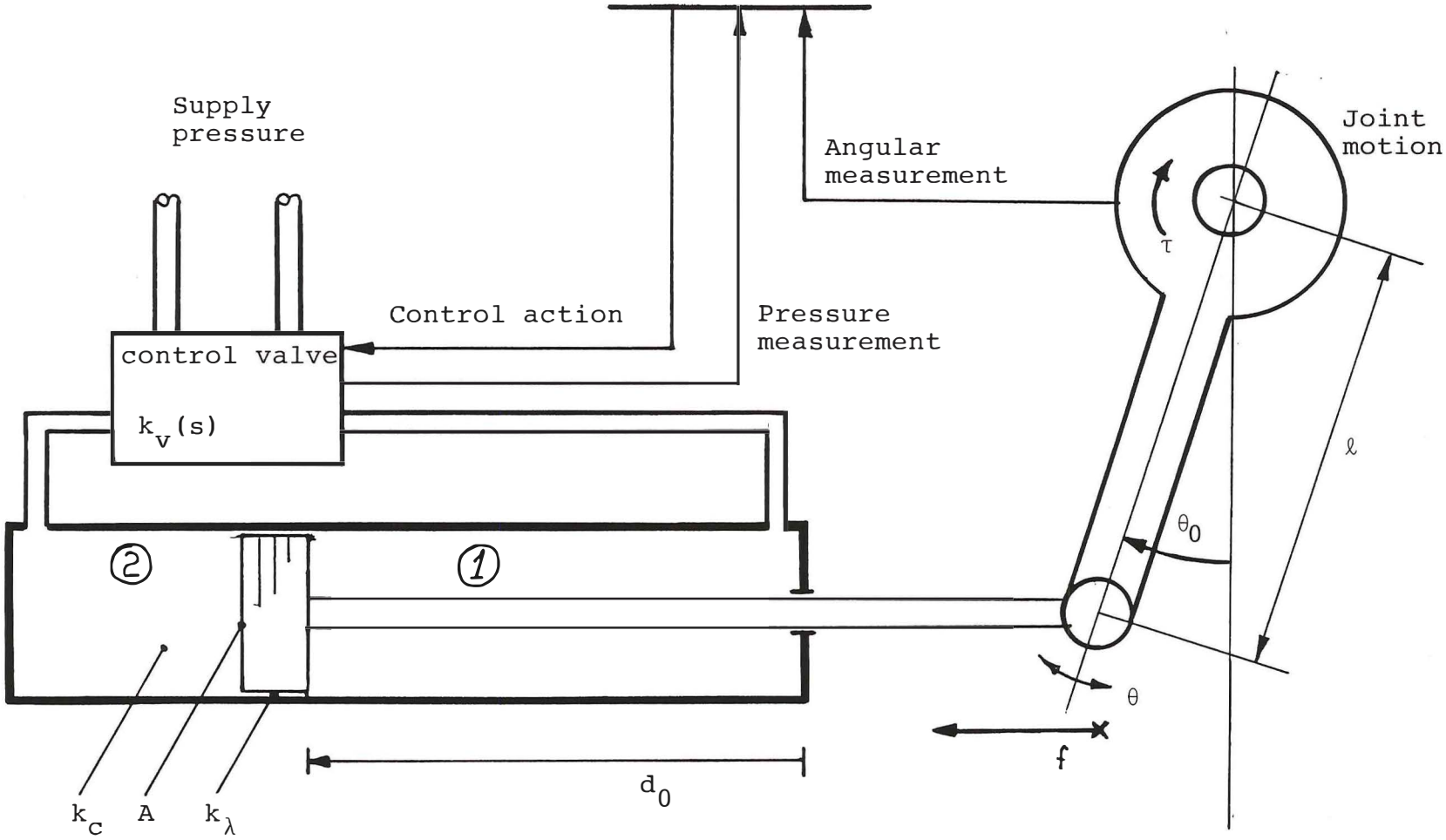

Figure 7.2. Translational hydraulic actuator. The motion is transferred to the manipulator joint through a lever.

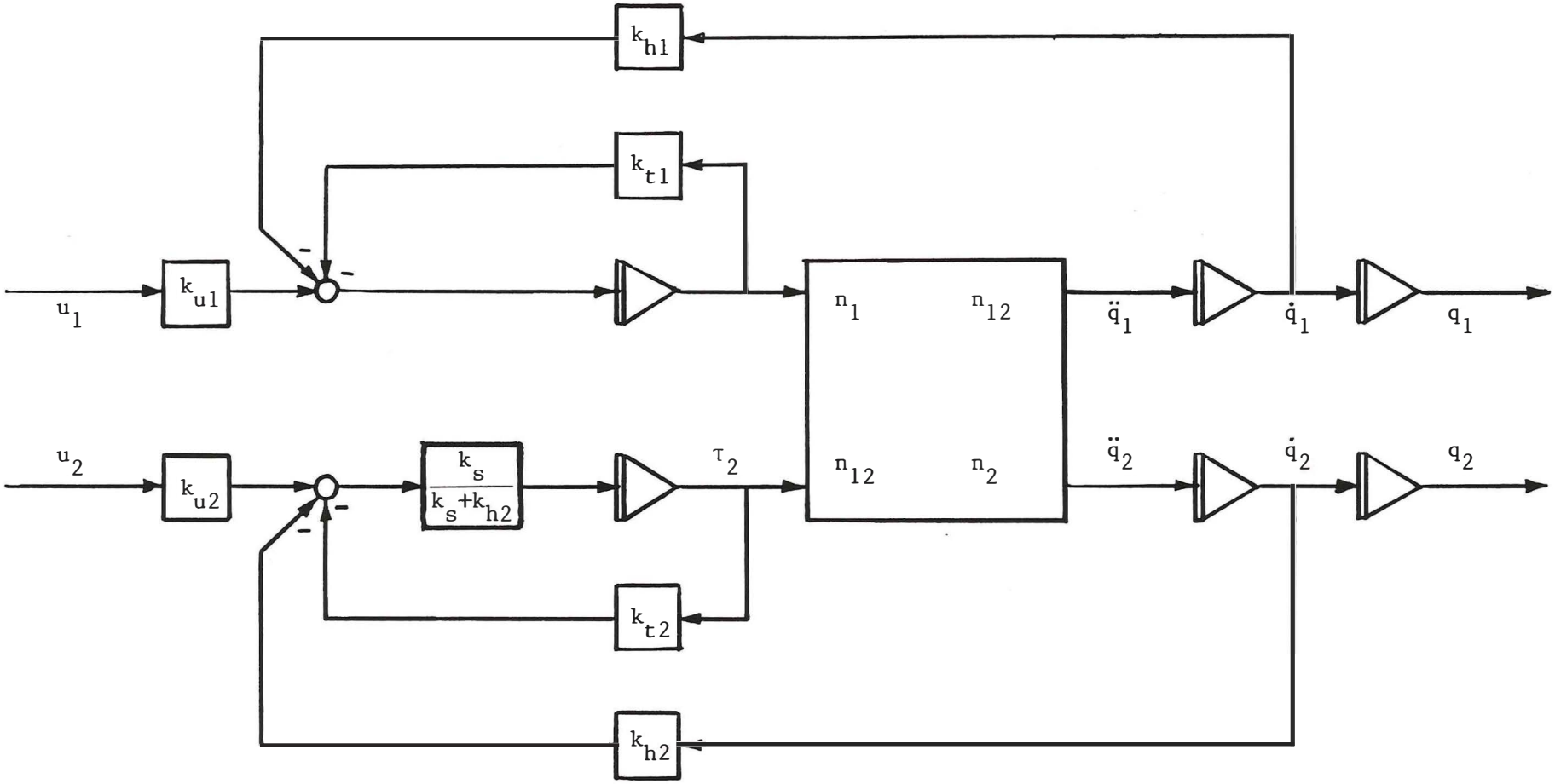

Figure 7.3. Complete dynamic model for the two-link two-joint manipulator. Measurements omitted.

Here u, τ and θ respectively denote control action, joint torque and joint displacement perturbation. As pointed out in Appendix A3, the coefficients are difficult to determine exactly. Because of this, special care must be taken during the design of the control system.

Sticking to the notation of Section 7.1, (7.30) for joint 2 becomes

$$\dot{\tau}_1 = -k_{t1}\tau_1 - k_{h1}\dot{q}_1 + k_{u1}u_1 \tag{7.31}$$

and for joint 3

$$\dot{\tau}_2 = -k_{t2}\tau_2 - k_{h2}(\dot{q}_2 + \dot{q}_3) + k_{u2}u_2 \tag{7.32}$$

Inserting the time derivative of (7.29) and rearranging,

$$\dot{\tau}_2 = -k_{st2}\tau_2 - k_{sh2}\dot{q}_2 + k_{su2}u_2 \tag{7.33}$$

where

$$k_{st2} = \frac{k_s k_{t2}}{k_s + k_{h2}} \quad ; \quad k_{sh2} = \frac{k_s k_{h2}}{k_s + k_{h2}}$$

$$k_{su2} = \frac{k_s k_{u2}}{k_s + k_{h2}} \tag{7.34}$$

Eqs. (7.31) and (7.33) may again be inserted into (7.28), the result being the 6-state linearized dynamic model shown in Fig. 7.3. This will be used in the investigation of controllers made in Section 8.

7.3. Measurements

The complete system includes several measurements. In addition to the positional deviation sensor located at the tip of the manipulator, joint displacements and torques may be measured. Available in the second experimental system, Section 5.4, are

- Hydraulic pressure, servos 1, 2 and 3
- Joint displacement, all 5 servos
- 5-measurements positional deviation sensor

The 2 d.o.f. subsystem discussed so far influences

- Hydraulic pressure, servos 2 and 3
- Joint displacement, servos 2 and 3
- 2 translational and 1 rotational deviation measurement.

By (A3.9) and (A3.14) in Appendix A3, pressure difference results from torque by

$$p_1 = \frac{f_1}{A} = \frac{1}{A a \cos q_1}\,\tau_1 \tag{7.35}$$

$$p_2 = \frac{f_2}{A} = \frac{1}{A a \cos q_2}\,\tau_2 \tag{7.36}$$

Accordingly, joint torque estimates are

$$\begin{aligned} \hat{\tau}_1 &= p_1\, A a \cos q_1 \\ \hat{\tau}_2 &= p_2\, A a \cos q_2 \end{aligned} \tag{7.37}$$

Assuming for the moment that these computations are part of the process, measurements

$$\hat{\tau} = \tau_1 \quad ; \quad \hat{\tau}_2 = \tau_2 \tag{7.38}$$

are obtained. Figure 7.1 relates joint displacements to the generalized coordinates by

$$\theta_2 = q_1 \tag{7.39}$$

$$\theta_3 = q_2 + q_3 = q_2 + \frac{1}{k_s}\,\tau_2 \tag{7.40}$$

The positional measurements at the tip of the manipulator are found by considering a part of the manipulator Jacobian. It is assumed that the current position of the tool marker corresponds to the generalized coordinate values q_{10} and q_{20}. Then, $\Delta q_1 = q_1 - q_{10}$ and $\Delta q_2 = q_2 - q_{20}$ denote perturbations of the manipulator around these values. Affected deviational quantities in Cartesian coordinate system 3, cf. Section A1.3, are ${}^3d_2$, ${}^3d_3$ and ${}^3\delta_1$. For small perturbations,

$$ {}^3d_2 = a_2 \sin\varphi \, \Delta q_1 + a_3 \Delta q_2 + \frac{\beta(a_3)}{k_s} \tau_2 \tag{7.41} $$

$$ {}^3d_3 = -a_2 \cos\varphi \, \Delta q_1 \tag{7.42} $$

$$ {}^3\delta_1 = -\Delta q_2 - \frac{\beta'(a_3)}{k_s} \tau_2 \tag{7.43} $$

approximate the measurement functions. Here $\varphi = q_1 - q_2$, function $\beta(r)$ is defined in (7.1) and

$$ \beta'(a_3) = \frac{\partial \beta}{\partial r}(a_3) \tag{7.44} $$

As seen, (7.29) was applied in (7.41) and (7.43),so the elasticity of link 3 enters here as well. For the TR 400 manipulator, cf. Section A2.2,

$$ \beta(a_3) \approx 0 \tag{7.45} $$

This is due to the choice of generalized coordinates and the link 3 mass distribution of the manipulator at hand. In this case,

$$ {}^3d_2 = a_2 \sin\varphi \, \Delta q_1 + a_3 \Delta q_2 \tag{7.46} $$

$$ {}^3d_3 = -a_2 \cos\varphi \, \Delta q_1 \tag{7.47} $$

$$ {}^3\delta_1 = -\Delta q_2 - k_r \tau_2 \tag{7.48} $$

Of these, the first two equations will enter in the infimal control system for servos 2 and 3. The last equation represents

coupling which will be passed on to the orientational servos if not nulled out by the coordination scheme.

Application of (A1.5) in Appendix A1 with $v_2 = {}^3d_2$, $v_3 = {}^3d_3$, $e_2 = \Delta\vartheta_2$ and $e_3 = \Delta\vartheta_3$ results in the control error estimates

$$e_2 = -\Delta q_1 \quad ; \quad e_3 = -\Delta q_2 \tag{7.49}$$

in joint coordinates. This one-to-one correspondence between error estimates and generalized coordinates is very convenient, since in that case no special means are required to compensate for structural elasticities. However, since (7.45) is an approximation only, a slight coupling from τ_2 must be expected.

8. INFIMAL CONTROL

In Section 5.2, simple expressions were developed which relate tracking performance and process bandwidth. Assumed controllers were of the P and the PI type, subject to a process with internal speed control. What remains is to investigate how different infimal (internal) controllers affect the performance. Below, this is done theoretically in terms of pole-zero-placements and, to some extent, experimentally.

8.1. A first approach

Based on the model developed in Section 7, a simple way to obtain approximate, internal speed control is by non-feedback input scaling. Inserting $\dot{t} = 0$ and $\tau = 0$ in (7.30) results in the static relationship

$$u = \frac{k_h(e_0)}{k_u(e_0)} \dot{e} \tag{8.1}$$

which may be modified to form the constant, non-feedback controller

$$u = (k_h(0)/k_u(0))\dot{e}_{ref} \tag{8.2}$$

Combination of (8.1) and (8.2) will result in $\dot{e} \approx \dot{e}_{ref}$ whenever $e \approx 0$ and (8.1) holds, i.e. for low frequencies. Ratio $\dot{e}/\dot{e}_{ref}$ increases slightly for nonzero e_0. This effect is of little significance however.

As in Section 5.2, supremal positional controllers are tuned using the Ziegler-Nichols method, the first step of which is to apply a proportional (P) controller and adjust its gains until the

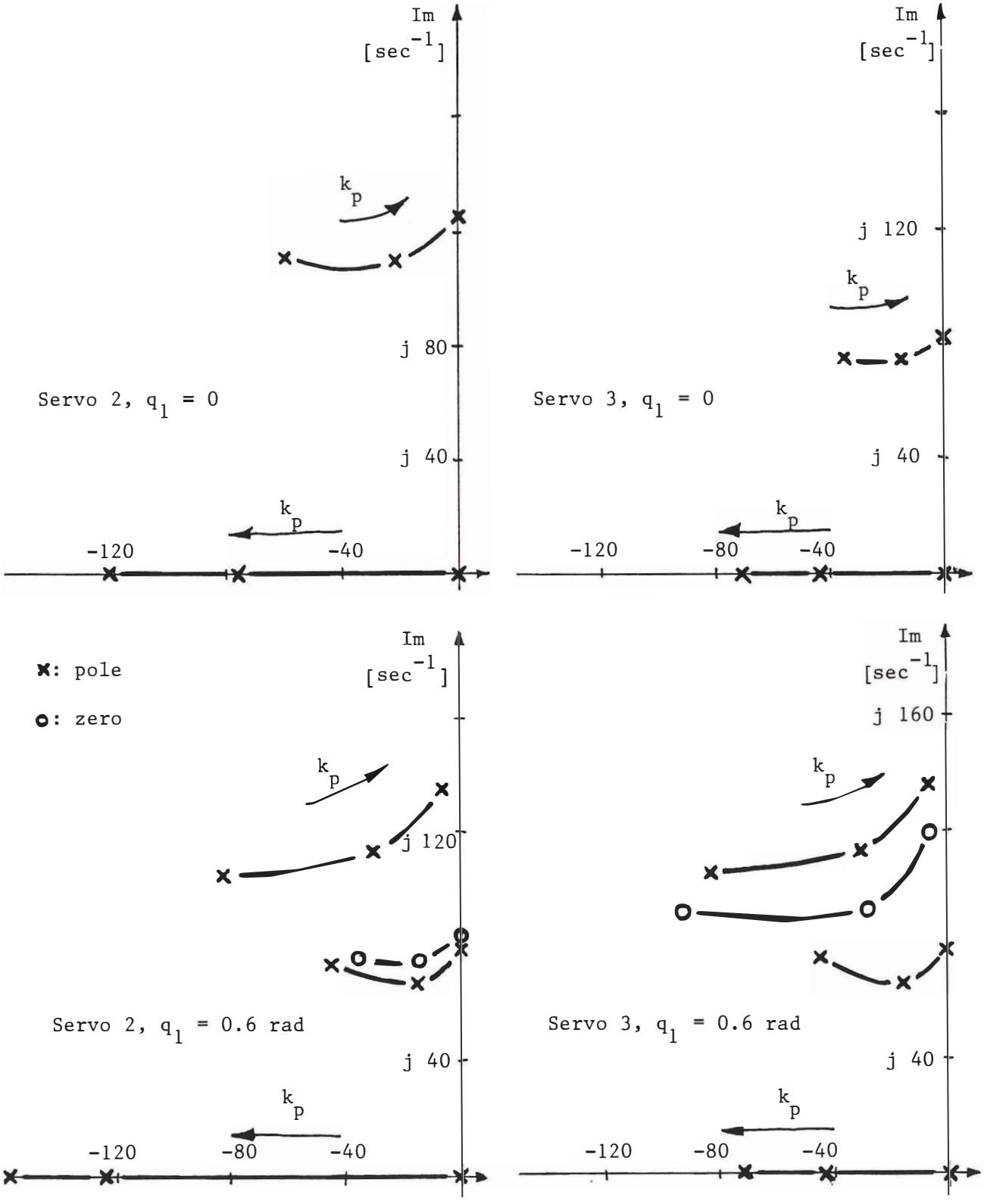

Figure 8.1. Plots of the left half of the complex plane showing pole-zero placements for P-type servos. Internal speed control is given by (8.2). Arrows indicate pole-zero motion when increasing k_p.

stability limit is reached. The vector of critical gains is denoted by $\underline{\omega}_x$ whereas $\underline{\omega}_\varphi$ denotes the frequencies of the obtained oscillating behaviour. In the present case, these are found to be

$$\underline{\omega}_x = \begin{bmatrix} 121 \\ 78 \end{bmatrix} s^{-1} \quad ; \quad \underline{\omega}_\varphi = \begin{bmatrix} 127 \\ 87 \end{bmatrix} s^{-1}$$

Controllers are now designed using (5.9) and (5.19). The plots in Fig. 8.1 show the locations of poles and zeros of the closed loop transfer functions

$$h_{11}(s) = q_1(s)/q_{10}(s)$$

$$h_{22}(s) = q_2(s)/q_{20}(s)$$

under positional P-type control. Plots are given for the three proportional gain combinations

$$\underline{k}_p = \underline{\omega}_x \quad ; \quad \underline{k}_p = 0.5\ \underline{\omega}_x \quad ; \quad \underline{k}_p = \underline{0}$$

subject to the two configurations

$$\underline{q} = \begin{bmatrix} 0 \\ 0 \end{bmatrix} \quad \text{and} \quad \underline{q} = \begin{bmatrix} 0.6 \\ 0 \end{bmatrix} \text{ rad}$$

As seen, the bandwidth of each servo is firmly restricted by $\underline{\omega}_\varphi$. It is also seen that the system is robust with respect to changes in the manipulator configuration. Fig. 8.2 shows the pole-zero placement of the same process under Ziegler-Nichols PI-control. The system is still robust even though the coupling between the two servos seems more noteable.

Application of (5.17) and (5.20) with E = 1 cm inserted, results in the performance measures

$$\underline{v}_P = 0.5\ E\ \underline{\omega}_x = \begin{bmatrix} 0.60 \\ 0.39 \end{bmatrix} \text{ m/s}$$

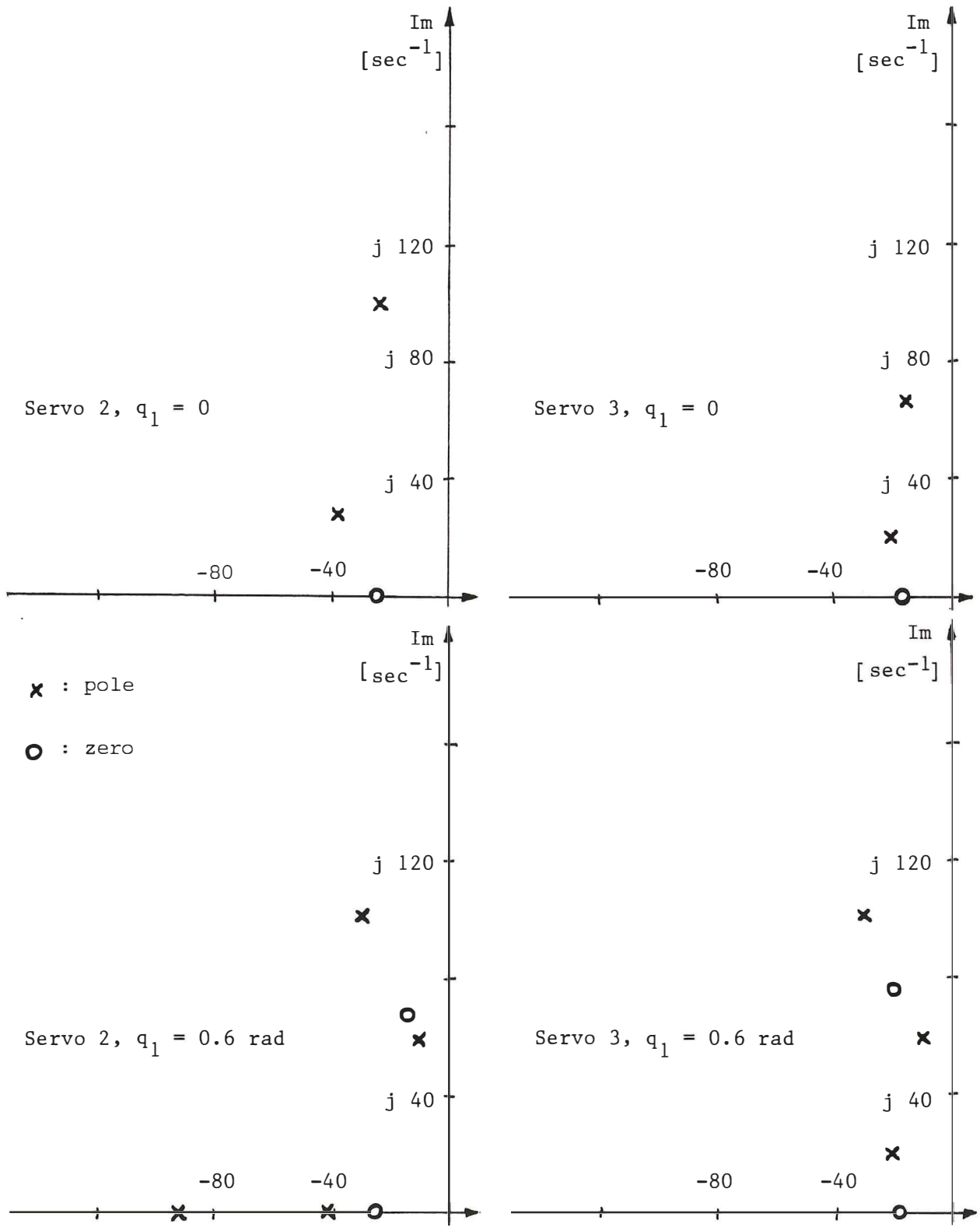

Figure 8.2. Corresponding plots for PI-type servos. Controller parameters are $k_p = 0.45\ \omega_x$; $T_i = 5/\omega_\varphi$.

$$\underline{a}_{pI} = 0.09\ E \begin{bmatrix} \omega_{x1}\omega_{\varphi 1} \\ \omega_{x2}\omega_{\varphi 2} \end{bmatrix} = \begin{bmatrix} 13.8 \\ 6.1 \end{bmatrix} \text{ m/s}^2 \qquad (8.3)$$

respectively for proportional and proportional plus integral control. The exactness of these numbers, and of the presented plots, rely on the exactness of the several, and sometimes diffuse, constants computed in Appendices A2 and A3. In fact, compared to the experimental results, they are too good to be true. This is not so important however, since the scope at the moment is to show that the obtained performance may still be improved.

8.2. Internal feedback

The bandwidth of the infimal speed controller can be increased by introducing feedback from torque and angular velocity. These quantities may be obtained either by measurements or by state estimation. The controller can take the form

$$\underline{u} = -G_\tau \underline{\tau} + G_v(\dot{\underline{q}}_0 - \dot{\underline{q}}) \qquad (8.4)$$

The bandwidth is more than tripled by applying the values

$$G_\tau = \begin{bmatrix} 352 & 0 \\ 0 & 634 \end{bmatrix} 10^{-6}/\text{Nm} \approx \frac{k_t(0)}{k_u(0)} \begin{bmatrix} 2 & 0 \\ 0 & 3.6 \end{bmatrix}$$

$$G_v = \begin{bmatrix} 5.1 & 0 \\ 0 & 10.2 \end{bmatrix} \text{s} \approx \frac{k_h(0)}{k_u(0)} \begin{bmatrix} 10 & 0 \\ 0 & 20 \end{bmatrix} \qquad (8.5)$$

and may be extended further if so desired. In the same way as in Section 8.1, a supremal positional controller is applied as well, and the resulting poles and zeros are plotted in Figs. 8.3 and 8.4. The new values for $\underline{\omega}_x$ and $\underline{\omega}_\varphi$ are found to be

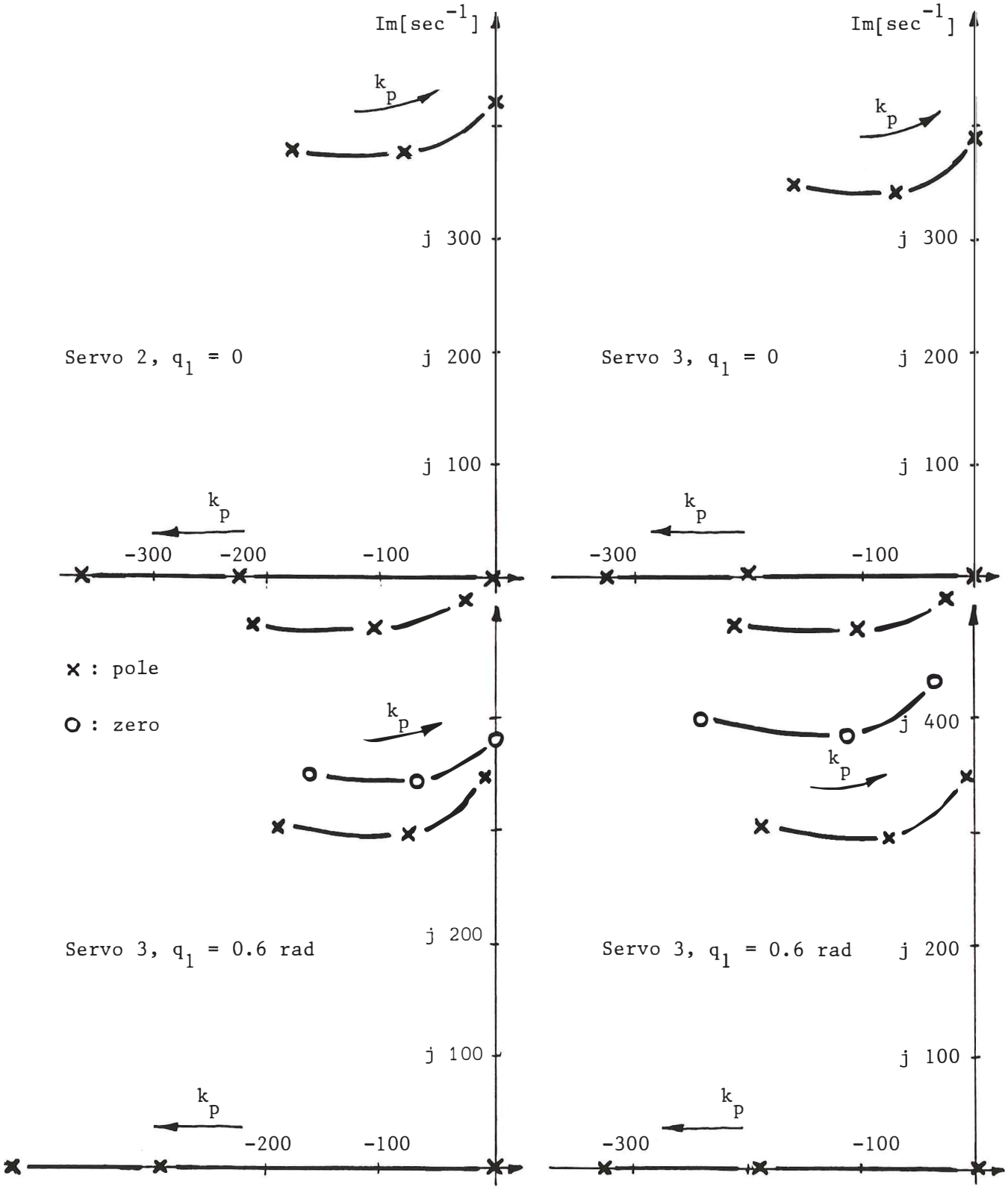

Figure 8.3. Plots showing pole-zero placements for P-type servos where the internal speed control is given by (8.5). Note that the scale differs from the one used in Figs. 8.1 and 8.2.

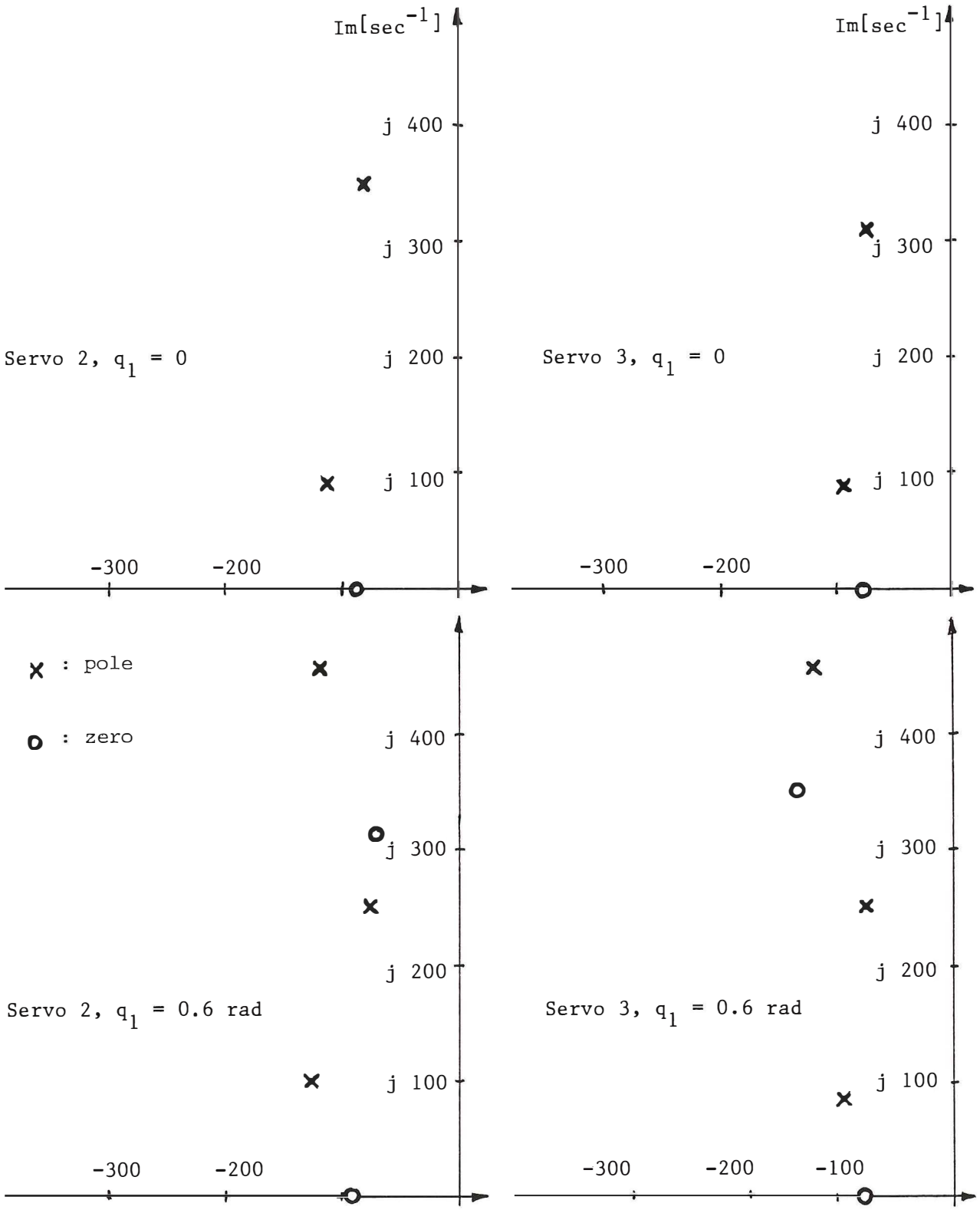

Figure 8.4. Corresponding plots for PI-type servos. Controller parameters are $k_p = 0.45\ \omega_x$; $T_i = 5/\omega_\varphi$

$$\underline{\omega}_x = \begin{bmatrix} 400 \\ 345 \end{bmatrix} s^{-1} \quad ; \quad \underline{\omega}_\varphi = \begin{bmatrix} 421 \\ 384 \end{bmatrix} s^{-1}$$

Apart from the increase in bandwidth, it is seen that the coupling between the two servos may be more noteable than before. However, the system is still robust with respect to changes in the manipulator configuration.

Applying (5.17) and (5.20) as in Section 8.1, the following is obtained, which is an improvement compared to (8.3):

$$\underline{v}_p = \begin{bmatrix} 2.0 \\ 1.7 \end{bmatrix} m/s \quad ; \quad \underline{a}_{pI} = \begin{bmatrix} 152 \\ 119 \end{bmatrix} m/s^2 \qquad (8.6)$$

By applying the internal controller (8.3) to the model developed in Section 7, arbitrarily fast responses may be obtained. However, this will not be the case when applied to the real system. A rough estimate of what can be obtained in practice is found by looking at some of the dynamic effects which were neglected while developing the model. The characteristic frequencies for three of these are

- Link 3 resonance : $\omega_{pf} \approx 10^3$ rad/s
- Spool valve dynamics : $\omega_v \approx 10^3$ rad/s
- Finite system sample rate: $\omega_s \approx 10^3 \sim 10^4$ rad/s

These were considered when inferring (8.5). However, unexpected effects may appear which will reduce the obtainable performance.

8.3. Experiments

The considerations above can be checked against the experimental results described in Appendix A4. Here, controllers 1 and 2

correspond to the controllers described in Section 8.1. Applying (A4.3) and (A4.4), it is found that in controller 1,

$$k_p = 3.3 \text{ rad/s}$$

The same value applies to controller 2 as well, which has the additional

$$T_i = 250 \text{ ms}$$

Applying (5.16) and (5.19) directly, the corresponding performance measures

$$v_P = E\, k_p \approx 0.033 \text{ m/s}$$

$$a_{PI} = E\, k_p / T_i \approx 0.13 \text{ m/s}^2$$

are found for controllers 1 and 2 respectively.

The controllers described in Section 8.2 correspond to controllers 5 and 6 of Appendix A4. Application of (A4.3) through (A4.7) yields

$$k_p = 41 \text{ rad/s}$$

$$g_\tau = 16.5 \cdot 10^{-3} \text{ Nm}^{-1}$$

$$g_v = 0.72 \text{ s}$$

for controller 5. In addition for controller 6 comes

$$T_i = 30 \text{ ms}$$

In these cases, the application of (5.16) and (5.19) results in

$$v_P \approx 0.41 \text{ m/s} \quad ; \quad a_{PI} \approx 13.7 \text{ m/s}^2$$

respectively for controllers 5 and 6. These results show that the performance of the tool tracking system is greatly improved by the use of internal feedback.

Having proven this agreement between the theoretical and the practical results, it is in place to highlight a few disagreements as well. The most eye-catching in this respect is the difference in potential performance. As noted in Section 8.1, the dynamic model is literally far too good to be true. It is believed that this results from errors in the model parameters rather than any of the structural simplifications. The two least reliable parameters in the system are

β : oil bulk modulus

k_λ : leakage constant

which both may be a decade away from the true values. A second, related disagreement is seen from the internal feedback constants g_τ and g_v. The experimentally obtained torque feedback is far stronger than its theoretical counterpart. At the same time, the experimentally obtained velocity feedback is less than the theoretical one. This disagreement may result from errors in β and k_λ, but can also be the result of insufficient noise protection in the experimental system.

It is also interesting to see the difference in the integration constant T_i between a PI-controller designed using the Ziegler-Nichols method and one tuned by trial and error. The first approach will result in a larger T_i than would result from the second method. This indicates that the accelerational capability of the tracking system is more important than is the damping of oscillations.

9. SENSOR MODEL

In this section, a model of a 5-measurements magnetic positional deviation sensor is developed. From the preliminary description in Section 3.1, it follows that the sensor may be divided into 3 subsystems:

1: Solenoids M1 through M4 for the measurment of intermediate deviations p_1 and p_2.

2: Solenoids M5 through M8 corresponding to p_3 and p_4.

3: Solenoids M9 and M10 corresponding to p_5.

For a 6-measurements sensor, a fourth subsystem would be considered which corresponds to deviation p_6.

9.1. Magnetic fields

Some general properties of magnetic fields will be stated. The first concerns the induction field, $\vec{B}$, and states that its net flow through a closed surface s is zero.

$$\iint_S \vec{B}\cdot\vec{n}\, ds = 0 \quad \text{or} \quad \text{div } \vec{B} = 0 \tag{9.1}$$

Here $\vec{n}$ denotes the normal vector of surface S. Magnetic field rotation in a point equals electric current density.

$$\text{curl } \vec{H} = \vec{j} \quad \text{or} \quad \int_L \vec{H}\cdot d\vec{l} = IN \tag{9.2}$$

where L is a closed loop and IN the net electrical current through it. In vacuum

$$\vec{B} = \mu_0 \vec{H} \quad \text{where} \quad \mu_0 = 4\pi \cdot 10^{-7} \text{ Wb/Am} \tag{9.3}$$

and the current density $\vec{j}$ may be assumed zero. In this case, $\vec{H}$ will be a gradient field,

$$\vec{H} = \text{grad (in)} \tag{9.4}$$

where "in" denotes magnetic potential. This, and (9.1) results in Laplaces equation

$$\text{divgrad (in)} = 0 \tag{9.5}$$

Generally, due to the boundary value problem, this equation is difficult to solve. However, a nonambiguous solution always exists. In some cases it is possible to design a simpler problem such that it includes the original boundary conditions. In this way, the original problem is solved as well.

9.2. Two parallel cylinders

The induced voltages in solenoids M1 through M8 are found by considering the magnetic fields in the two planes p_1 - p_2 and p_3 - p_4, defined in Fig. 3.3. Approximations to these fields can be obtained by looking at an ideal configuration of two infinitely long, parallel cylinders with a high magnetic conductivity. Cross sections are shown in Figs. 9.1 and 9.2. Each cylinder is then an equipotential surface.

As a start, the magnetic field between two thin, magnetic conductors will be considered. These are marked P1 and P2 in Fig. 9.1. The potential along a line with distance h_1 from P1 and h_2 from P2 is given by

$$\text{in}(h_1,h_2) = k \ln(h_2/h_1) \tag{9.6}$$

where k is a yet undetermined constant. The magnetic field may be

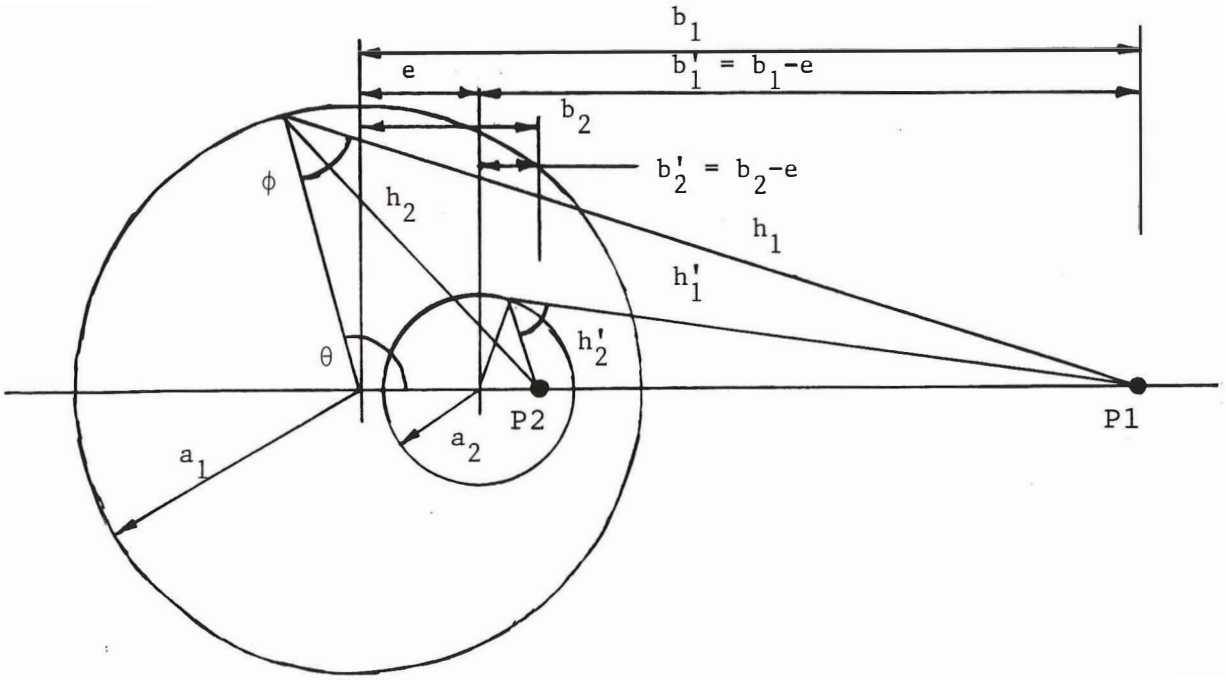

Figure 9.1. Cross section of two parallel cylinders.

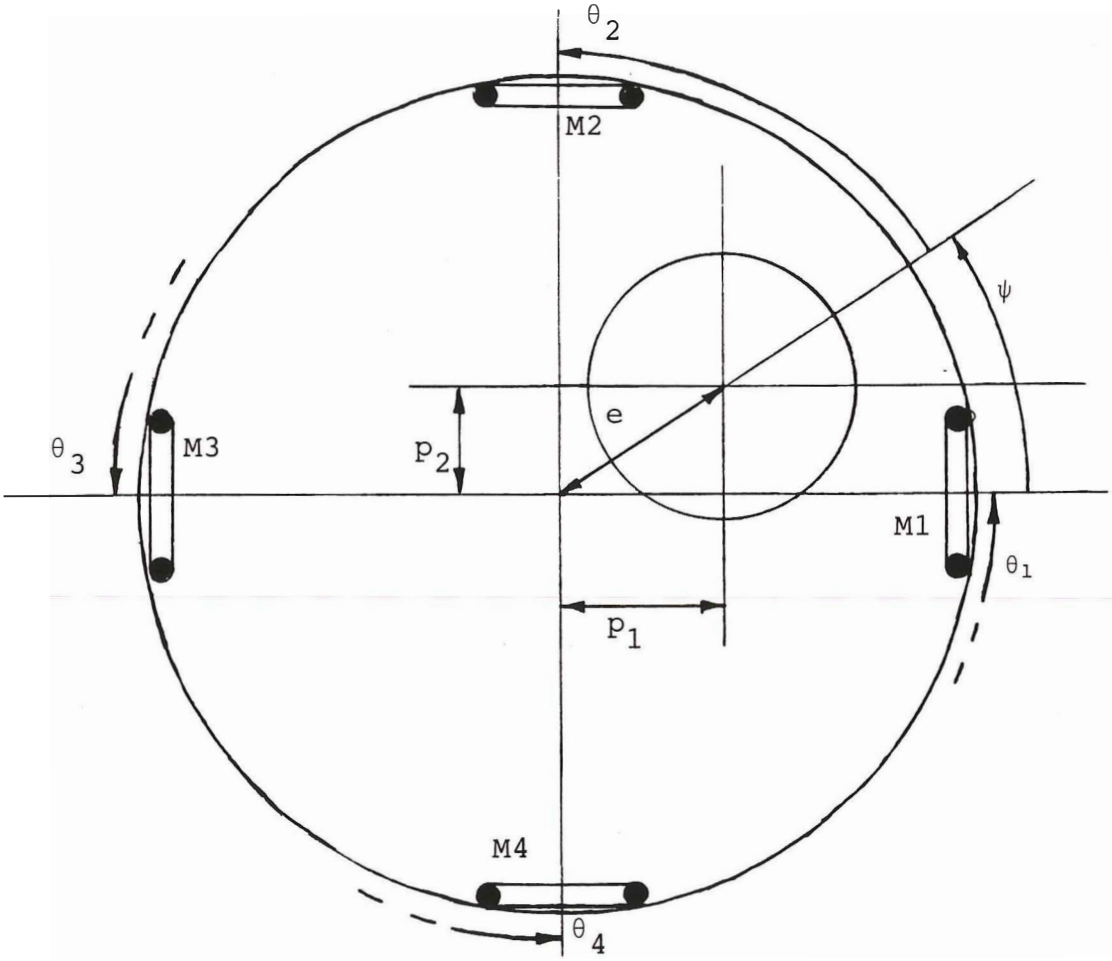

Figure 9.2. Solenoid placement in plane p_1 - p_2.

considered as the sum of two radial fields set up around P1 and P2 respectively. Their magnitudes are given by

$$|\vec{H}_i| = k/h_i \qquad i = 1 \text{ or } 2 \tag{9.7}$$

From (9.6) it follows that the equipotential surfaces in this situation are described by h_1/h_2 constant, which happens to mean circular cylinders. The original problem involves a cylinder of radius a_2 inside a cylinder of radius a_1. Then, in Fig. 9.1, letting

$$b_1 b_2 = a_1^2 \quad \text{and} \quad b_1' b_2' = a_2^2 \tag{9.8}$$

will by Apollonius' theorem imply that

$$\frac{h_1}{h_2} = \frac{b_1}{a_1} \quad \text{and} \quad \frac{h_1'}{h_2'} = \frac{b_1'}{a_2} \tag{9.9}$$

This is proven in Section A5.4. Noting that $b_1' = b_1 - e$ and $b_2' = b_2 - e$, (9.8b) may be written

$$(b_1 - e)(b_2 - e) = b_1 b_2 - (b_1 + b_2)e + e^2 = a_2^2 \tag{9.10}$$

Combining and rearranging yields

$$b_1^2 - \frac{1}{e}(a_1^2 - a_2^2 + e^2)b_1 + a_1^2 = 0 \tag{9.11}$$

and the same for b_2. The solution may be written

$$b_1 = u + v \quad ; \quad b_2 = u - v \tag{9.12}$$

where

$$u = \frac{a_1^2 - a_2^2 + e^2}{2e} \quad ; \quad v = \left[\left(\frac{a_1^2 - a_2^2 + e^2}{2e}\right)^2 - a_1^2\right]^{\frac{1}{2}}$$

This expresses the positions of the imaginary conductors P1 and P2 which result in a magnetic field dependning on e. When these are known, the field is given by (9.7). However, coordinates h_1 and

h_2 are not convenient in the present case. Since the measurement solenoids are located on the outer cylinder, the field will be evaluated on this surface only, and with an angle θ as parameter. Furthermore, since the field by (9.4) is perpendicular to this equipotential cylinder, tangential contributions from (9.7) need not be considered.

By Fig. 9.1 and (9.7), the perpendicular contribution from P1 is

$$H_{1N} = -H_1\cos\varphi = - k \frac{a_1^2 + h_1^2 - b_1^2}{2a_1h_1^2} \tag{9.13}$$

where $\cos\varphi$ was eliminated using the cosine (Extended Pythagorean) equation. Applying the same with respect to θ gives

$$h_1^2 = a_1^2 + b_1^2 - 2a_1b_1\cos\theta \tag{9.14}$$

which inserted into (9.13) gives

$$H_{1N} = - k \frac{a_1 - b_1\cos\theta}{a_1^2 + b_1^2 - 2a_1b_1\cos\theta} \tag{9.15}$$

In the same way, the contribution from P2 is found to be

$$H_{2N} = - k \frac{a_1 - b_2\cos\theta}{a_1^2 + b_2^2 - 2a_1b_2\cos\theta} \tag{9.16}$$

The magnitude of the resulting field is the sum of (9.15) and (9.16). Signs have been chosen so that the field is positive when directed inwards. The field expression may be simplified by replacing b_1 and b_2 by (9.12), the result being

$$H_1 = k \frac{v}{a_1} (u - a_1\cos\theta)^{-1} \tag{9.17}$$

For completeness, constant k must be found. Initially, a potential difference ΔIN between the cylinders was assumed. By (9.4),

$$\Delta IN = in_1 - in_2 = k\ln(h_2/h_1) - k\ln(h_2'/h_1') = k\ln \frac{h_2 h_1'}{h_1 h_2'} \quad (9.18)$$

Applying (9.9) and (9.10), h_2h_1'/h_1h_2' may be expressed in terms of a_1, a_2 and e. If ΔIN is known, (9.18) may be solved for k. This will be done at a later stage. Magnetic field resistance is defined by $R_c = \Delta IN/\Phi$, where the magnetic flux may be determined by a closed surface integral around P1.

$$\Phi = \mu_0 \iint \vec{H} ds = 2\pi h \; L \; \mu_0 k/h = 2\pi L \mu_0 k \quad (9.19)$$

Substitution of k by (9.18) and rearrangement gives

$$R_c = \frac{\Delta IN}{\Theta} = \frac{1}{2\pi L \mu_0} \ln \frac{h_2 h_1'}{h_1 h_2}$$

This is of importance when for instance investigating the inductance of the magnetizing solenoid.

9.3. Radial measurements

Sensor subsystems 1 and 2 each consist of 4 measurement solenoids evenly distributed inside the outer cylinder. Subsystem 1 is shown in Fig. 9.2, which is a drawing of plane p_1 - p_2. Fig. 3.3. The position of the tool marker is described by eccentricity e and angle ψ, alternatively displacements p_1 and p_2. The relationship between these descriptions is

$$p_1 = e \cos \psi \quad ; \quad p_2 = e \sin \psi \quad (9.20)$$

To tie this together with the results from Section 9.2, four angles θ_i corresponding to θ are defined.

$$\theta_1 = -\psi \quad ; \quad \theta_2 = \frac{\pi}{2} - \psi \quad ; \quad \theta_3 = \pi - \psi \quad ; \quad \theta_4 = \frac{3}{4}\pi - \psi \quad (9.21)$$

Substitution of ψ in (9.20) gives

$$p_1 = e\cos\vartheta_1 = e\sin\vartheta_2 = -e\cos\vartheta_3 = -e\sin\vartheta_4$$

$$p_2 = -e\sin\vartheta_1 = e\cos\vartheta_2 = e\sin\vartheta_3 = -e\cos\vartheta_4 \qquad (9.22)$$

Each angle ϑ_i represents the position of solenoid Mi relative to the axis defined by angle ψ. Thus, if H_i denotes the magnetic field at Mi, four equations

$$H_i = k\frac{v}{a_1}\left(u - a_1\cos\vartheta_i\right)^{-1} \qquad (9.23)$$

result from (9.17). Substitution of $\cos\vartheta_i$ by (9.22) results in

$$H_1 = k\frac{v}{a_1}\left(u - \frac{a_1}{e}p_1\right)^{-1}$$

$$H_2 = k\frac{v}{a_1}\left(u - \frac{a_1}{e}p_2\right)^{-1} \qquad (9.24)$$

$$H_3 = k\frac{v}{a_1}\left(u + \frac{a_1}{e}p_1\right)^{-1}$$

$$H_4 = k\frac{v}{a_1}\left(u + \frac{a_1}{e}p_2\right)^{-1}$$

Now, four measurements for the estimation of two deviational quantities are available. However, the computations involved seem complicated. Because of this, the number of measurements will be reduced to two by defining

$$y_1 = \frac{H_1 - H_3}{H_1 + H_3} \quad \text{and} \quad y_2 = \frac{H_2 - H_4}{H_2 + H_4} \qquad (9.25)$$

A similar reduction is made for sensor subsystem 2,resulting in y_3 and y_4. Inserting (9.24) into (9.25) gives

$$y_1 = \frac{a_1}{ue}p_1 \quad \text{and} \quad y_2 = \frac{a_1}{ue}p_2 \qquad (9.26)$$

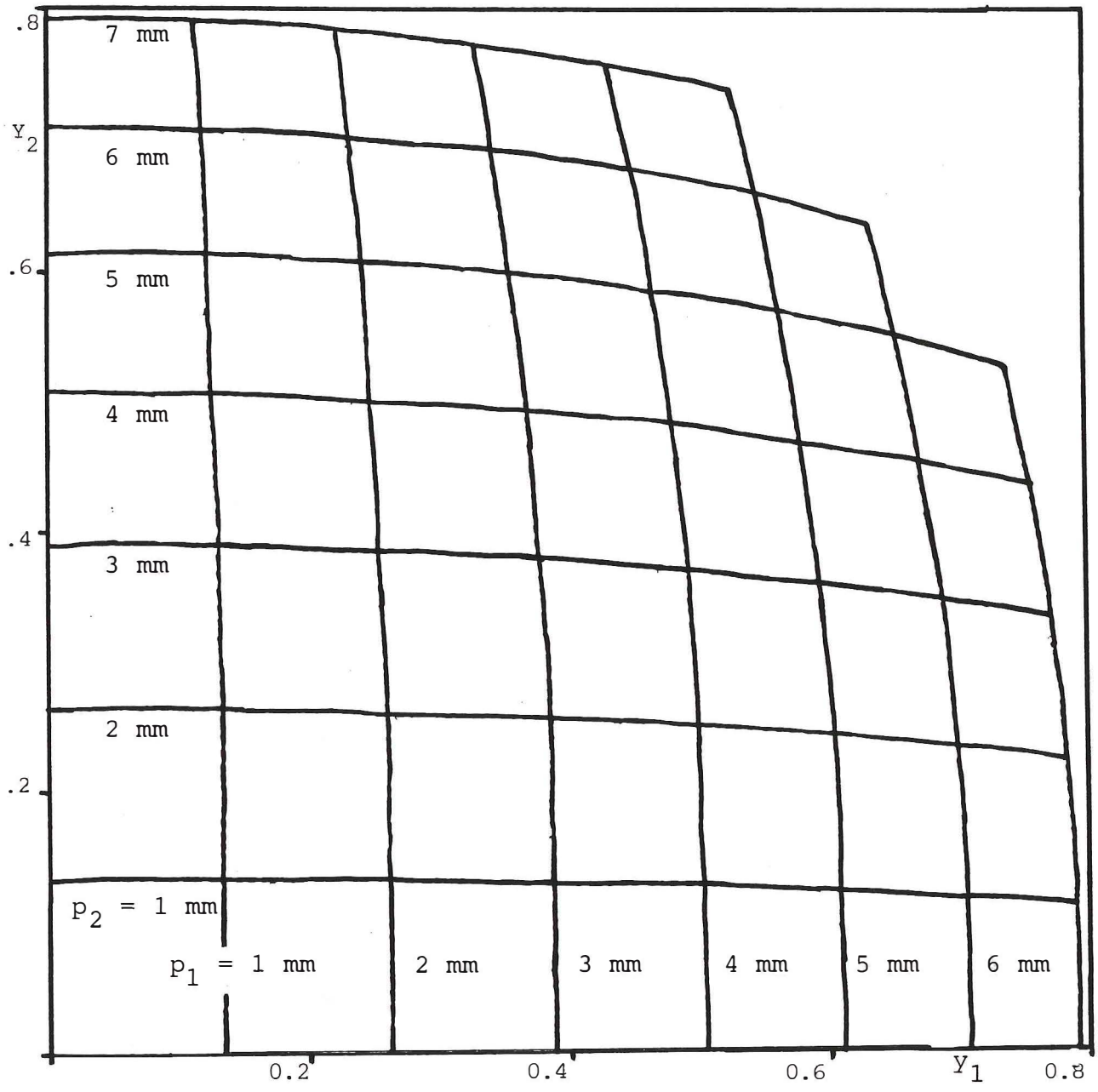

Figure 9.3. Mapping (9.26). Constant-p_1 and p_2-lines in the upper right quadrant of plane y_1-y_2.

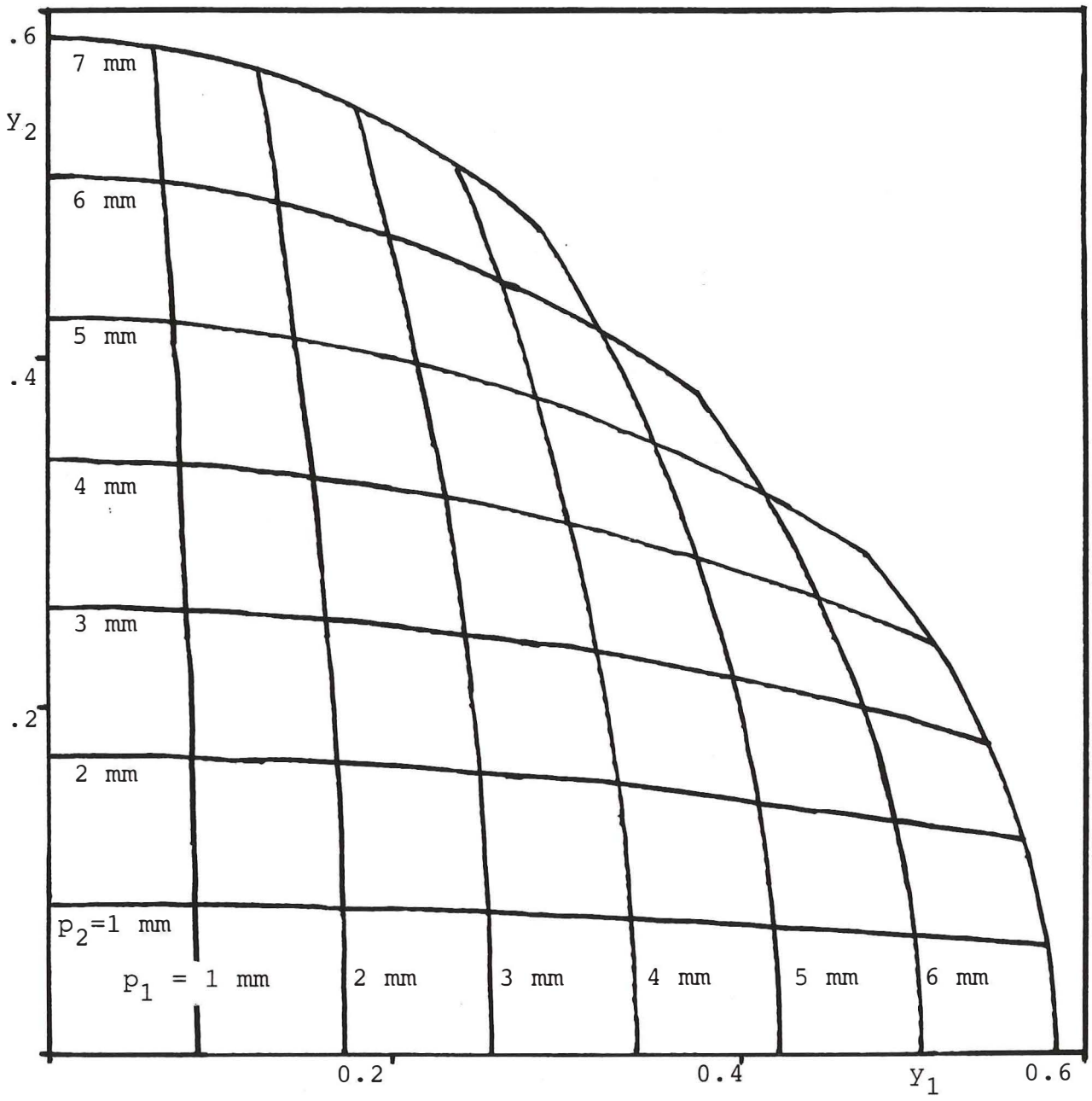

Figure 9.4. Mapping (9.28) with relative leakage factor $a_1/h_0 = 0.56$.

These are computationally more handy than (9.24), however it must be noted that they are not linear since by (9.12),

$$\frac{a_1}{ue} = \frac{2a}{a_1^2 - a_2^2 + e^2} \tag{9.27}$$

where again $e^2 = p_1^2 + p_2^2$.

The idealized system considered in Section 9.1 represents the real situation very well. However, one important effect is neglected. The real sensor does not consist of infinite cylinders, but of two closely spaced sets of short cylinders. It is likely that some flux lines pass through the measurement solenoids without being led through the tool marker (see Figs 3.2 or 9.5). This leakage is easily determined by removing the tool marker and observing the remaining magnetic field. It may also be estimated from the calibrational results in Appendix A5.3. Due to symmetry, leakage through all solenoids are considered equal and denoted by the constant H_0. To take this effect into account, H_0 is added to each expression in (9.24). If reductions (9.25) are used, the result will be

$$y_1 = \frac{a_1}{ue} p_1\{1 + \frac{a_1 ue}{h_0 ve}[1 - (\frac{a_1}{ue} p_1)^2]^{-1}\}$$

$$y_2 = \frac{a_1}{ue} p_2\{1 + \frac{a_1 ue}{h_0 ve}[1 - (\frac{a_1}{ue} p_2)^2]^{-1}\} \tag{9.28}$$

where $h_0 = k/H_0$. Since now even k must be computed, these should be avoided in practice. An easier approach is to modify the measurement reduction formula (9.25) to

$$\tilde{y}_1 = \frac{H_1 - H_3}{H_1 + H_3 - 2H_0} \quad \text{and} \quad \tilde{y}_2 = \frac{H_2 - H_4}{H_2 + H_4 - 2H_0} \tag{9.29}$$

which once again results in Eqs. (9.26). This measurement function is shown in Fig. 9.3. This, and reduction (9.29), is

used in the experiments. However, the calibrational results presented in Appendix A5.3 are based on (9.25), which results in (9.28). For this reason, a further discussion of this equation is necessary.

All elements of (9.28) are easily obtained, except for denominator h_0. As mentioned,

$$h_0 = k/H_0 \tag{9.30}$$

or by applying (9.19),

$$\frac{1}{h_0} = \frac{H_0}{k} = 2\pi L\mu_0 \frac{H_0}{\Phi} \tag{9.31}$$

where Φ is the total flux of the sensor. The characteristics described in Appendix A5.1 only show small variations in Φ with respect to eccentricity e. Due to this, h_0 will be assumed constant in (9.28). Experimental adjustment of the relative leakage factor a_1/h_0 yields the plots in Figs. 9.4 and A5.4. These match the calibrational data very well. Because of this, it will be assumed that (9.26) subject to (9.29) is equally correct.

9.4. Axial measurements

Axial displacement is measured by solenoids M9 and M10, Figs. 3.2 and 9.5. The magnetic field distribution in this direction is more complicated to obtain than was the case radially. This is due to the complexity of the border value problem. Because of this, an approximation will be given which may be adjusted by calibration.

Axial flux through the tool marker may be considered to be piecewise linear. This follows if the magnetic field between the tool marker and the sensor housing is limited to, and evenly distributed along, lengths L in Fig. 9.5. Accumulated flux in the tool marker is given in M-coordinates (fixed to the housing) as

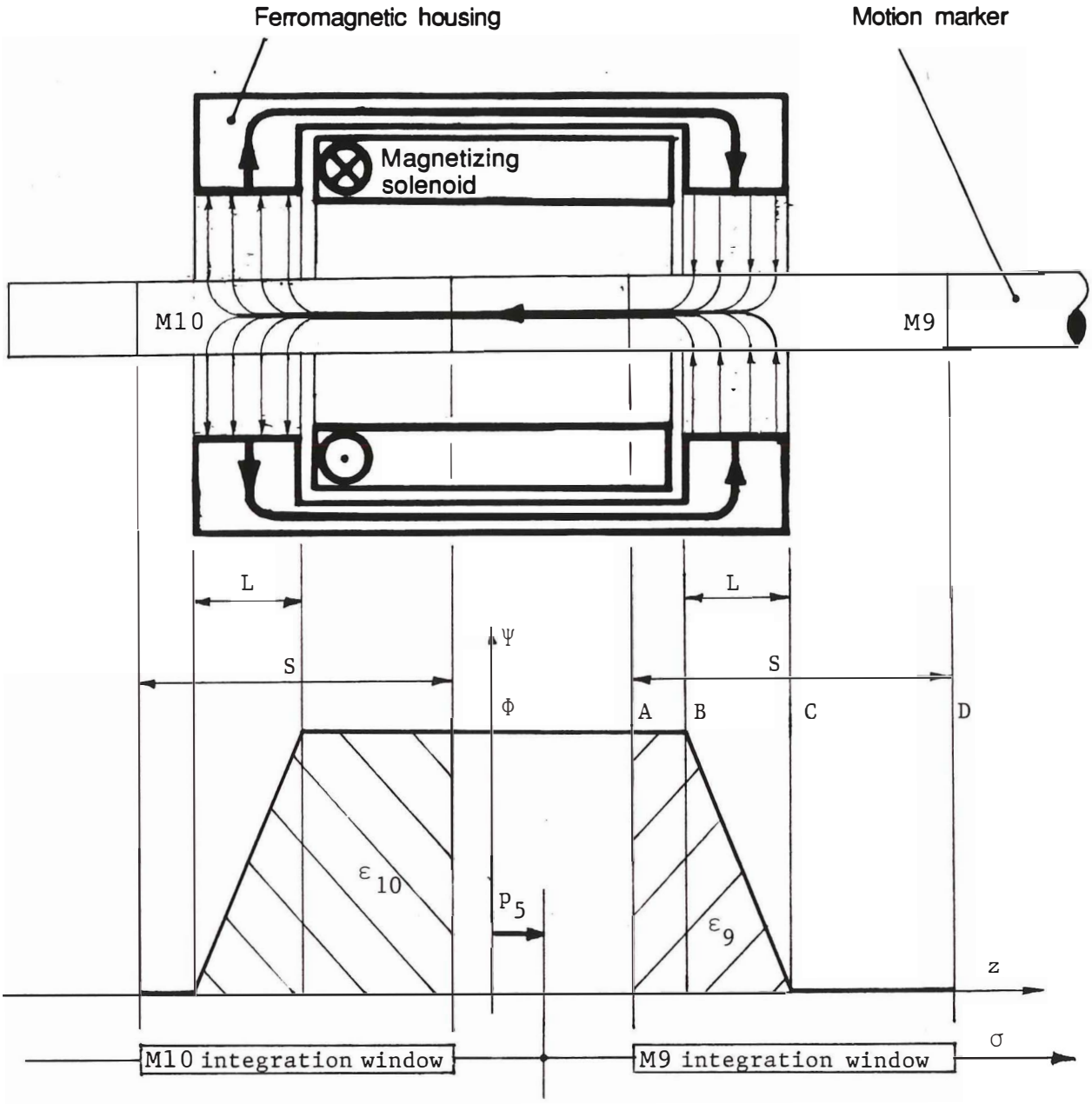

Figure 9.5. Flux distribution in axial measurement solenoids M9 and M10. Induced emf is found by moving the indicated integration windows according to p_5.

$$\Psi(z) = \begin{cases} \Phi & |z| \leq B \\ \Phi(1 - \frac{z-B}{L}) & B \leq |z| \leq C \\ 0 & C \leq |z| \end{cases} \qquad (9.32)$$

Measurement solenoids M9 and M10 are wound around the tool marker. In each single winding the electromagnetic force

$$\varepsilon'(z) = \pi a_2^2 \omega \Psi(z) \qquad (9.33)$$

is induced. Here ω denotes flux frequency. The total emf induced in solenoid M9 is then

$$\varepsilon_9 = \int_{-\infty}^{\infty} \varepsilon'(z) \frac{\partial n}{\partial z} dz \qquad (9.34)$$

The density of the solenoid windings, $\partial n/\partial z$, may be considered as an integrational window which is fixed to the tool marker. Considering Fig. 9.5,

$$\varepsilon_9 = \frac{\pi a_2^2 \omega \Phi N}{S} (\frac{S}{2} - p_5) \qquad (9.35)$$

In the same way

$$\varepsilon_{10} = \frac{\pi a_2^2 \omega \Phi N}{S} (\frac{S}{2} + p_5) \qquad (9.36)$$

The measurement reduction formula

$$y_5 = \frac{\varepsilon_{10} - \varepsilon_9}{\varepsilon_{10} + \varepsilon_9} \qquad (9.37)$$

finally results in

$$y_5 = \frac{2}{S} p_5 \qquad (9.38)$$

where, by Fig. 9.5, S denotes the length of each measurement

solenoid. Note that strictly, this function is only valid for

$$-\frac{1}{2}(S-L) \lesssim p_5 \lesssim \frac{1}{2}(S-L) \tag{9.39}$$

which may be compared to restriction (4.4) in Section 4.2.

Using the value for S given in Appendix A5.1 and comparing to the results in A5.3, it is seen that (9.37) represents a good, linear approximation. However, higher order polynomials give even better approximations and are recommended for motion recording purposes.

10. INVERSE SENSOR MODEL

As the name suggests, the purpose of the positional deviation sensor is to obtain estimates of relative position. For this reason, inverse measurement functions are desired. In general, given an arbitrary number of measurement solenoids M1 through MN and their outputs as functions of positional deviation, a non-linear multi-dimensional state estimation problem appears. An iterative solution procedure which also consideres the dynamics of the manipulator may thus be given in terms of an extended Kalman filter. However, even if the result is a minimum variance estimate of the state vector, the computational load may imply low data rates. For this reason, simpler schemes are sought which supply estimates at higher rates.

10.1 Separate subsystems

Assuming reduction formula (9.29), the measurement function for subsystem 1 is

$$\begin{bmatrix} y_1 \\ y_2 \end{bmatrix} = \frac{2\ a_1}{a_1^2 - a_2^2 + e^2} \begin{bmatrix} p_1 \\ p_2 \end{bmatrix} \qquad (10.1)$$

A similar function is obtained for subsystem 2. Noting that $e^2 = p_1^2 + p_2^2$, this may be solved for $[p_1,\ p_2]^T$. The result is somewhat complicated, and numerical problems arize near $[y_1,\ y_2]^T = \underline{0}$. Due to this, other means will be sought for solving (10.1).

Eq. (10.1) can be written

$$\underline{p} = c_r(\underline{p})\underline{y} \tag{10.2}$$

where $c_r = (a_1^2 - a_2^2 + p_1^2 + p_2^2)/a_1$

or $$c_r = \frac{1}{a_1}\,[a_1^2 - a_2^2 + c_r^2(y_1^2 + y_2^2)] \tag{10.3}$$

By manipulation this results in

$$|\underline{y}|^2\, c_r^2 - a_1 c_r + a_1^2 - a_2^2 = 0 \tag{10.4}$$

This may be used to solve for c_r symbolically, resulting in the problems stated above. Alternatively, (10.4) may be solved by Newton´s method. The iteration

$$c(k+1) = c(k) - \frac{(a_1^2 - a_2^2) - a_1 c(k) + |\underline{y}|^2 c^2(k)}{-a_1 + 2|\underline{y}|^2 c(k)}$$

results in an error of relative magnitude 10^{-3} after two iterations. To achieve this, a carefully chosen fixed initial value c_0 is used.

The structure of the TMS 32020 signal processor, which is used for the experiments in Section 8, implies that fairly large polynomials may be evaluated within the time needed for a single division. Because of this, the denominator in (10.5) should be replaced by a polynomial approximation. However, an even better approach may be to represent factor c_r directly by a symmetric polynomial function of $|\underline{y}|$.

$$c_r = c_r(\underline{p}(\underline{y})) = c_0 + c_2|\underline{y}|^2 + \ldots \tag{10.6}$$

The number of terms depend on the need for accuracy, which is discussed in Section 10.3. As an example, a single constant c_0 was used in the preliminary experiments described in Section 5.3. Indicative computational errors, compared to (10.3), for a few polynomials of different order are for

order 0: max 0.3 mm absolute error

order 2: max 0.04 mm "

order 4: max 0.012 mm "

The two latter are presented in Fig. 10.1. Note that these curves, and those in Fig. 10.2, are least-squares curve fits. Better results may be obtained by L^{∞}-approximations.

The measurement function for subsystem 3, which represents axial deviation, is given by Tables A5.3 and A5.4 (Appendix A5). Neglection of the coupling from radial displacement results in the inverse measurement function

$$p_5 = c_a(y_5)y_5 \tag{10.7}$$

where factor c_a may be represented by a polynomial expansion similar to (10.6). The computational error for two of these are shown in Fig. 10.2. The plots have been subject to extensive "wild point editing" which was necessary since the polynomials are compared to experimental data. The figure indicates that as long as y_5 stays within <-20 mm, 20 mm>, the results are

order 2: max 0.25 mm absolute error

order 4: max 0.1 mm "

Studying Fig. A5.7, it is seen that errors of 2 mm approx. may be the result of approximation by a constant.

10.2 Coupling terms

From the calibrational results in Appendix A5.3, it is seen that radial rotation affects measurements y_1 and y_2. It also appears that radial translation affects y_5. Due to the symmetry of the sensor, coupling will be assumed symmetric in its arguments.

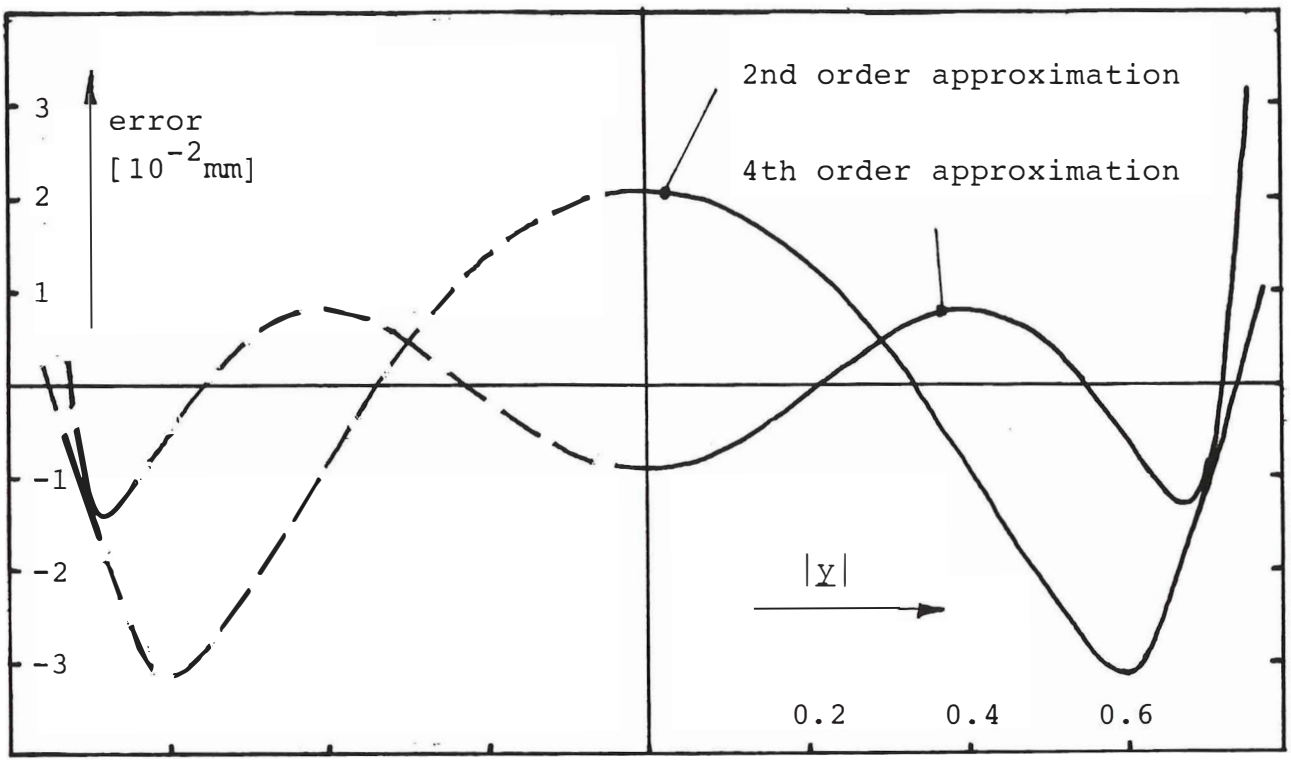

Figure 10.1. Approximation errors for two polynomial expansions of coefficient $c_r(\underline{p}(\underline{y}))$.

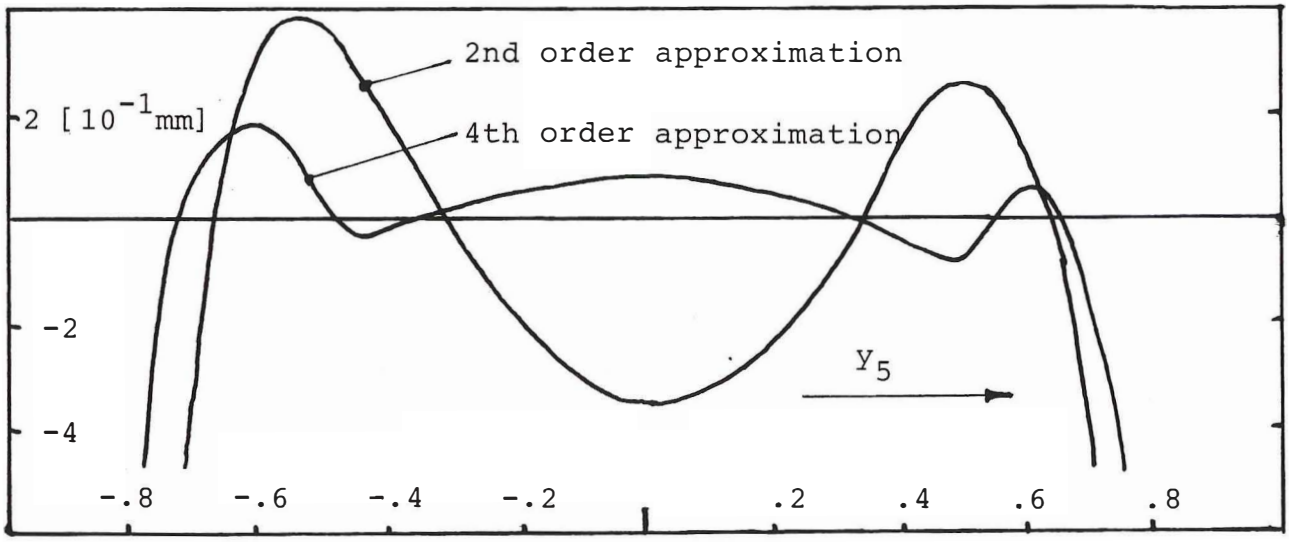

Figure 10.2. Approximation errors for two polynomial expansions of coefficient $c_a(y_5)$.

The extension to coupling from all elements in $\underline{p}$ is in each case fairly obvious, and will not be emphasized.

Coupling effects on y_5 may be estimated from Tables A5.3 and A5.4. An approximation of y_5 which seems to hold for p_5 within <-15 mm, 15 mm> is

$$y_5 = \frac{1}{c_a} [1 + (0.93\ 10^{-3}\ \text{mm}^{-2}) d^2] p_5 \qquad (10.8)$$

where c_a is given by (10.7) and $d^2 = d_1^2 + d_2^2$ is defined by (3.2). Neglecting this coupling may lead to errors of up to 10% within the given range, while inclusion reduces this to approximately 2%. At full scale, this corresponds to measurement errors of 2 mm and 0.4 mm respectively.

Turning to measurements y_1 and y_2, the influence from radial rotation is determined by considering Tables A5.1, A5.2 and A5.6. At 0.1 rad rotational deviation, the coupling is of the same order of magnitude as the modeling error, Table A5.2, and could thus have been neglected. However, following the discussion in Appendix A5.3, it may increase by a factor of 10. The sparse data in Table A5.6 is not sufficient to deduce good approximations of the coupling terms. As an indication, (9.26) may be augmented to

$$\begin{bmatrix} y_1 \\ \\ y_2 \end{bmatrix} = \frac{a_1}{ue} \begin{bmatrix} 1 - \delta_1^2 + \delta_2^2 & 0 \\ \\ 0 & 1 + \delta_1^2 - \delta_2^2 \end{bmatrix} \begin{bmatrix} p_1 \\ \\ p_2 \end{bmatrix} \qquad (10.9)$$

which is an elliptical modification of the decoupled measurement equation.

The introduction of coupling makes the inversion of the measurement equation more complicated. It is now necessary to consider the complete 5-by-5 or 6-by-6 system. The following discussion will be based on an arbitrarily complex and exact theoretical measurement function

$$\underline{y} = Q(\underline{p}) \tag{10.10}$$

which may be based on electromagnetical field theory, polynomial expansions or look-up tables. Examples will be given in terms of the previous results. In general, symbolic expressions for the inverse of (10.10) are difficult to obtain, and may be extremely complex. Presently, methods for obtaining approximate solutions will be discussed. Simplifications in the schemes will be based on the assumption of weak coupling and on partitioning.

In the same way as for the inverse kinematics discussed in Section 5.1 and Appendix A1.1, partitioning reflects one-way dependence. In the present case it is obvious that measurements

y_1 through y_4 do not depend on p_5 or p_6

y_5 does not depend on p_6

This can be seen from Fig. 3.2. A linear or linearized transformation of this type may be represented by the matrix

$$Q = \begin{bmatrix} q_{11} & q_{12} & q_{13} & q_{14} & 0 & 0 \\ q_{21} & q_{22} & q_{23} & q_{24} & 0 & 0 \\ q_{31} & q_{32} & q_{33} & q_{34} & 0 & 0 \\ q_{41} & q_{42} & q_{43} & q_{44} & 0 & 0 \\ q_{51} & q_{52} & q_{53} & q_{54} & q_{55} & 0 \\ q_{61} & q_{62} & q_{63} & q_{64} & q_{65} & q_{66} \end{bmatrix} = \begin{bmatrix} & \tilde{Q} & & \underline{0} & \underline{0} \\ & & & & \\ & & & q_{55} & 0 \\ & \underline{q}_5^T & & & \\ & \underline{q}_6^T & & q_{65} & q_{66} \end{bmatrix} \tag{10.11}$$

$$Q^{-1} = \begin{bmatrix} & \tilde{Q}^{-1} & & \underline{0} & \underline{0} \\ & & & & \\ & -q_{55}^{-1}\underline{q}_5^T\tilde{Q}^{-1} & & q_{55}^{-1} & 0 \\ -q_{66}^{-1}(\underline{q}_6^T - q_{65}q_{55}^{-1}\underline{q}_5^T)\tilde{Q}^{-1} & & -q_{66}^{-1} & q_{65}\, q_{55}^{-1} & q_{66}^{-1} \end{bmatrix} \tag{10.12}$$

Inversion is in this case simplified since only a 4-by-4 matrix inversion takes place. Q( ) in (10.10) is nonlinear however, and the result may not be used directly. Instead, a sequential scheme is applied which

1: Obtains $p_1 \ldots p_4$ from $y_1 \ldots y_4$

2: Obtains p_5 from y_5 and $p_1 \ldots p_4$

3: Obtains p_6 from y_6 and $p_1 \ldots p_5$

At present, the 3rd step is omitted since only 5 measurements are available.

Considering the second step first, and assuming that (10.8) is correct, p_5 is obtained by

$$d^2 = \frac{1}{4}\left[(p_1 + p_3)^2 + (p_2 + p_4)^2\right] \tag{10.13}$$

$$p_5 = c_a(y_5)[1 + \text{const} \cdot d^2]^{-1} y_5 \tag{10.14}$$

In general a nonlinear scalar function is inverted, which in the present context is a fairly trivial problem.

Equation (10.13) depends on results from the inversion of

$$\tilde{\underline{y}} = \tilde{Q}(\tilde{\underline{p}}) \tag{10.15}$$

where $\tilde{\underline{y}} = [y_1 \ldots y_4]^T$, $\tilde{\underline{p}} = [p_1 \ldots p_4]^T$ and $\tilde{Q}$: $R^4 \longrightarrow R^4$. As an approximate example,

$$\begin{bmatrix} y_1 \\ y_2 \end{bmatrix} = \frac{2a_1}{a_1^2 - a_2^2 + p_1^2 + p_2^2} \begin{bmatrix} 1-\gamma & 0 \\ 0 & 1+\gamma \end{bmatrix} \begin{bmatrix} p_1 \\ p_2 \end{bmatrix}$$

$$\begin{bmatrix} y_3 \\ y_4 \end{bmatrix} = \frac{2a_1}{a_1^2 - a_2^2 + p_3^2 + p_4^2} \begin{bmatrix} 1-\gamma & 0 \\ 0 & 1+\gamma \end{bmatrix} \begin{bmatrix} p_3 \\ p_4 \end{bmatrix} \qquad (10.16)$$

is obtained from (10.9) and (10.1). Here, by (3.2)

$$\gamma = \delta_1^2 - \delta_2^2 = \frac{1}{b^2}\left[(p_4 - p_2)^2 - (p_1 - p_3)^2\right] \qquad (10.17)$$

The equations serve as indications only. As mentioned, arbitrary functions $\tilde{Q}$ are considered. Two approaches for solving (10.15) are now outlined.

Iterative solution: The equation may be solved by Newton's method. Considering the equation

$$\Delta\underline{\tilde{y}} = \underline{\tilde{y}} - \tilde{Q}(\underline{\tilde{p}}) \qquad (10.18)$$

where $\Delta\underline{\tilde{y}} = 0$ is desired, the interation

$$\underline{\tilde{p}}(k+1) = \underline{\tilde{p}}(k) + J_{py}^{-1}\,\Delta\underline{\tilde{y}} \qquad (10.19)$$

is obtained, where J_{py} is the Jacobian of $\tilde{Q}(\ )$. Determination and inversion of this matrix is generally time consuming, and should be avoided. This may be done by considering the approximate inverse function given by (10.2) with (10.6) inserted. Approximation of c_r by the constant c_0 gives

$$J_{py}^{-1} = J_{yp} = c_0 I \qquad (10.20)$$

Higher order approximations may result in faster convergence. By considering polynomial expansions of the inverse measurement equation, differentiation is simplified and matrix inversion

avoided.

Approximate, symbolic solution: Since weak coupling is assumed, a natural approach is to consider (10.16) first with $\gamma = 0$. This was done in Section 10.1. Inversion results in two 2-by-2 systems of the form

$$\underline{p} = c_r(\underline{y})\underline{y} \tag{10.21}$$

When these are obtained, approximate coupling may be inserted by assuming for instance

$$\begin{bmatrix} p_1 \\ p_2 \end{bmatrix} = c_r(y_1, y_2) \begin{bmatrix} 1-\eta & 0 \\ 0 & 1+\eta \end{bmatrix} \begin{bmatrix} y_1 \\ y_2 \end{bmatrix}$$

$$\begin{bmatrix} p_3 \\ p_4 \end{bmatrix} = c_r(y_3, y_4) \begin{bmatrix} 1-\eta & 0 \\ 0 & 1+\eta \end{bmatrix} \begin{bmatrix} y_3 \\ y_4 \end{bmatrix} \tag{10.22}$$

where η may be a polynomial function of $\tilde{\underline{y}}$, This may be obtained by using an offline curve fitting scheme. The shape of (10.22) is chosen to resemble (10.16), but may take other forms as well. This approach is based on trial and error, and arbitrarily precise results may be obtained.

Once $\tilde{\underline{p}}$ is found, it may be inserted into (10.13). In (10.14), p_5 is obtained by an approximate, symbolic solution, however iteration could have been used here as well.

11. CONCLUSION AND RECOMMENDATIONS

The basic control principles and problems were described in Section 5. From this it became evident that the tracking performance in terms of steady state velocity or acceleration depends on the sensor range and on the servo bandwidth. Hence, means for improving the performance were sought along two different directions:

1. Optimizing the use of the sensor´s "workspace".
2. Improving the control system bandiwidth.

Attempts in direction 1 were described in Section 6, where it is shown by an example that significant improvements are possible however depending on the kinematic properties of the manipulator, and the mounting of the sensor.

Prior to the investigations in the second direction, a detailed dynamic model was developed in Section 7 for servos 2 and 3 of the manipulator at hand. This included the first elastic mode of link 3, which is shown to reduce the bandwidth of servo 3 by a factor of 2 approx. if not compensated for. In Section 8 it is proved both theoretically and experimentally that a considerable increase in the servo bandwidth can be obtained by introducing feedback from force (pressure) and velocity. The first is believed to have a positive influence on factor α, whereas the velocity feedback will enable increases in ω_φ. Both factors appear in (5.17) and (5.20). The experiments have shown that a system for real-time manual training of high-speed paint-spraying robots is well within reach.

Investigations concerning the measurement equations of the positional deviation sensor are presented in Sections 8, 9 and A5. These prove a nice correspondence between the theoretical and the

experimental results. It is shown that the inversion of the measurements (computation of positional deviation) can be carried out by simple yet reasonably accurate means. No investigation of dynamic performance vs sensor exactness has been made, since the accuracy is believed to be a problem only in connection with precise motion recording.

The success of the presented manual training system relies on the quality of a large number of elements. This dissertation has been dealing with control problems and the development of the sensor in addition to giving the outlines of the system. Apart from this, items of practical importance include

1. System cost
2. System safety

The first item comes up since it is essencial from the point of view of marketing. Cost reduction is largely a technical problem, but involves control theory when considering economical computer systems and interfaces. Key components in the improved tracking system in Section 8 are the pressure sensors, which are expensive both to purchase and to install. These can be avoided however, if a sufficiently precise state estimator is made available. Thus, research in this area should be intensified. A second, cost optimization, problem concerns the sampling rates and the extent of multiplexing used to simplify the control system hardware. This as well can be analyzed using the theory of state estimation.

The question of safety is brought forward since the presented concept necessitates that a human being is present in the workspace of an activated manipulator. It was stated in Section 1 that the use of a tool marker is safer than the use of a joy-stick or similar since the operator in the first case wields better control. However, considering the possibility of system mal-function, it is necessary to take adequate precautions. Means for improving the safety can include

1. Exhaustive system surveillance with automatic notification and shut-down capabilities.

2. Duplication of vital components in order to enable graceful shut-downs.

3. Collision predictors and dampers.

This outlines a large area for research and development even though the principles are well known. The above means are not common in today´s robotics where instead negative precautions such as speed limitations and fences have been made the rule. It is the author´s belief that the above described non-killer will function under lesser restrictions, enabling true interaction between man and machine.

REFERENCES

Alexander, I., H. Farreny, M. Ghallab (1986). Robot Technology: Vol. 6, Decision and Intelligence. (Kogan Page, London).

ASEA (1984). Programming Manual CK 09-1401 E, IRB --/02.

Balchen, J.G. (1984). Norwegian Patent Application 870419.

Blume, C., W. Jakob (1986). Programming Languages for Industrial Robots. (Springer, Berlin).

Bolt, R.A. (1984). The Human Interface. (Lifetime Learning Publications, Belmont, CA).

Dessen, F. (1985). Koordinatkonvertering for styring av robotmanipulatorer. Report 85-27-U, Div. of Engr. Cybernetics, Norwegian Inst. of Tech.

Engelberger,J. (1980). Robotics in Practice. (Kogan Page, London).

Findeisen, W., F.N. Bailey et al. (1980). Control and Coordination in Hierarchical Systems. (John Wiley, New York).

Foley, J.D. (1987). Interfaces for Advanced Computing. Scientific American, 257 (10), 83-90.

Fu, K.S., R.C. Gonzalez, C.S.G. Lee (1987). Robotics. (McGraw-Hill, New York).

Hayward, V., R.P.C. Paul (1986). Robot Manipulator Control under Unix. RCCL: A Robot Control "C" Library. Int. J. of Robotics Research, 5(4), 94-111.

Hirzinger, G. (1982). Robot-teaching via force-torque-sensors. 6th Eur. Meeting on Cybernetics and Systems Research EMCSR 82, April 13-16.

Hirzinger, G., J. Heindl (1983). Sensor programming - a new way for teaching robot paths and forces/torques simultaneously. 3rd Int. conf. on Robot Vision and Sensory Controls RoViSeC 3, Cambridge, MA.

Hollerbach, J.M., G. Sahar (1983). Wrist-Partitioned, Inverse Kinematic Accelerations and Manipulator Dynamics. Int. J. of Robotics Research, 2(4), 61-76.

Ishii, M., S. Sakane, M. Kakikura, Y. Mikami (1987). A 3-D Sensor System for Teaching Robot Paths and Environments, Int. J. of Robotics Research, 6(2), 45-59.

Khatib, O. (1985). Real-time Obstacle Avoidance for Manipulators and Mobile Robots. 1985 IEEE Int. Conf. on Robotics and Automation, St. Louis, March 25-28, 500-505.

Kokotovic, P.V., R.E. O'Malley, P. Sannuti (1976). Singular Perturbations and Order Reduction. An Overview. Automatica, 12, 123-132.

MacFarlane, A.G.J., I. Postlethwaite (1977). Generalized Nyquist stability criterion and multivariable root loci. Int. J. of Control, 25, 81-127.

Meriam, J.L. (1975). Dynamics. (John Wiley, New York).

Mesarovic, M.D., D. Macko, Y. Takahara (1970). Theory of Hierarchical, Multilevel, Systems. (Academic Press, New York).

Parent, M., C. Largeau (1984). Robot Technology: Vol. 5, Logic and Programming. (Kogan Page, London).

Paul, R.P. (1981). Robot Manipulators. (MIT-Press, Cambridge, MA).

PC Electronics (1986). Bugbust, A Development System for the TMS32020 Signal Processor.

PC Electronics (1987). Simon 20, Symbolic Interactive Monitor for TMS 32020 Signal Processor.

Texas Instruments (1986). TMS 32020 User's Guide.

Trallfa Robot (1982a). TR-4000 System Description.

Trallfa Robot (1982b). TR-4000 Operator's Manual.

Trallfa Robot (1986). Robtalk/TSM Manual.

Vertut, J., P. Coiffet (1985). Robot Technology: Vol. 3, Teleoperation and Robotics. (Kogan Page, London).

Yoshikawa, T. (1985). Manipulability and Redundancy Control of Robotic Mechanisms, 1985 IEEE Int. Conf. on Robotics and Automation, St. Louis, March 25-28, 1004-1009.

A1. KINEMATICS OF THE TR 400

The manipulator used in the experiments is a 5 d.o.f. hydraulically driven TR 400 from Trallfa Robot AS. The quantities necessary for a kinematic description are shown in Fig. A1.1. Angle θ_1 defines base rotational displacement, θ_2 the angle between link 2 and the vertical axis, θ_3 the angle between link 3 and the horisontal plane. Angles θ_4 and θ_5 are wrist rotations and defined relative to the preceeding link. Mechanical constants are a_2, a_3, which denote the length of link 2 and link 3 respectively, and D which is the offset between the neutral axis of link 3 and the axis of joint 5.

A1.1 The manipulator Jacobian

Coordinate system 5 is defined fixed to link 5 and with origo in the intersection point between axes 4 and 5. System 3 is defined fixed to link 3, but with the same origo as system 5. The homogeneous transformation matrix from base coordinates to system 3 is then given by

$$H_3 = \begin{bmatrix} & R_3 & & \underline{p}_3 \\ & & & \\ & \underline{0}^T & & 1 \end{bmatrix} \qquad \text{(A1.1)}$$

where

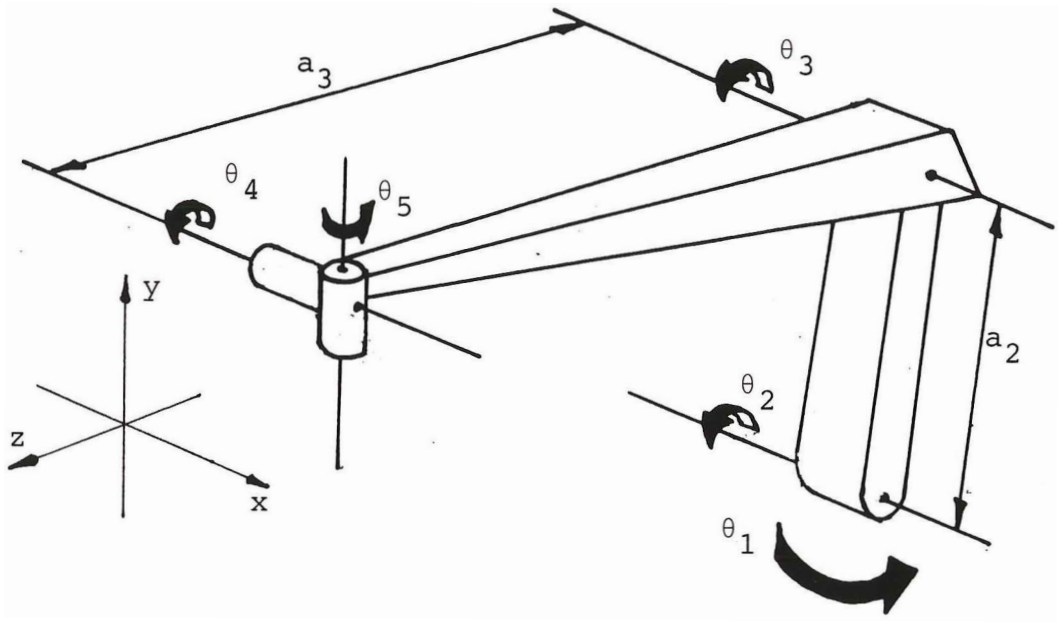

Figure A1.1. Structure and notation for the TR 400 kinematics.

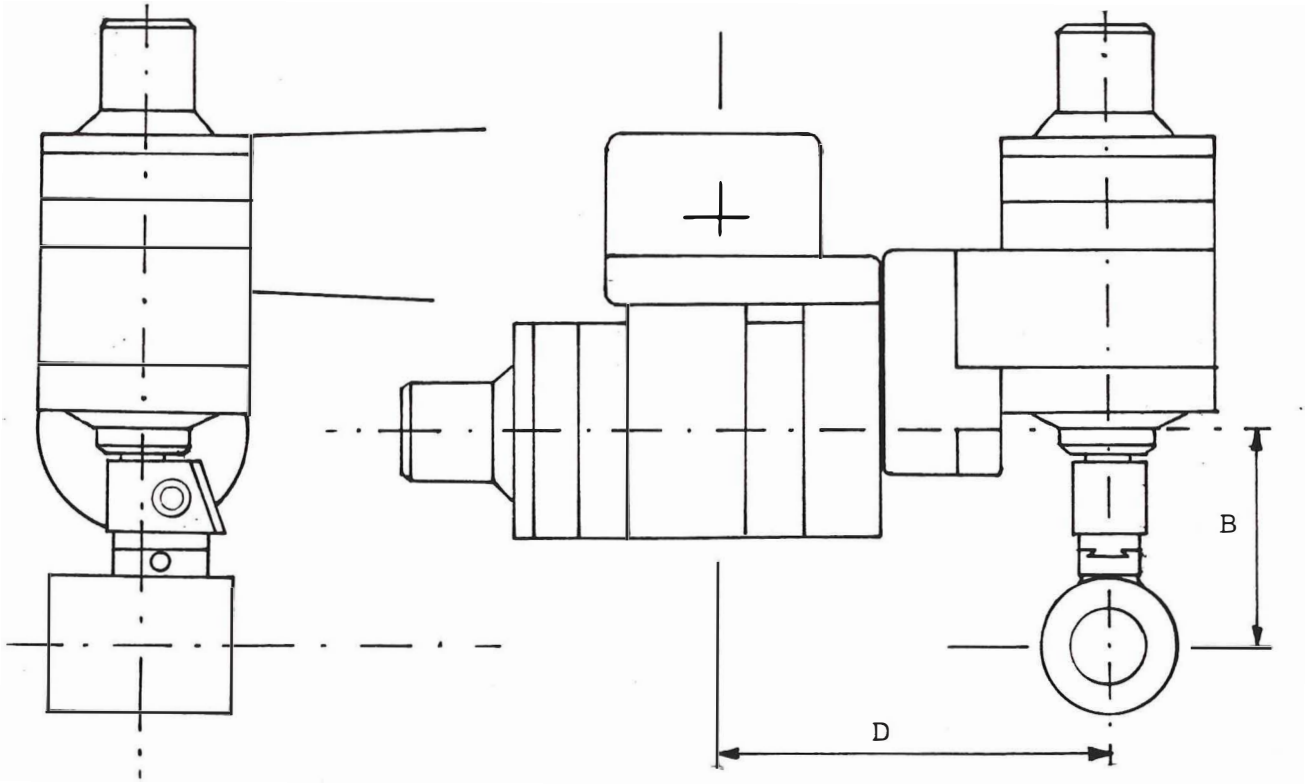

Figure A1.2. Placement of the positional deviation sensor.

$$R_3 = \begin{bmatrix} c_1 & 0 & s_1 \\ 0 & 1 & 0 \\ -s_1 & 0 & c_1 \end{bmatrix} \begin{bmatrix} 1 & 0 & 0 \\ 0 & c_3 & -s_3 \\ 0 & s_3 & c_3 \end{bmatrix} = \begin{bmatrix} c_1 & s_1 s_3 & s_1 c_3 \\ 0 & c_3 & s_3 \\ -s_1 & c_1 s_3 & c_1 c_3 \end{bmatrix} \quad \text{(A1.2)}$$

and

$$p_3 = \begin{bmatrix} c_1 & 0 & s_1 \\ 0 & 1 & 0 \\ -s_1 & 0 & c_1 \end{bmatrix} \begin{bmatrix} D \\ a_2 c_2 - a_3 s_3 \\ a_2 s_2 + a_3 c_3 \end{bmatrix} \quad \text{(A1.3)}$$

A virtual displacement ${}^3\underline{v}_3$ of system 3, in system 3 coordinates, is then related to joint displacements $\Delta\underline{e}_3 = [e_1, e_2, e_3]^T$ by

$$\begin{aligned} v_1 &= (a_2 s_2 + a_3 c_3)\Delta e_1 \\ v_2 &= -a_2 s_{23}\Delta e_2 - a_3 \Delta e_3 \\ v_3 &= a_2 c_{23}\Delta e_2 \end{aligned} \quad \text{(A1.4)}$$

where $s_{23} = \sin(e_2 - e_3)$ and $c_{23} = \cos(e_2 - e_3)$. Solving for joint displacements,

$$\begin{aligned} \Delta e_1 &= \frac{1}{a_2 s_2 + a_3 c_3} v_1 \\ \Delta e_2 &= \frac{1}{a_2 c_{23}} v_3 \\ \Delta e_3 &= -\frac{1}{a_3} v_2 - \frac{s_{23}}{a_3 c_{23}} v_3 \end{aligned} \quad \text{(A1.5)}$$

Equations (A1.4) and (A1.5) may of course be given in matrix notation by

$${}^3\underline{v}_3 = J_{e3}\,\Delta\underline{e}_3 \quad ; \quad \Delta\underline{e}_3 = J_{e3}^{-1}\,{}^3\underline{v}_3$$

Note that, for simplicity, offset D has been neglected in these

expressions. Since $D << a_3$, the resulting error is small.

The computed change in $\underline{e}_3$ leads to a change ${}^3\underline{w}_3$ in the orientation of system 3. This is given by

$$\begin{aligned} w_1 &= \Delta e_3 \\ w_2 &= c_3 \Delta e_1 \\ w_3 &= -s_3 \Delta e_1 \end{aligned} \tag{A1.6}$$

The homogeneous transformation matrix from system 3 to system 5 is

$${}^3H_5 = \begin{bmatrix} & {}^3R_5 & & \underline{0} \\ & & & \\ & \underline{0}^T & & 1 \end{bmatrix} \tag{A1.7}$$

where

$${}^3R_5 = \begin{bmatrix} 1 & 0 & 0 \\ 0 & c_4 & -s_4 \\ 0 & s_4 & c_4 \end{bmatrix} \begin{bmatrix} c_5 & 0 & s_5 \\ 0 & 1 & 0 \\ -s_5 & 0 & c_5 \end{bmatrix} = \begin{bmatrix} c_5 & 0 & s_5 \\ s_4 s_5 & c_4 & -s_4 c_5 \\ -c_4 s_5 & s_4 & c_4 c_5 \end{bmatrix} \tag{A1.8}$$

This means that a vector in system 5, ${}^5\underline{v}$, is represented in system 3 coordinates by

$${}^3\underline{v} = {}^3R_5 \, {}^5\underline{v} \tag{A1.9}$$

Given the deviation vector ${}^T\underline{d} = {}^5\underline{d}$, which represents data from the positional deviation sensor in manipulator (system 5) coordinates,

$$ {}^{T}\underline{d} = \begin{bmatrix} {}^{T}\underline{v} \\ \\ {}^{T}\underline{w} \end{bmatrix} \qquad \text{cf. (2.7)} $$

its representation in system 3 is found by

$$ {}^{3}\underline{v} = {}^{3}R_5 \; {}^{5}\underline{v} \quad ; \quad {}^{3}\underline{w} = {}^{3}R_5 \; {}^{5}\underline{w} \tag{A1.10} $$

Joint displacements corresponding to the positional deviation ${}^{3}\underline{v}$ are then found by (A1.5). Going back, the resulting change in orientation, $\underline{w}_3$, is given by (A1.6). This is further transformed into system 5 coordinates by

$$ {}^{5}\underline{w}_3 = {}^{5}R_3 \; {}^{3}\underline{w}_3 \tag{A1.11} $$

where ${}^{5}R_3$ is the inverse, and hence the transpose of ${}^{3}R_5$. Defining

$$ {}^{5}\bar{\underline{w}} = {}^{5}\underline{w} - {}^{5}\underline{w}_3 \tag{A1.12} $$

angular displacements in joints 4 and 5, corresponding to the deviation vector ${}^{T}\underline{d}$, are given by

$$ \begin{aligned} \Delta\theta_5 &= {}^{5}\bar{w}_2 \\ \Delta\theta_4 &= c_5 \; {}^{5}\bar{w}_1 + s_5 \; {}^{5}\bar{w}_3 \end{aligned} \tag{A1.13} $$

The calculation of joint displacements from the deviation vector ${}^{T}\underline{d}$ may be summarized by

$$ \Delta\underline{\theta} = J_{T\theta} \; {}^{T}\underline{d} \tag{A1.14} $$

where $J_{T\theta}$ often is called the inverse manipulator Jacobian.

A1.2 Sensor coordinates

The positional deviation sensor is fixed to link 5 as shown in Fig. A1.2. Its position in system 5 is generally described by the constant transformation matrix

$$M = \begin{bmatrix} & R_M & & \underline{p}_M \\ & & & \\ & \underline{0}^T & & 1 \end{bmatrix} \qquad \text{(A1.15)}$$

In Section 2, the relationship between displacement in sensor coordinates and manipulator coordinates is given in (2.9) in terms of Δ-matrices by

$$T_\Delta = M \, M_\Delta \, M^{-1} \qquad \text{(A1.16)}$$

where the deltas may be decomposed into

$$T_\Delta = \begin{bmatrix} & T_\Omega & & T_{\underline{v}} \\ & & & \\ & \underline{0}^T & & 0 \end{bmatrix} ; \; M_\Delta = \begin{bmatrix} & M_\Omega & & \underline{p}_3 \\ & & & \\ & \underline{0}^T & & 0 \end{bmatrix} \qquad \text{(A1.17)}$$

Note that the diagonal elements of the Δ-matrices are zero and that the Ω sub-matrices are skew symmetric.

Inserting (A1.15) in (A1.16),

$$T_\Omega = R_M \, M_\Omega \, R_M^T \qquad \text{(A1.18)}$$

$$T_{\underline{v}} = -R_M \, M_\Omega \, R_M^T \, \underline{p}_M + R_M \, M_{\underline{v}} \qquad \text{(A1.19)}$$

In the present case, by Fig. A1.2, matrix M is given by

$$R_M = I \quad ; \quad \underline{p}_M = [0, -B, 0]^T \tag{A1.20}$$

so (A1.18) and (A1.19) are reduced to

$$T_\Omega = {}^M\Omega \tag{A1.21}$$

$$T_{\underline{v}} = -{}^M\Omega \, \underline{p}_M + {}^M\underline{v} \tag{A1.22}$$

Noting the relationship between Ω matrix notation and the rotational deviation vector $\underline{w}$,

$$\Omega = \begin{bmatrix} 0 & -\delta_3 & \delta_2 \\ \delta_3 & 0 & -\delta_1 \\ -\delta_2 & \delta_1 & 0 \end{bmatrix} \quad ; \quad \underline{w} = \begin{bmatrix} \delta_1 \\ \delta_2 \\ \delta_3 \end{bmatrix} \tag{A1.23}$$

(A1.21) and (A1.22) finally yields

$$T_{\underline{d}} = \begin{bmatrix} T_{\underline{v}} \\ \\ T_{\underline{w}} \end{bmatrix} = \begin{bmatrix} I & \tilde{B} \\ \\ 0 & I \end{bmatrix} \begin{bmatrix} {}^M\underline{v} \\ \\ {}^M\underline{w} \end{bmatrix} = J_{MT} \, {}^M\underline{d} \tag{A1.24}$$

where

$$\tilde{B} = \begin{bmatrix} 0 & 0 & -B \\ 0 & 0 & 0 \\ B & 0 & 0 \end{bmatrix}$$

The complete transformation of sensor data, ${}^M\underline{d}$, into equivalent joint displacements, $\underline{e}$, is now obtained by applying (A1.24) and then the procedure corresponding to (A1.14).

A1.3 Constants

For the manipulator at hand, the kinematic constants in Figs. A1.1 and A1.2 have the values

$a_2 = 0.8$ m

$a_3 = 1.6$ m

$D = 0.17$ m

$B = 0.11$ m

The accuracy of these is sufficient for use in differential transformations. For the computation of absolute position however, more accurate values are needed.

A2. INERTIA AND STIFFNESS COEFFICIENTS

As stated in Section 7.1, the parameters of the equations of motion depend on the mass and stiffness distribution of links 2 and 3. Since link 2 in Section 7.1 is considered rigid, the corresponding parameters are easily obtained, Section A2.3. For link 3 however, more detailed computations are needed. These are carried out below. Afterwards, calculation of the inertia matrix (7.16) is carried out, and some notes on its inversion are given.

A2.1 Link 3

Refering to Fig. A2.1, link 3 is assumed to consist of lumped masses m_i and m_t respectively at the inner end and the tip of the beam. The remaining mass is distributed. The total mass distribution function is assumed to be

$$\mu(r) = m_i\delta(0) + [\mu_0 - \frac{\mu_0 - \mu_a}{a_3}] + m_t\,\delta(a_3) \qquad \text{(A2.1)}$$

where $\delta(\ )$ is the unit impulse function, whereas $\mu_0 = \mu(0^+)$ and $\mu_a = \mu(a_3^-)$. Introducing $\varrho = r/a_3$ and $\mu' = \mu_a/\mu_0$, this may be

$$\mu(r) = m_i\delta(0) + \mu_0[1 - (1-\mu')\varrho] + m_t\delta(a_3) \qquad \text{(A2.2)}$$

which implies, cf. (7.4),

$$i(r) = \frac{m_i}{m_3}\,\delta(0) + \frac{\mu_0}{m_3}\,[1 - (1-\mu')\varrho] + \frac{m_t}{m_3}\,\delta(a_3) \qquad \text{(A2.3)}$$

Beam deflection depends on the stiffness distribution, which again depends on the area moment of inertia, I(r), of the link. The beam cross section is assumed rectangular with measures B and H, formed by sheet metal of thickness Δ. Considering up-down bending

only,

$$I(r) = \frac{1}{2} H^2(r)B(r)\Delta \tag{A2.4}$$

where, since H and B by Fig. A2.1 may be assumed linear in r,

$$H(r) = H_0[1-(1-h)]\varrho \; ; \; B(\varrho) = B_0[1-(1-b)]\varrho$$

where again $H_0 = H(0)$, $h = H(a_3)/H(0)$ and $\varrho = r/a_3$. Similarly, $B_0 = B(0)$ and $b = B(a)/B(0)$. Expansion of (A2.4) yields

$$I(r) = \frac{H_0^2 B_0 \Delta}{2} \{1-[2(1-h)+(1-b)]\varrho + [(1-h)^2 + 2(1-h)(1-b)]\varrho^2 - (1-h)^2(1-b)\varrho^3\} \tag{A2.5}$$

With proper values for b and h inserted, (A2.5) is in Fig. A2.2 compared with the approximation

$$I(r) \approx \frac{H_0^2 B_0 \Delta}{2} (1 - \varrho) \tag{A2.6}$$

Adopting this, and assuming moment distribution

$$M(r) = \tau_2(1 - \varrho) \tag{A2.7}$$

where τ_2 is the torque at joint 3, beam deflection is given by

$$\frac{\partial^2 u}{\partial r^2} = \frac{M(r)}{EI(r)} = \frac{2\tau_2}{E\, H_0^2 B_0 \Delta} \tag{A2.8}$$

By integration,

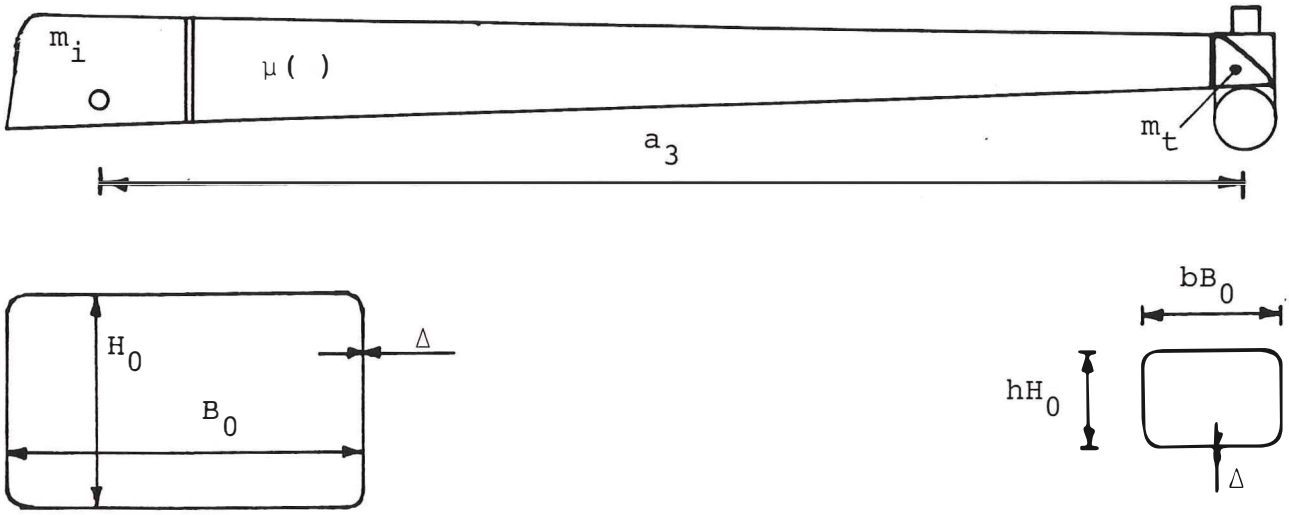

Figure A2.1. Link 3 of the TR 400. Mechanical outline including cross sections at both ends.

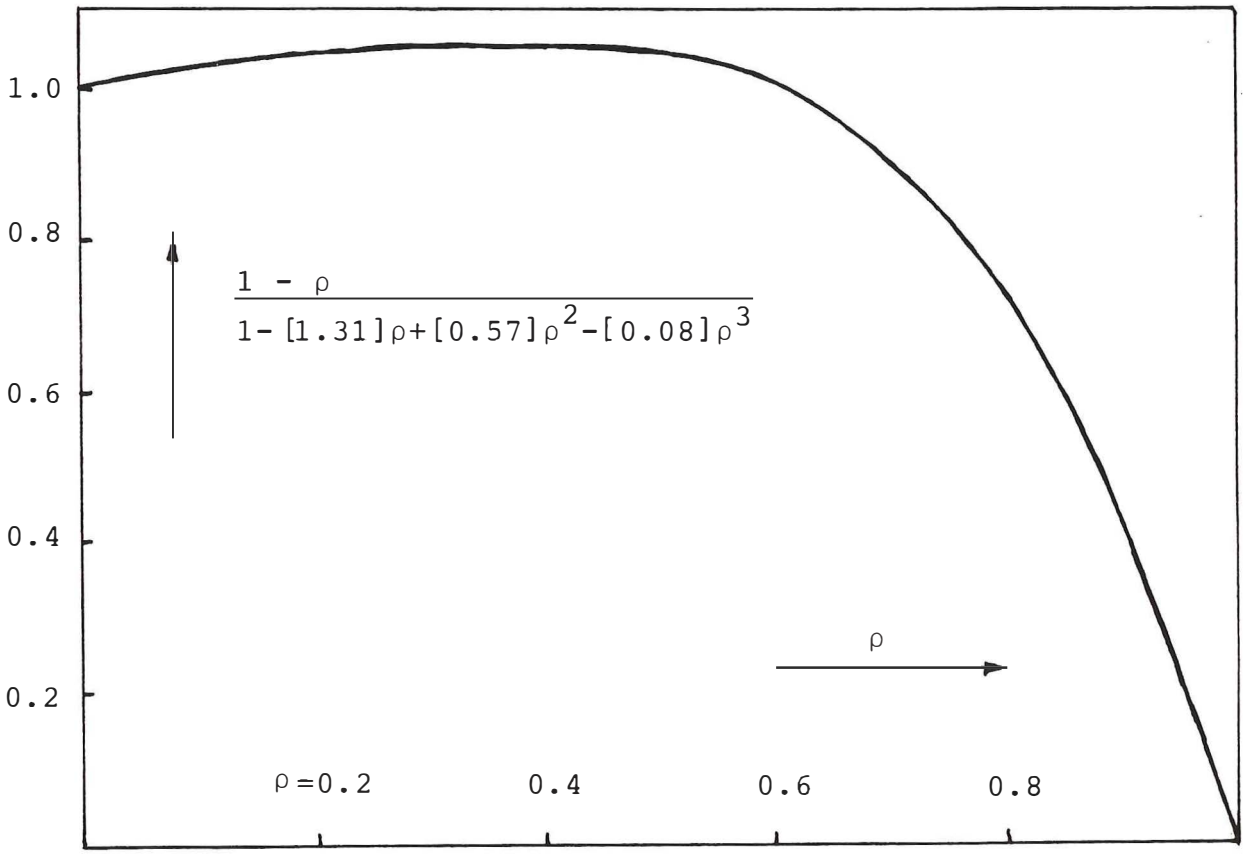

Figure A2.2. Ratio between Eqs. (A2.6) and (A2.5). This is close to unity for large parts of the link. Hence, (A2.6) will be used instead of (A2.5) in order to avoid complicated results.

$$\frac{\partial u}{\partial r} = \frac{2\tau_2}{EH_0^2 B_0 \Delta} r + c_1 \tag{A2.9}$$

$$u(r) = \frac{\tau_2}{EH_0^2 B_0 \Delta} r^2 + c_1 r + c_0 \tag{A2.10}$$

where, knowing that $u(0) = 0$, $c_0 = 0$. Constant c_1 is found by (7.6). Due to the mass distribution (A2.2), which includes a large lumped mass m_t at $r = a_3$ it is seen that when (7.6) is is satisfied,

$$u(a_3) \approx 0 \tag{A2.11}$$

By (A2.10), this implies

$$c_1 = - \frac{a_3 \tau_2}{E H_0^2 B \Delta} \tag{A2.12}$$

Inserting this into (A2.9), and recalling the definition of generalized coordinate q_3,

$$q_3 = - \frac{\partial u}{\partial r}(0) = -c_1 = \frac{a_3}{EH_0^2 B \Delta} \tau_2 = \frac{1}{k_s} \tau_2 \tag{A2.13}$$

Here k_s denotes the stiffness of link 3. The orientational change at the link tip results by setting $r = a_3$.

$$ {}^{3}\delta_1 = \frac{\partial u}{\partial r}(a_3) = -\frac{a_3}{EH_0^2 B\Delta}\tau_2 = -\frac{1}{k_s}\tau_2 \qquad \text{(A2.14)} $$

A2.2 Constants

LINK 2

Beam length: $a_2 = 0.8$ m

Center of gravity: $\bar{r} = 0.34$ m (from joint 2)

Moment of inertia: $J_{\bar{r}} = 2$ kgm^2

Total mass: $m_2 = 13$ kg

From this, the moment of inertia about joint 2 is

$$ J_1' = J_{\bar{r}} + m_2\bar{r}^2 = 3.5 \text{ kg m}^2 $$

LINK 3

Beam length: $a_3 = 1.6$ m

Total mass: $m_3 = 28.5$ kg

Inner lumped mass: $m_i = 13$ kg

Outer lumped mass: $m_t = 10$ kg

Mass distribution: $\mu_0 = 5$ kg/m ; $\mu' = 0.4$

Link cross section height: $H_0 = 0.14$ m ; $h = 0.464$

Link cross section width: $B_0 = 0.235$ m ; $b = 0.383$

Sheet thickness: $\Delta = 2.5\ 10^{-3}$ m

Youngs modulus (aluminium): $E = 70\ 10^{9}$ N/m^2

Total stiffness by (A2.13): $k_s = 500\ 10^{3}$ Nm/rad

A2.3 Inertia matrix

By (7.15), the inertia terms depend on the integrals

$$B = \int_0^{a_3} i(r) r\, dr \quad ; \quad D = \int_0^{a_3} i(r)\beta(r)dr$$

$$R^2 = \int_0^{a_3} i(r) r^2 dr \quad ; \quad B^2 = \int_0^{a_3} i(r)\beta^2(r)dr$$

Inserting the values given in Section A2.3 into (A2.3) results in

$$i(r) = 0.456\ \delta(0) + 0.175[1-0.6\ \frac{r}{a_3}] + 0.351\ \delta(a_3)$$

Multiplication by r and r^2 and integration yields the link 2 center of mass and squared inertial radius respectively,

$$b = 0.52\ a_3^2 + 0.351\ a_3 = 0.696 \text{ m}$$

$$R^2 = 0.32\ a_3^3 + 0.351\ a_3^2 = 1.03\ m_3^2$$

Equation (7.1) defines $\beta(r) = u(r)/q_3$ which by (A2.10) and (A2.13) implies

$$\beta(r) = -\frac{1}{a_3} r^2 + r$$

$$\beta^2(r) = \frac{1}{a_3^2} r^4 - \frac{2}{a_3} r^3 + r^2 \qquad \text{(A2.15)}$$

Multiplication by i(r) and integration yields

$$D = 0.020\ a_3^2 = 0.052\ m$$

$$B^2 = 0.004\ a_3^3 = 0.017\ m^2$$

Inertias are now found by (7.15):

$$J_1 = m_3\ a_2^2 + J_1' = 21.7\ kg\ m^2$$

$$J_2 = m_3 R^2 = 29.4\ kg\ m^2$$

$$J_3 = m_3 B^2 = 0.485\ kg\ m^2$$

$$J_{12} = m_3 a_1 b = 15.9\ kg\ m^2$$

$$J_{13} = m_3 a_1 D = 1.19\ kg\ m^2$$

Considering the different orders of magnitude of these elements, simplifications can be made when inverting (7.25). The inverse of the matrix

$$A = \begin{bmatrix} a_1 & a_{12} & a_{13} \\ a_{12} & a_2 & 0 \\ a_{13} & 0 & a_3 \end{bmatrix}$$

is given symbolically by

$$A^{-1} = (a_1 a_2 a_3 - a_{12}^2 a_3 - a_2 a_{13}^2)^{-1}$$

$$* \begin{bmatrix} a_2 a_3 & -a_{12} a_3 & -a_{13} a_2 \\ -a_{12} a_3 & a_1 a_3 - a_{13}^2 & a_{12} a_{13} \\ -a_{13} a_2 & a_{12} a_{13} & a_1 a_2 - a_{12}^2 \end{bmatrix} \qquad \text{(A2.16)}$$

Considering the order of magnitude of its elements, the inverse of $M(\varphi)$ can be approximated by

$$N = [J_3 (J_1 J_2 - J_{12}^2 \sin^2\varphi)]^{-1}$$

$$* \begin{bmatrix} J_2 J_3 & -J_{12} J_3 \sin\varphi & -J_{13} J_2 \sin\varphi \\ -J_{12} J_3 \sin\varphi & J_1 J_3 & J_{12} J_{13} \sin^2\varphi \\ -J_{13} J_2 \sin\varphi & J_{12} J_{13} \sin^2\varphi & J_1 J_2 - J_{12}^2 \sin^2\varphi \end{bmatrix} \qquad \text{(A2.17)}$$

It is seen that element n_3 of N is much larger than the others, which gives rise to the simplifications resulting in (7.25) and (7.26). Since also assumption (7.27) seems to hold, (7.28) and (7.29) are applicable as well. The 2x2 matrix of (7.28) can

by (A2.17) be approximated by

$$\begin{bmatrix} n_1 & n_{12} \\ n_{12} & n_2 \end{bmatrix} = (J\,J - J^2 \sin^2\varphi)^{-1} \begin{bmatrix} J_2 & -J_{12}\sin\varphi \\ -J_{12}\sin\varphi & J_1 \end{bmatrix} \quad \text{(A2.18)}$$

which is the inverse of the upper left 2x2 block of $M(\varphi)$.

A3. HYDRAULIC ACTUATOR

The joints of the TR400 are driven hydraulically. Joints 1, 4 and 5 by single vane, limited rotational actuators and joints 2 and 3 by translational cylinders. Since, in Section 7, the analysis is restricted to the latter two joints, this will be the case in this appendix as well.

A3.1 Translational actuator

Separate mass balances for the hydraulic cylinder in Fig. 7.2 are, for chamber 1

$$\dot{p}_1 \frac{V_1}{\beta} + \dot{V}_1 = q_1 - q_\lambda \qquad \text{(A3.1)}$$

and for chamber 2

$$\dot{p}_2 \frac{V_2}{\beta} + \dot{V}_2 = -q_2 + q_\lambda \qquad \text{(A3.2)}$$

Here p_i denotes pressure, V_i chamber volume, q_i valve port flow and q_λ leakage. Bulk modulus (inverse compressibility) is denoted by β. Chamber volumes as functions of linear translation are

$$V_1 = A(\frac{L}{2} + d_c) \; ; \; V_2 = A(\frac{L}{2} - d_c) \qquad \text{(A3.3)}$$

where A denotes the cylinder cross section area, and $LA = v_1 + v_2$. The time derivatives are

$$\dot{V}_1 = A\dot{d}_c \; ; \; \dot{V}_2 = -A\dot{d}_c = -\dot{V}_1 \qquad \text{(A3.4)}$$

Turning to the right sides of (A3.1) and (A3.2), leakage is equal for both chambers and considered proportional to the pressure

difference.

$$q_\lambda = k_\lambda (p_1 - p_2) \tag{A3.5}$$

Assuming equal valve port flows as well,

$$q_1 = q_2 = q \tag{A3.6}$$

At the moment, q may be considered as a preliminary system control value. Inserting (A3.3) through (A3.6) into (A3.1) and (A3.2),

$$\dot{p}_1 \frac{A(\frac{L}{2} + d_c)}{\beta} + A\dot{d}_c = q - k_\lambda (p_1 - p_2) \tag{A3.7}$$

and

$$\dot{p}_2 \frac{A(\frac{1}{2} - d_c)}{\beta} - A\dot{d}_c = -q + k_\lambda (p_1 - p_2) \tag{A3.8}$$

are obtained. Since the mechanical friction of the TR400 servos is very low, it may be neglected. Thus, the piston force is given by

$$f = A(p_1 - p_2) \tag{A3.9}$$

subtraction of (A3.8) from (A3.7) and division by two yields

$$\dot{f} \frac{L}{4\beta} + (\dot{p}_1 + \dot{p}_2) \frac{Ad_c}{2\beta} + A\dot{d}_c = q - \frac{k_\lambda}{A} f \tag{A3.10}$$

Adding the same equations yields

$$(\dot{p}_1 + \dot{p}_2) \frac{Ad_c}{2\beta} = -(\dot{p}_1 - \dot{p}_2) \frac{Ad_c^2}{\beta L}$$

which inserted into (A2.10) results in

$$(\frac{L}{4\beta} - \frac{d_c^2}{\beta L}) \dot{f} = -\frac{k_\lambda}{A} f - A\dot{d}_c + q \tag{A3.11}$$

Finally, linearization about the fixed displacement d_0 yields

$$\dot{f} = -\frac{k_\lambda k_c}{A} f - Ak_c\dot{d} + k_c q \tag{A3.12}$$

where $d = d_c - d_0$ and

$$k_c = \left(\frac{L}{4\beta} - \frac{d_0^2}{\beta L}\right)^{-1} = \frac{4\beta}{L}\left(1 - 4\frac{d_0^2}{L^2}\right)^{-1} \tag{A3.13}$$

Variables f and d of (A3.12) will now be replaced by the joint-space variables τ and θ. By Fig. 7.2, linearization about $d_0 = a\sin\theta_0$ yields

$$\begin{aligned} d &= \theta\, a\cos\theta_0 \\ \tau &= f\, a\cos\theta_0 \end{aligned} \tag{A3.14}$$

Assuming $\dot{\theta}_0 = 0$, and inserting into (A3.12),

$$\begin{aligned} \dot{\tau} &= \frac{k_\lambda k_c}{A}\tau - Ak_c a^2\cos^2\theta_0\,\dot{\theta} + k_c a\cos\theta_0\, q \\ \dot{\tau} &= -k_t(\theta_0)\tau - k_h(\theta_0)\dot{\theta} + k_q(\theta_0)q \end{aligned} \tag{A3.15}$$

Plots of all coefficients as functions of θ_0 are shown in Fig. A3.1. The fact that the underlying leakage and bulk modulus constants are difficult to determine exactly, diffuses the model. Usually the θ_0-dependence in (A3.15) is neglected as well. Due to this, the control system must be made robust with respect to these parameters.

A3.2 Control valve

Except for assumption (A3.6), the characteristics of the control valve has not yet been considered. The flow depends on the valve opening and on the pressures. The valve in Fig. A3.2 has a positive valued spool position, and

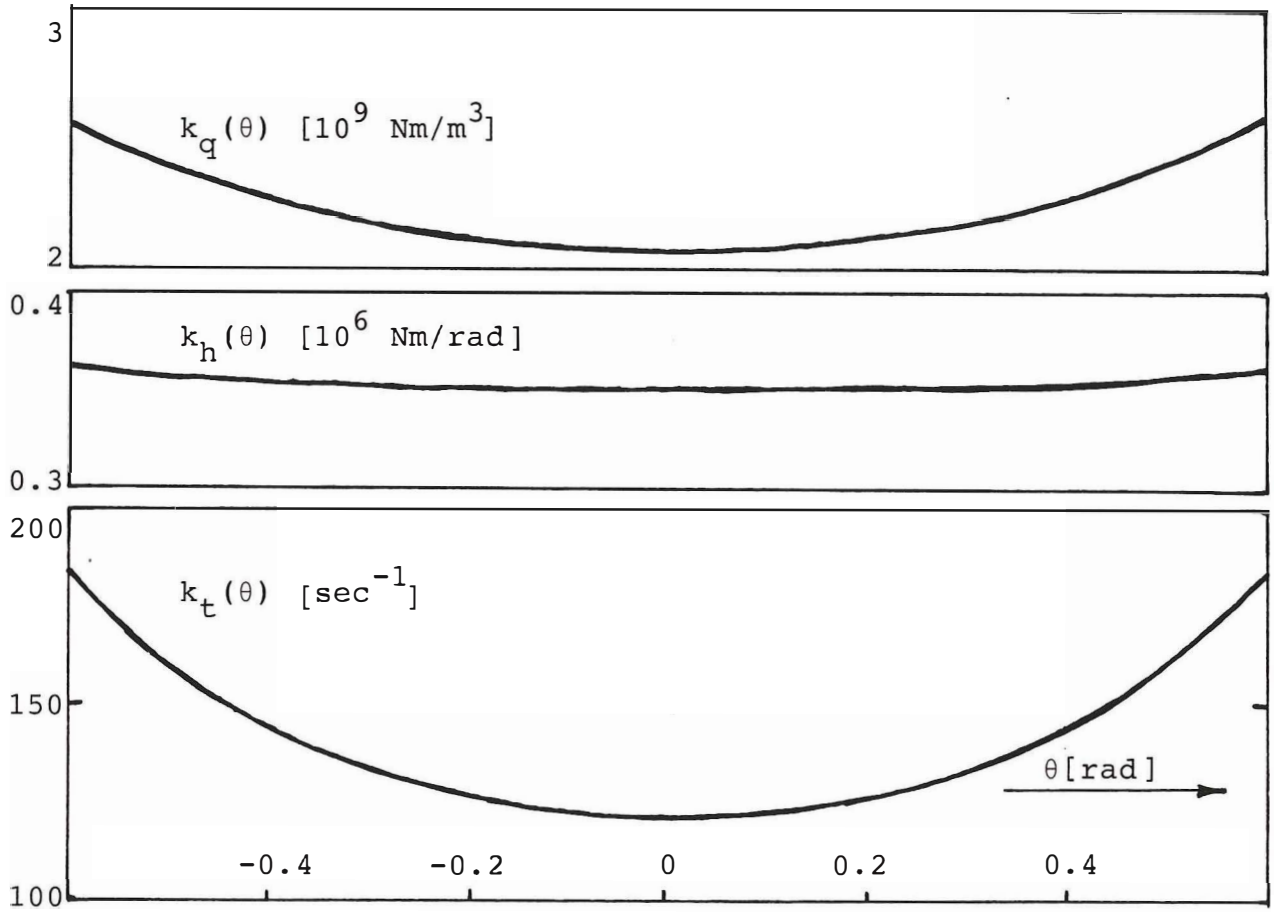

Figure A3.1. Plots of coefficients k_q, k_h and k_t as functions of angular displacement.

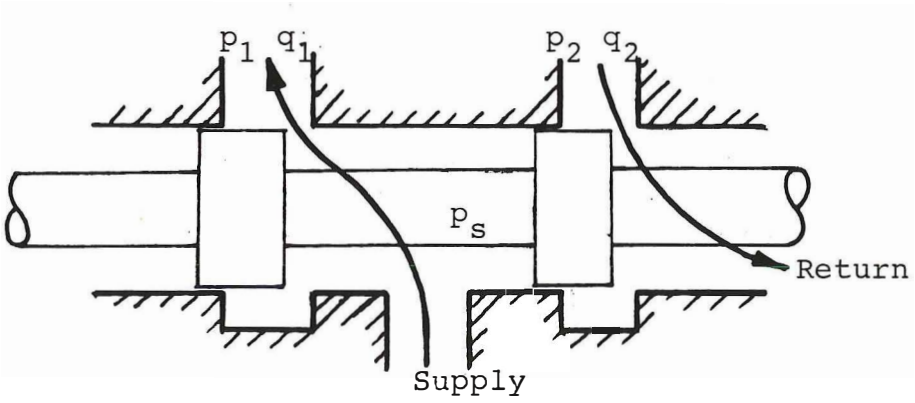

Figure A3.2. 4-way spool valve.

$$q_1 = c(p_s - p_1)^{1/2} \quad ; \quad q_2 = c(p_2)^{1/2} \tag{A3.16}$$

A negative valued position will give

$$q_1 = c(p_1)^{1/2} \quad ; \quad q_2 = c(p_s - p_2)^{1/2} \tag{A3.17}$$

Here c is proportional to the spool position and p_s denotes the supply pressure. Linearization about $p_1 = p_2 = p_s/2$ yields

$$q_1 = c\left(\frac{p_s}{2}\right)^{1/2} - \frac{|c|}{2}\left(\frac{2}{p_s}\right)^{1/2} p_1 \tag{A3.18}$$

$$q_2 = c\left(\frac{p_s}{2}\right)^{1/2} + \frac{|c|}{2}\left(\frac{2}{p_s}\right)^{1/2} p_2 \tag{A3.19}$$

for the positive and negative values of c. It is seen that (A3.6) results if the load dependent terms of (A3.18) and (A3.19) are neglected. By adding the equations and dividing by two,

$$q = \frac{q_1 + q_2}{2} = c\left(\frac{p_s}{2}\right)^{1/2} - \frac{|c|}{2A}\left(\frac{2}{p_s}\right)^{1/2} \tag{A3.20}$$

A glance at (A3.12) and (A3.15) shows that if (A3.20) is inserted, the load dependent term will add to the load dependent terms of these equations. Hence coefficient k_t of (A3.15) becomes even more difficult to determine. Neglecting load dependence, q is proportional to c, which in turn is controlled electrically. Valve flow may now be written

$$q = k_v u \tag{A3.21}$$

or, considering the dynamics of the valve in question,

$$q(s) = k_v(s)u(s) = \frac{k_v}{1 + \left(\frac{s}{\omega_v}\right)^2} u(s) \tag{A3.22}$$

Transfer function $k_v(s)$ is factory designed. Since $\omega_v \sim 1000$ rad/sec, the dynamics will be neglected.

A3.3 Constants

In the present case, the values of the relevant constants are

$$\beta = 1 \text{ GPa}$$

$$L = 0.33 \text{ m}$$

$$A = 10 \text{ cm}^2 = 10^{-3} \text{m}^2$$

$$k_\lambda = 1 \frac{\text{ml/s}}{\text{bar}} = 10^{-11} \frac{\text{m}^3/\text{s}}{\text{Pa}}$$

$$a = 0.17 \text{ m}$$

$$k_v = 20 \text{ 1/min} = 333 \ 10^{-6} \text{ m}^3/\text{s}$$

From this, the following may be computed:

$$\frac{L}{4\beta} = 82.5 \ 10^{-12} \text{ m/Pa} \quad ; \quad \frac{4\beta}{L} = 12 \text{ GPa/m}$$

$$k_t = \frac{k_\lambda k_c}{A} = \frac{4k_\lambda \beta}{AL} \left[1 - 4\left(\frac{a}{L}\right)^2 \sin^2 \theta_0\right]^{-1}$$

where $\frac{4k_\lambda \beta}{AL} = 121 \text{ s}^{-1}$ and $4\left(\frac{a}{L}\right)^2 = 1.0$

$$k_h = Ak_c a^2 \cos^2 \theta_0 = \frac{4\beta \, Aa^2}{L} \left[1 - 4\left(\frac{a}{L}\right)^2 \sin^2 \theta_0\right]^{-1} \cos^2 \theta_0$$

where $\frac{4\beta A a^2}{L} = 0.35 \ 10^6$ Nm/rad

$$k_q = k_c a \cos\theta_0 = \frac{4\beta a}{L} \left[1 - 4\left(\frac{a}{L}\right)^2 \sin^2 \theta_0\right]^{-1} \cos\theta_0$$

where $\frac{4\beta a}{L} = 2.05 \ 10^9 \text{ Nm/m}^3$

These coefficients are plotted in Fig. A3.1. Coefficient k_u of (7.30) in Section 7.2 is given by

$$k_u = k_q k_v = \frac{4\beta a k_v}{L} \left[1 - 4\left(\frac{a}{L}\right)^2 \sin^2 \theta_0\right]^{-1} \cos\theta_0$$

where $\frac{4\beta a k_v}{L} = 683\ 10^3$ Nm/s

A4. EXPERIMENTAL CONTROL SYSTEM

Means for improving the dynamics of the tool tracking system were investigated experimentally at the Norwegian Institute of Technology in July 1988. The experiments were carried out using a specially designed control system hardware. This is outlined below, together with the structure of the control system. Subsequently, some experimental results are presented, with special emphasis on the dynamics of the 3rd servo of the manipulator.

A4.1. System design

The control system is run on a single TMS 32020 signal processor board (Texas, 1986; PC,1986;1987) which fits into the extention bus of an IBM AT. Two adjoint input/output boards are connected to the I/O-bus of the TMS 32020, as shown in Fig. A4.1. The first board serves as an interface to the positional deviation sensor, and allows simultaneous sampling of the measurement vector $\underline{y}$ at a rate of 2 per ms. The data fusion corresponding to (9.25) or (9.29) is carried out by analog computation. The second input/output board contains the interface to the TR400 manipulator. The aquisition of joint displacement values is restricted to 1 element per ms, which for the manipulator at hand implies a 5 ms cycle for updating the Jacobian matrix described in Appendix A1. However, the setting of the control action vector $\underline{u}$, and sampling of the hydraulic pressure of servos 1, 2 and 3 can be carried out simultaneously. Here, a cycle time of 0.5 ms is easily obtained.

The experiments were carried out with an effective sample time of 5 ms. The conversion of the positional deviation measurements $\underline{y}$ into the equivalent joint-space control error vector $\underline{e}$ was done using the sequential scheme

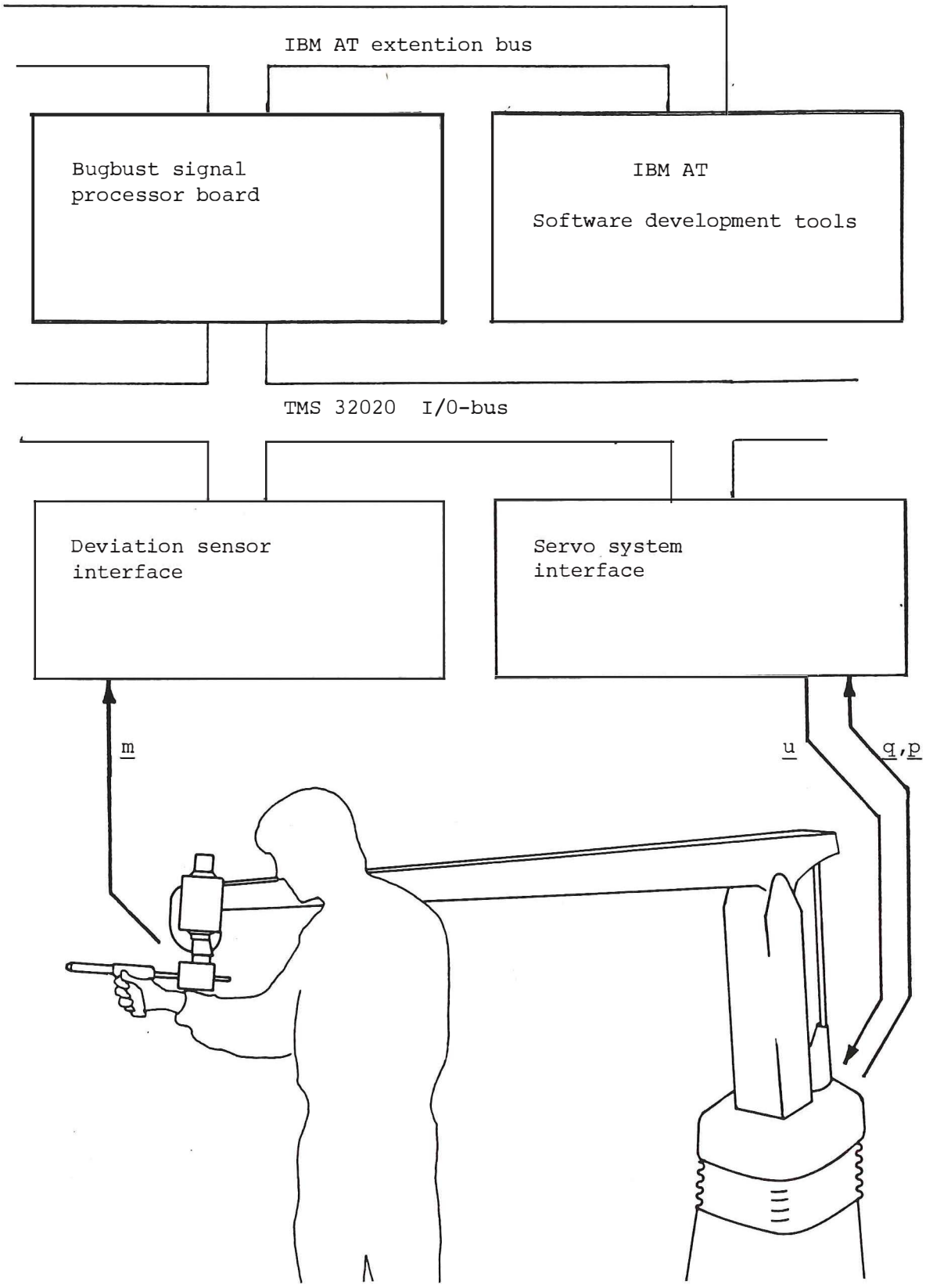

Figure A4.1. Second experimental system. The controller is run on the Bugbust board.

$\underline{y} \longrightarrow \underline{p}$ Appendix A3

$\underline{p} \longrightarrow {}^{M}\underline{d}$ (3.2) and (3.3)

$M_{\underline{d}} \longrightarrow \underline{e}$ Appendix A1

In addition to vector $\underline{e}$, pressure measurements for servos 1, 2 and 3 were made available to the subsequent controllers. The programmed structure of each controller was

$$u(k) = i(k) + c_p e(k) + c_d[e(k)-e(k-1)] + c_t \Delta p(k)$$

$$i(k) = i(k-1) + c_i e(k) \qquad \text{(A4.1)}$$

for servos 1, 2 and 3, and

$$u(k) = c_p e(k) \qquad \text{(A4.2)}$$

for servos 4 and 5.

Linking the constants of (A4.1) to the notation used in Sections 5 and 8, the proportional gain is recognized as

$$k_p = c_p/(5\ \text{ms}\cdot c_d + k_h/k_u) \qquad \text{(A4.3)}$$

where k_h/k_u is the natural velocity feedback reflected by (7.30). Integration constant T_i is given by

$$T_i = 5\ \text{ms}\cdot c_p/c_i \qquad \text{(A4.4)}$$

due to the 5 ms sample time. The torque and velocity feedback constant in (8.4) are found to be

$$g_\tau = c_t/\text{Aacose}_0 \qquad \text{(A4.5)}$$

$$g_v = 5\ \text{ms}\cdot c_d \qquad \text{(A4.6)}$$

respectively, where the values of A and a are found in Section A3.3. In the experiments presented below, e_0 is set to zero, resulting in

$$g_\tau = c_t/(170 \cdot 10^{-6} m^3) \qquad (A4.7)$$

The scope of the investigation was to obtain the best possible results for each of six different sub-structures of controller (A4.1), these being

1. $c_d = c_t = c_i = 0$
2. $c_d = c_t = 0$
3. $c_d = c_i = 0$
4. $c_d = 0$
5. $c_i = 0$
6. all constants nonzero.

In the cases where $c_i = 0$, variable i(k) remains constant and will to some extent compensate the offset of the control valves.

The results presented below concern servo 3 of the TR400. This servo has appeared to be the most difficult one to control, due to the elasticity of link 3, cf. Sections 7 and 8.

A4.2. Some results

The control parameters which from the author's point of view gave the best performance are shown in Table A4.1. For structures 1 trough 4, the parameters reflect a trade-off between stable behaviour and swift tracking. For structures 5 and 6 however, a ceiling was reached while adjusting parameter c_d. This was due to the appearance of significant noise rather than instability. Even

so, the performance of the system when using all the available measurements was outstanding, and is believed to be sufficient for the real-time teaching of high-speed paint-spraying robots.

To compare the performance of the six different controllers in Table A4.1, the step response for each was recorded. The results are shown in Figs. A4.2 through A4.7. The figures give a good indication of the resulting bandwidth for each controller, but are in many respects unfair since the system is not designed to cope with such sudden changes in the tool position. It is characteristic throughout that a tracking controller which is optimal from the point of view of the human operator turns out to be oscillatoric.

Throughout the plots, an oscillatoric mode at approximately 60 rad/sec is observed which is an obvious obstacle to further improvement. The crossing of this barrier will be the scope of future experiments.

Table A4.1. Control parameters for the six sub-structures defined in Section A4.1.

sub-structure number	1	2	3	4	5	6
c_p [rad^{-1}]	1.69	1.69	22.5	22.5	50.6	50.6
c_d [rad^{-1}]	0	0	0	0	144	144
c_t [Pa^{-1}]	0	0	$2.0 \cdot 10^{-6}$	$2.0 \cdot 10^{-6}$	$2.8 \cdot 10^{-6}$	$2.8 \cdot 10^{-6}$
c_i [rad^{-1}]	0	$34 \cdot 10^{-3}$	0	$197 \cdot 10^{-3}$	0	8.43

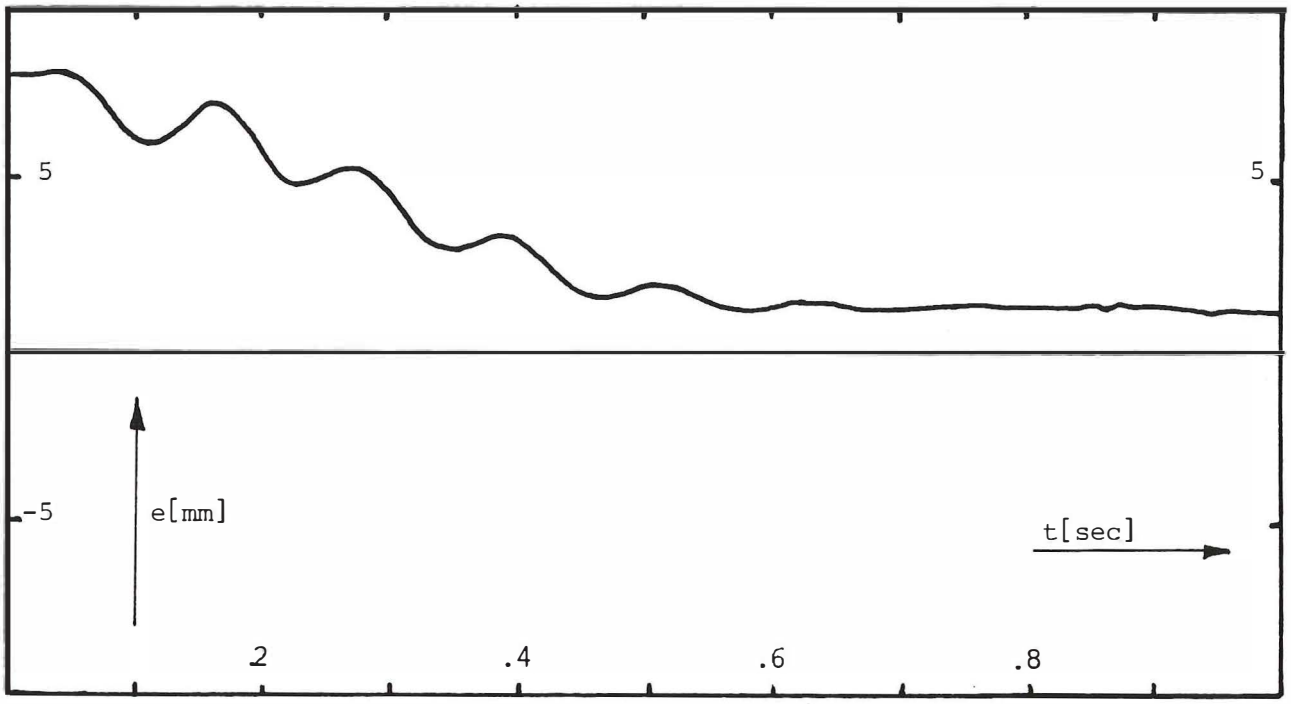

Figure A4.2. Step response of system 1.

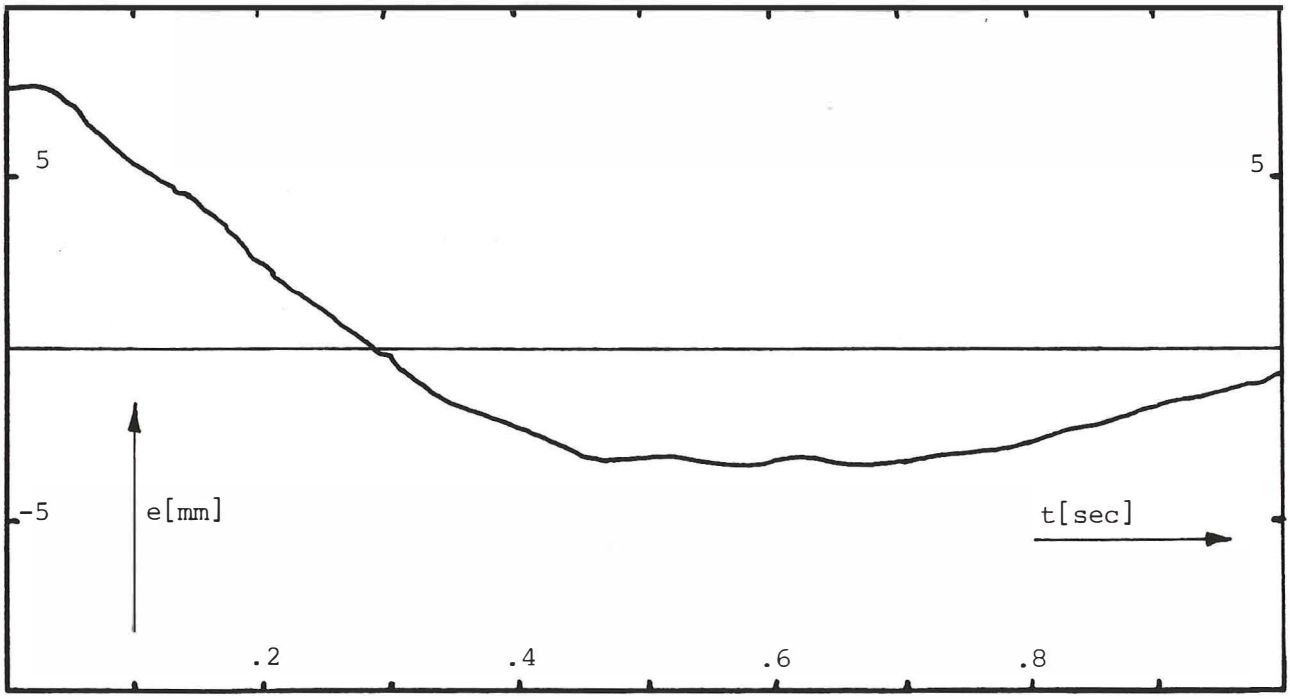

Figure A4.3. Step response of system 2. The oscillation continues for 2 more seconds. The tracking performance however is far better than for system 1.

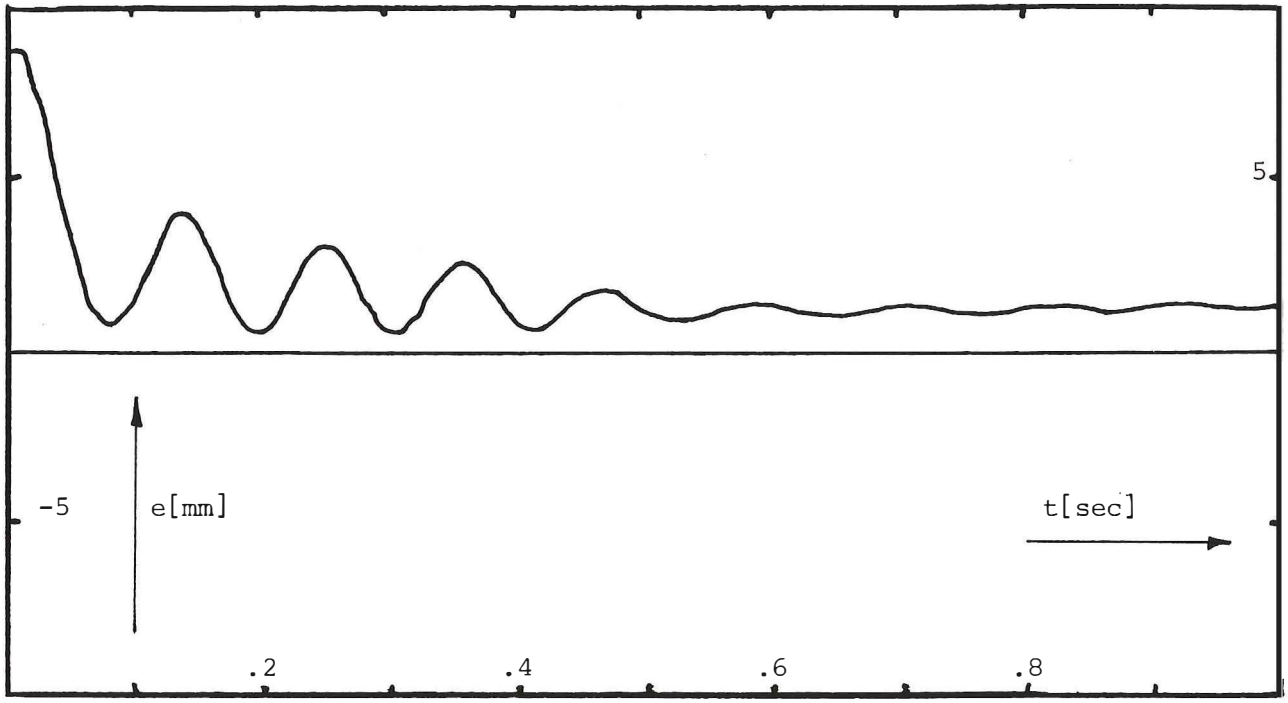

Figure A4.4. Step response of system 3.

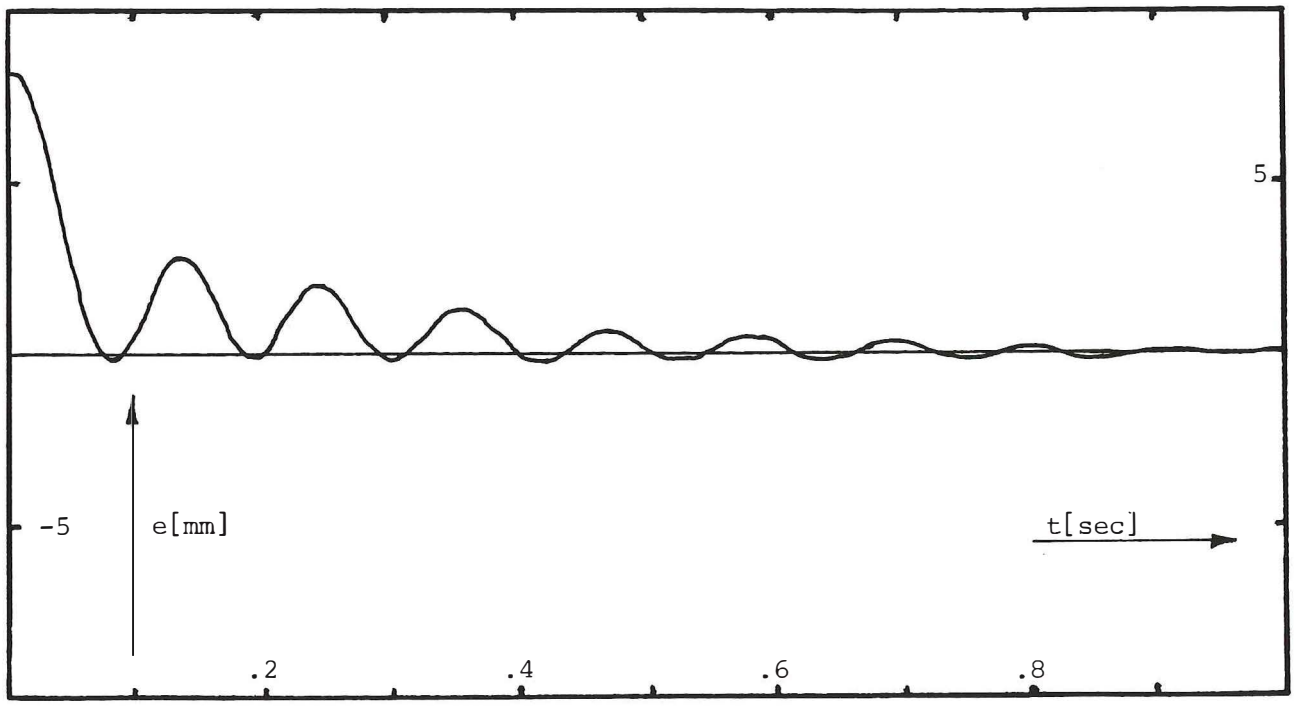

Figure A4.5. Step response of system 4. The integrator was of little use in this case, other than to null out the steady-state error.

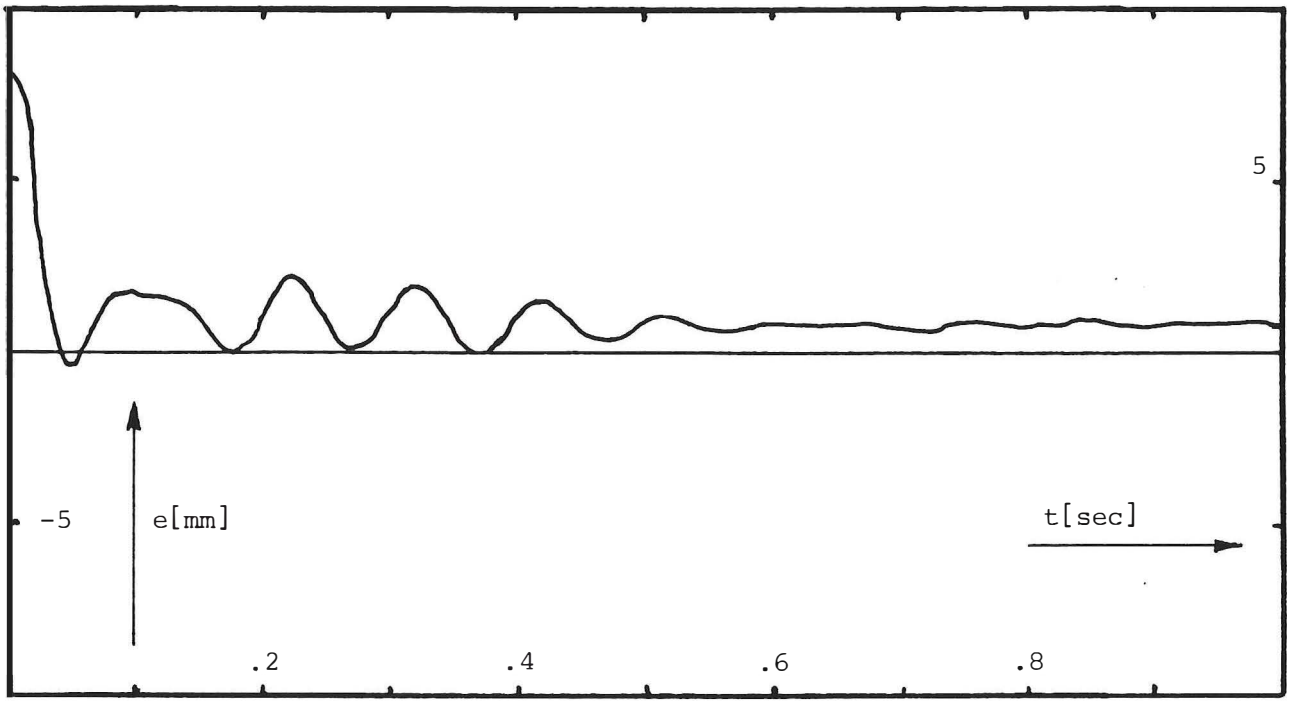

Figure A4.6. Step response of system 5. The bandwidth is greatly improved compared to the previous systems.

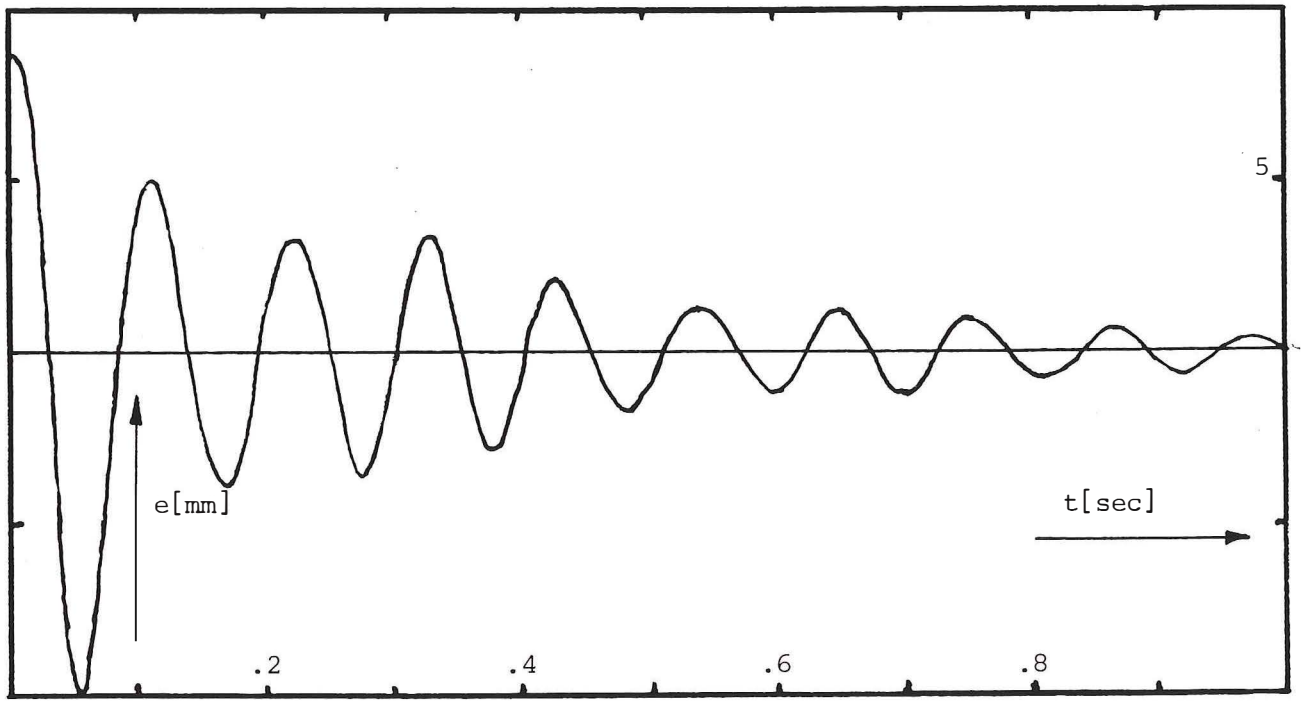

Figure A4.7. Step response of system 6. In spite of the significant oscillations, this is by far the best tracking system.

A5. EXPERIMENTAL DEVIATION SENSOR

In the experiments, a 5-measurements inductive positional deviation sensor is used. Its working principle is described in Section 3.1, whereas the measurement functions are considered theoretically in Section 9. Below, mechanical measures and electrical characteristics are given. Also, calibrational data are presented and subsequently refined.

A5.1 Mechanical outline

The magnetically conductive parts of the sensor are made of common iron. These are shown in Fig. A5.1. From this, the kinematic quantities of the sensor are found:

distance between planes p_1 - p_2 and p_3 - p_4: $b = 66$ mm

inner radius of outer cylinder: $a_1 = 17$ mm

pole length (cf. Section 9.3): $L = 14$ mm

radius of the tool marker: $a_2 = 5$ mm

The position of the magnetizing solenoid is shown in Fig. 3.2. As seen, it fits inside the sensor housing. Characteristic measures are:

mean diameter : 42 mm
number of windings: 6500
wire diameter : 0.23 mm (copper alloy)

The measurement solenoids are placed as shown in Figs. 3.2, 9.2 and 9.5. Two different types of solenoids are used. Solenoids M1

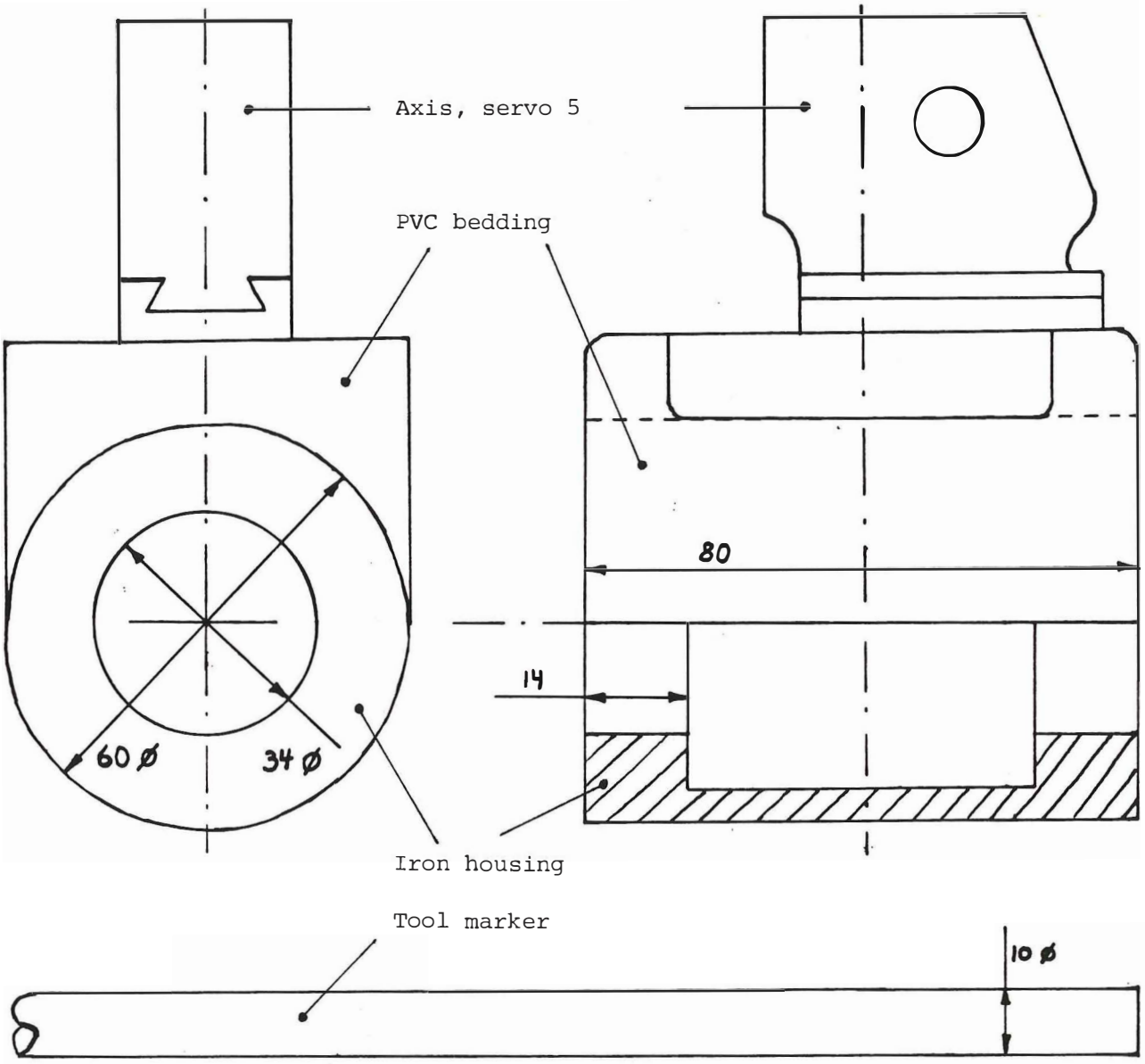

Figure A5.1. Mechanical outline of the sensor.

through M9 have measures:

mean diameter	:	3.5 mm
number of windings:		300
wire diameter	:	0.05 mm (copper alloy)

M9 and M10, which are wound on the tool marker, are (knowing marker radius a_2) described by:

solenoid length	:	S = 40 mm
number of windings:		N = 137
wire diameter	:	0.25 mm

A5.2 Electrical characteristics

The magnetizing solenoid is exited by a 1kHz current source through a 1:20 transformer. Typically, current and voltage from the current source are

I_1 = 190 mA rms

$\hat{u}_2$ = 10 V amplitude

On the secondary side of the transformer, corresponding values are

I_2 = 9 mA rms

$\hat{u}_2$ = 156 V amplitude

In later versions of the sensor, the number of windings of the magnetizing solenoid will be reduced by a factor of 20. In this case, no transformer will be necessary.

Subject to the electrical values given above, the output of the measurement solenoids vary as stated below:

M1 - M8 : 10 - 100 mV

M9 - M10: 0 - 2 V

Polarities are chosen so that all solenoids return positive values. Under normal conditions, the sign (phase) will never change. The induced voltage in solenoids M9 and M10 increase by 5% approx. as eccentricity e is changed from value 0 to 10 mm. This implies similar variations in flux Φ through the tool marker, but does not affect measurement y_5 since (9.34) is applied.

During these tests, approximate measurement functions were obtained by simple means. Using reduction formulas (9.25) and (9.34),

$$y_i \approx \frac{1}{k_r} p_i \qquad \text{for } i = 1...4$$

$$y_5 \approx \frac{1}{k_a} p_5$$

where k_r = 11 mm and k_a = 25 mm. These were used in the preliminary experiments described in Section 5.3.

A5.3 Calibrations

A more thorough investigation of the sensor output was made at Trallfa Robot AS in November 1987. During this, the relative position between the two parts of the sensor was controlled by a 3 d.o.f. positioner with a resolution of 0.01 mm. Throughout the presentation, the position will be given in terms of x_1, x_2 and x_5. These closely correspond to p_1, p_2 and p_5 of Figs. 3.1 and 3.3, but slight differences exist due to misalignments. Measurements investigated were y_1, y_2 and y_5, as generated by reduction formulas (9.25) and (9.34).

At first, the two parts of the sensor were kept parallel. Obtained values of y_1 and y_2 as functions of x_1 and x_2 ($x_5 = 0$) are shown in Table A5.1. From this, Fig. A5.2 results which shows the mapping of constant-x_1 and x_2-lines onto plane y_1-y_2. The figure does not show the expected symmetry which would have been the result if the measurement solenoids were identical and placed accurately. Fact is that solenoid M2 differs from the others due to a nonidentical replacement. For this reason, the subsequent discussion will be based on y_1-measurements only. Synthetic y_2-measurements are then obtained by transposition of the y_1-measurements in Table A5.1. This results in the mapping shown in Fig. A5.3, which still reflects a misalignment between axes x_1 and p_1 estimated to

$$\alpha = 0.06 \text{ radians}$$

Inserting the mechanical data from Section A5.1 into Eqs. (9.28) along with the relative leakage number

$$\frac{a_1}{h_0} = 0.56$$

results in Figs. 9.4 and A5.4. In the latter, misalignment α is taken into account as well. The figure may be compared to Fig. A5.3. In the same way, Tables A5.1 and A5.2 may be compared.

Table A5.1. Measurements y_1 and y_2 for different radial displacements x_1 and x_2. Column no. i in each array represent measurements at x_1 = (i-1) mm. In the same way x_2 = (j-1) mm along row no. j. The two parts of the sensor are kept parallel.

000	080	159	239	319	398	477	555
-02	077	156	235	314	393	470	549
-05	073	150	227	305	381	457	530
-10	066	140	215	289	362	434	503
-13	058	129	200	270	339	404	467
-17	049	115	182	246	309	368	424
-22	039	101	161	219	274	327	
-27	030	084	138	189	238		

$y_1 \cdot 10^3$

000	000	-01	000	001	003	002	005
079	077	074	070	065	062	058	053
156	152	146	139	131	120	113	101
234	228	219	208	193	179	163	146
310	302	291	276	257	236	215	190
384	375	361	341	317	290	263	230
459	447	428	404	377	344	307	
532	517	496	466	431	391		

$y_2 \cdot 10^3$

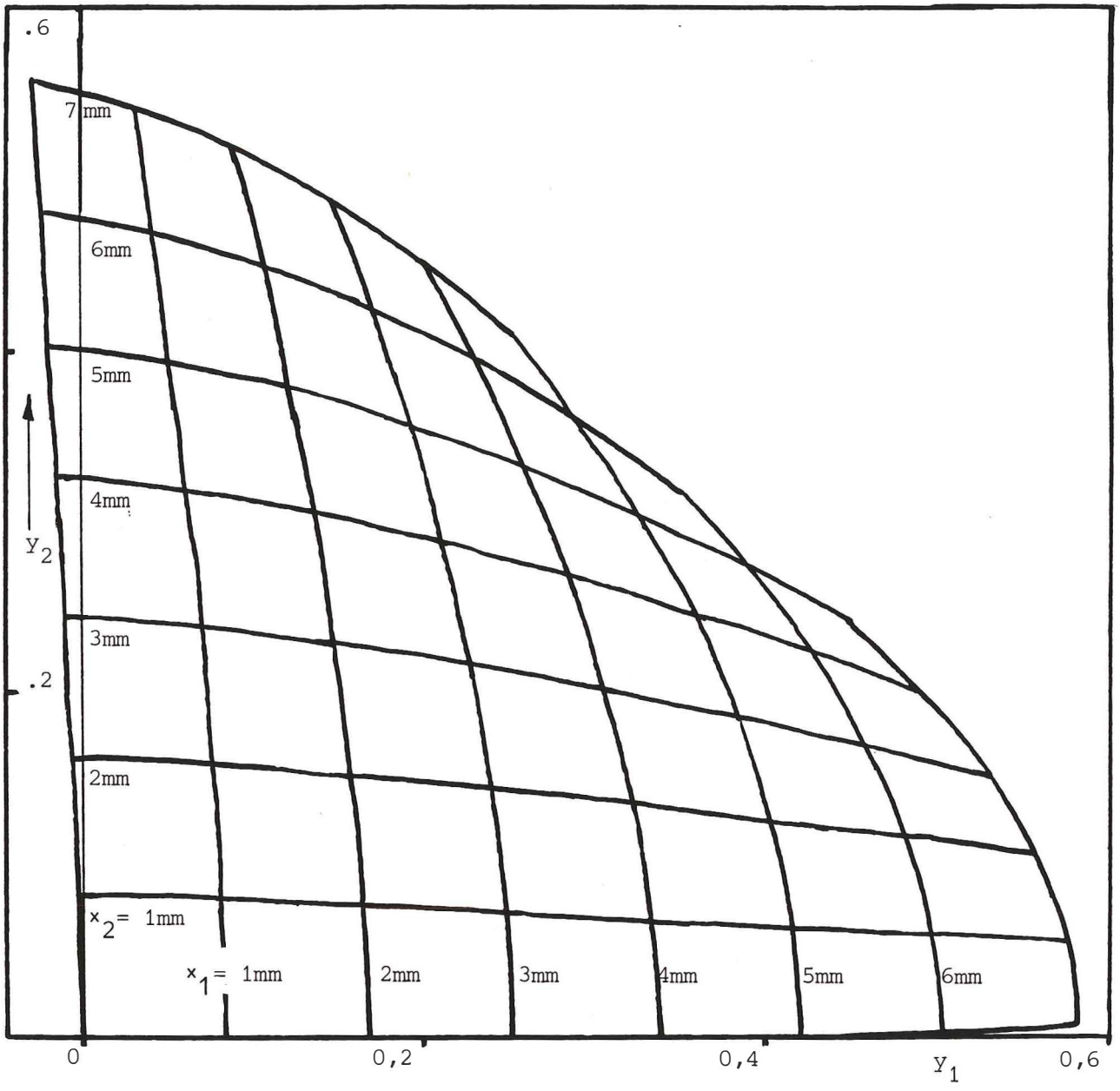

Figure A5.2. Actual radial measurement function. Mapping of constant-x_1 and x_2-lines onto plane y_1-y_2.

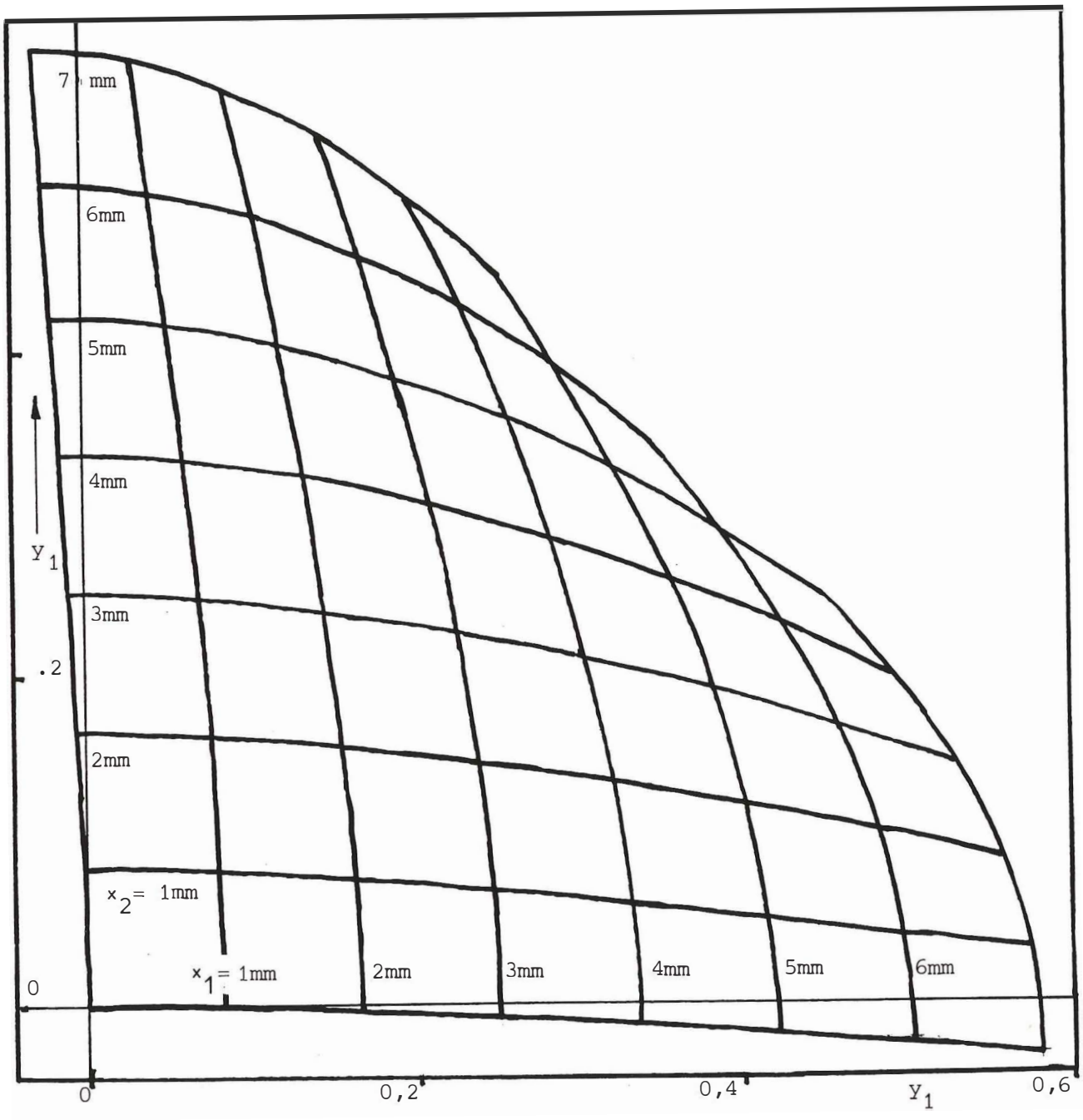

Figure A5.3. Synthetic radial measurement function. This is based on the y_1-measurements only.

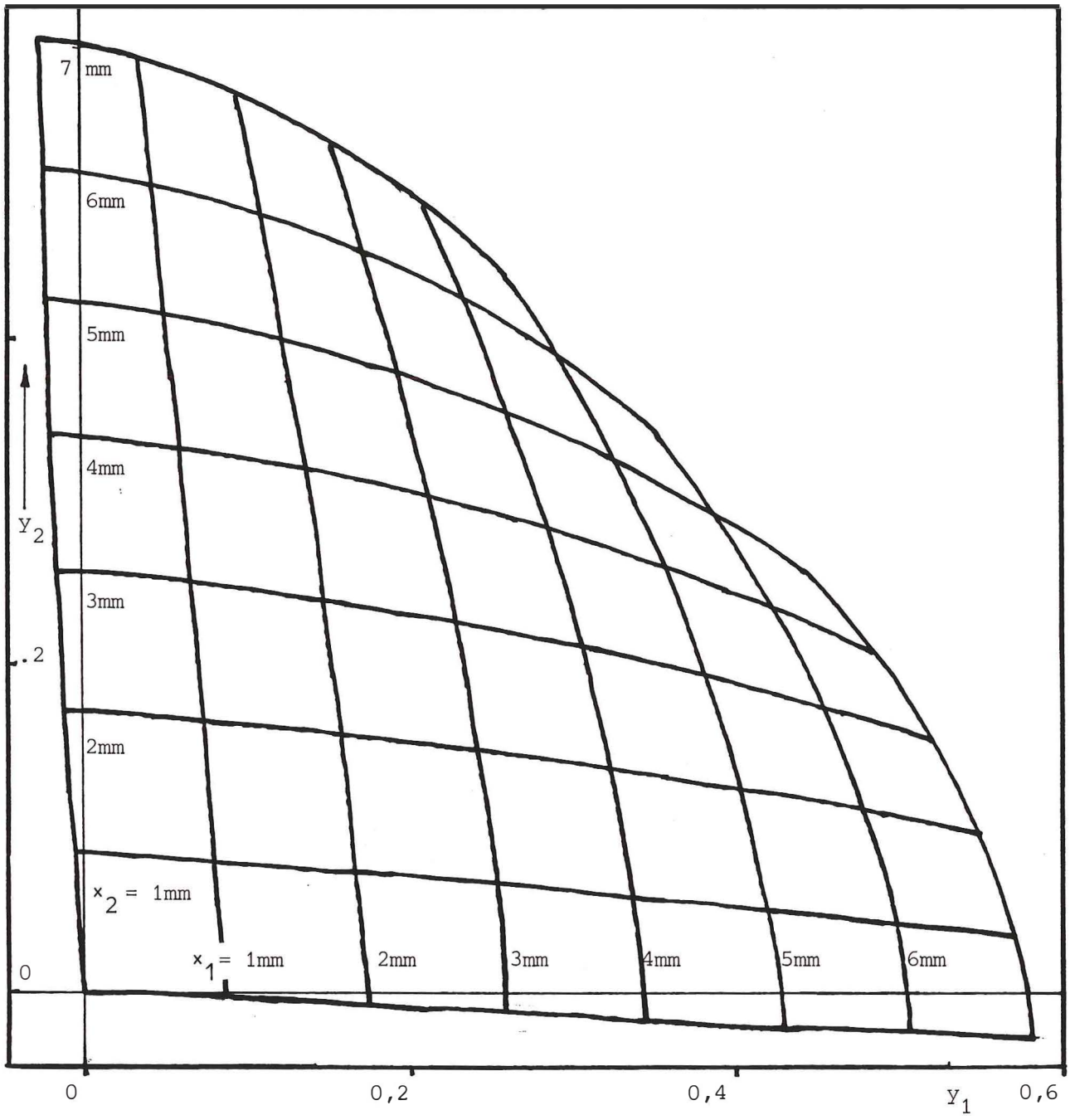

Figure A5.4. Theoretical radial measurement function. Mapping (9.28) with relative leakage factor 0.56. Misalignment α is entered as well. This shows agreement with Fig. A5.3.

Table A5.2. The first array shows computed values of y_1 based on (9.28) with relative leakage 0.56. Measurement y_2 may be obtained by transposition. The second array shfows the difference from Table A5.1.

000	082	164	245	325	404	481	556
-05	077	158	238	317	395	470	543
-10	070	150	228	305	380	452	522
-14	063	140	215	289	360	429	494
-18	056	129	200	270	336	400	459
-21	048	117	183	247	309	366	417
-23	041	104	165	223	278	328	
-25	034	090	145	197	245		

$Y_1 \cdot 10^3$

0	2	5	6	6	6	4	1
-3	0	2	3	3	2	0	-6
-5	3	0	1	0	-1	-5	-8
-4	3	0	0	0	-2	-5	-9
-5	2	0	0	0	-3	-4	-8
-4	1	2	1	1	0	-2	-7
-1	2	3	4	4	4	1	
2	4	6	7	8	7		

x 10^3

Data representing y_5 as a function of x_1 and x_5 are shown in Tables A5.3 and A5.4. The first table shows how y_5 varies for negative x_5 along 3 different values of x_1, whereas the second table shows how it varies for positive x_5 along $x_1 = 0$ and for x_5 along $x_1 = 10$ mm. Some plots of y_5 are shown in Figs. A5.5 and A5.6. In the latter, a second order curve

$$y_5|_{x_5=10} = (0.4 \cdot 10^{-3})x_1^2 - (0.4 \cdot 10^{-3})x_1 + 0.4297$$

fits the data in a least squares sense. Using the substitution

$$p_1 = x_1 - 0.57 \text{ mm} \quad ; \; p_5 = x_5$$

this may be written

$$y_5|_{p_5=10} = (0.4\ 10^{-3})p_1^2 + 0.4296$$

Due to symmetry, the same dependence will be found in the p_2-direction.

Based on Tables A5.3 and A5.4, for $x_1 = 0$ and $-20 \text{ mm} \leq x_5 \leq 20$ mm, least-squares second-order approximations of ratios y_5/x_5 and x_5/y_5 as functions of x_5 and y_5 respectively are

$$\frac{y_5}{x_5}|_{x_1=0} \approx -(23.9 \cdot 10^{-6})x_5^2 + (15.0 \cdot 10^{-6})x_5 + (45.5) \cdot 10^{-3})$$

$$\frac{x_5}{y_5}|_{x_1=0} \approx (11.8)y_5^2 - (26.9 \cdot 10^{-3})y_5 + (21.4)$$

Since the first order terms in these polynomials are small, they can be neglected, resulting in estimates

$$\hat{k}_a = -(24 \cdot 10^{-6})x_5^2 + (45.5 \cdot 10^{-3})$$

$$\hat{k}_a^{-1} = (11.8)y_5^2 + (21.4)$$

Table A5.3. Measurement y_5 for different values of x_1 and x_5. No rotational deviation

$-x_5$ [mm]	$x_1 = 0$	$x_1 = 4$mm	$x_1 = 8$mm
0	000	000	003
1	045		
2	092	094	100
3	136		
4	181		
5	226		
6	270	270	287
7	310		
8	351		
9	390		
10	429	433	456
11	465		
12	500		
13	534		
14	565	570	598
15	594		
16	622		
17	649		
18	672		
19	696		
20	717		
22	755	760	788
24	787		
26	814		
28	836		
30	856	859	878
34	883		
38	902	905	915
42	914		
46	920	922	930

$-y_5 \cdot 10^3$

Table A5.4. Measurement y_5 for different values of x_1 and x_5. No rotational deviation.

$x_1 = 0$

x_5 [mm]	$y_5 \cdot 10^3$
0	000
2	092
6	270
10	430
14	568
18	677
22	762
26	822
30	864
34	894
38	913
42	926
46	933

$x_5 = 10$mm

x_1	$y_5 \cdot 10^3$
-7	453
-6	447
-5	442
-4	438
-3.5	436
-2	432
-1	431
0	430
4	434
8	452

Table A5.5. Measurement y_5 for different values of x_5 at $x_1 = 0$. Rotational deviation $\delta_1 = 0.1$ rad. This may be compared to Table A5.3.

$x_1 = 0$

$-x_5$	$-y_5 \cdot 10^3$
0	000
2	094
6	270
10	432
14	568
22	756
30	856
38	903
46	920

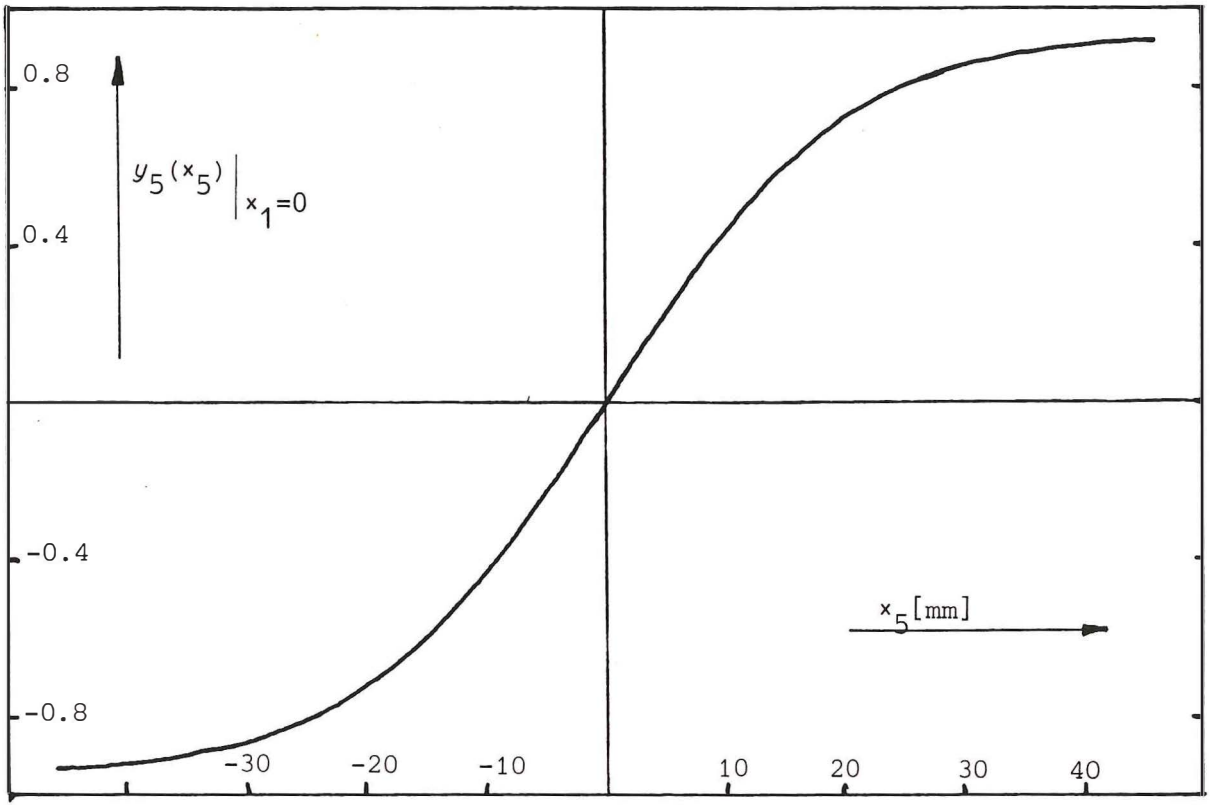

Figure A5.5. True axial measurement function, $y_5(x_5)$ for $x_1 = 0$. Saturation becomes significant at $\pm$20 mm approx.

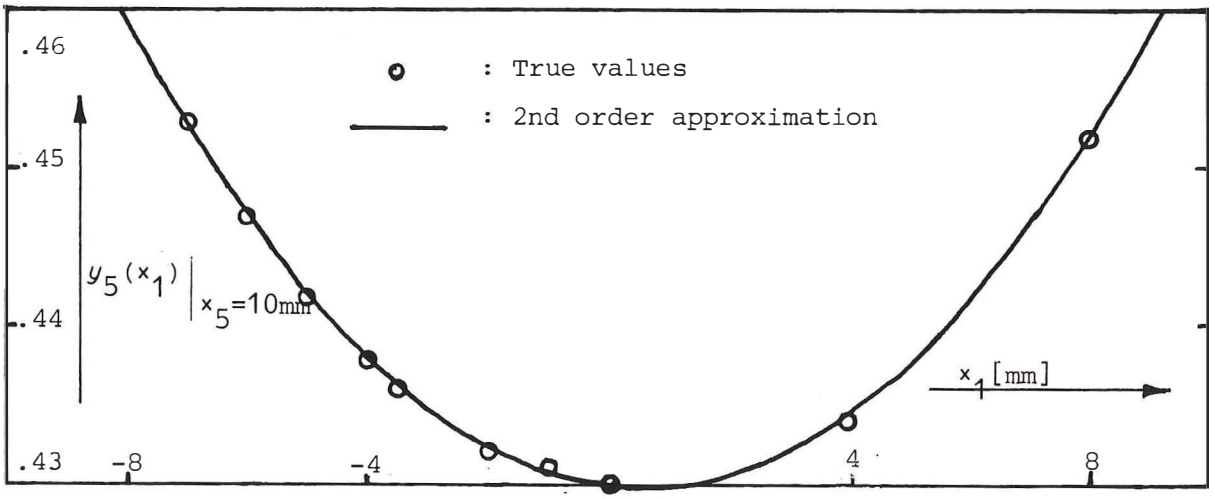

Figure A5.6. Obtained values of $y_5(x_1)$ at x_5 = 10 mm. The second order approximation fits the data very well.

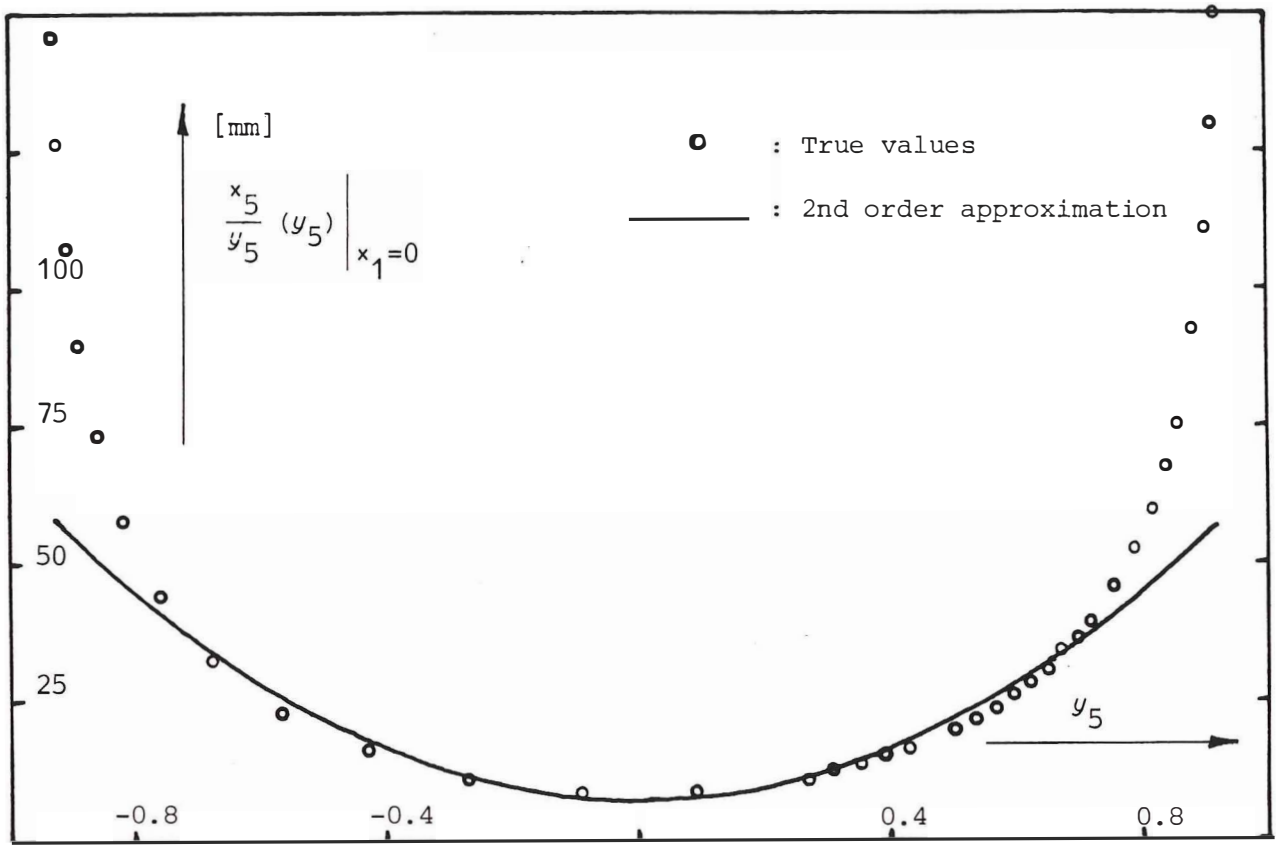

Figure A5.7. Actual values of x_5/y_5 as a function of y_5 compared to a second order approximation. As seen, assumption k_a = 25 mm made in Section A5.2 is reasonable.

Table A5.6. Measurements y_1 and y_2 for different radial displacements x_1 and x_2. A rotational deviation δ_1 = 0.1 rad is set between the two parts of the sensor. Values may be compared to Table A5.1 directly.

000		158		316		462	
-06		148		301		448	
-14		127		265		394	
-21		098		214		316	
							$Y_1 \cdot 10^3$

000		000		-01		010	
160		147		130		110	
316		295		258		214	
470		437		381		309	
							$Y_2 \cdot 10^3$

for axial amplification. The latter is shown in Fig. A5.7 together with the corresponding tabulated values.

In order to investigate the sensitivity of the measurements with respect to rotational displacements, an orientational deviation

$$\delta_1 = 0.1 \text{ rad}$$

was set, and new values for y_1, y_2 and y_5 were tabulated. The results are presented in Tables A5.5 and A5.6. As seen, no notable difference appears in the axial measurement, y_5. Table A5.6 however, differs slightly from the corresponding entries in Table A5.1. The resulting error, if this effect is not taken into account, is approximately 3% at the current orientational deviation. By the mechanical data given in Section A5.1, orientational differences up to 0.3 radians may appear. Assuming the error to be a second order function in δ_1, measurement errors of up to 27% may thus be expected.

A5.4. Appolonius' theorem

Applied directly to Fig. 9.1, we want to prove the following

Theorem: Considering Fig. 9.1,

$$b_1 b_2 = a_1^2 \quad \Rightarrow \quad h_1/h_2 = b_1/a_1$$

$$b_1' b_2' = a_2^2 \quad \Rightarrow \quad h_1'/h_2' = b_1'/a_2$$

Proof: Segments a_1, b_1 and h_1 are related by the Extended Pythagoran equation as

$$h_1^2 = a_1^2 + b_1^2 - 2a_1 b_1 \cos\theta \qquad \text{(A5.1)}$$

A similar relation including h_2^2 is

$$h_2^2 = a_1^2 + b_2^2 - 2a_1b_2\cos\varepsilon \qquad \text{(A5.2)}$$

Multiplication of (A5.1) by b_2, (A5.2) by b_1 and subsequent application of prerequisite

$$b_1b_2 = a_1^2 \qquad \text{(A5.3)}$$

yields

$$b_2h_1^2 = b_2a_1^2 + b_1a_1^2 - 2a_1^3\cos\varepsilon \qquad \text{(A5.4)}$$

$$b_1h_2^2 = b_1a_1^2 + b_2a_1^2 - 2a_1^3\cos\varepsilon \qquad \text{(A5.5)}$$

subtracting (A5.5) from (A5.4) results in

$$b_2h_1^2 - b_1h_2^2 = 0 \qquad \text{(A5.6)}$$

which implies

$$h_1^2/h_2^2 = b_1/b_2 \qquad \text{(A5.7)}$$

Since

$$b_1/b_2 = b_1^2/b_1b_2 \qquad \text{(A5.8)}$$

application of (A5.3) results in

$$h_1^2/h_2^2 = b_1^2/a_1^2 \qquad \text{(A5.9)}$$

which implies

$$h_1/h_2 = b_1/a_1$$

This proves the first statement. The second one is proved in a similar manner.

ISBN 82-7119-051-2